Nonlinear Optical Properties of Metal Free Thio Alkyl and Tert-butyl Phenoxy Phthalocyanine

A thesis submitted in fulfilment of the requirement for the degree of

MASTER OF SCIENCE

Of

RHODES UNIVERSITY

By

Otto Joseph

March, 2021

DEDICATION TO

To My Father and My Mother

Themba Dougal Joseph and Sindiswa Joseph

To my siblings Eddy, Africa and Pumeza

To Joseph and Mkhangala Family All

Let this work be a representation of the sacrifices made.

The society that separates its scholars from its warriors will have its thinking done by cowards and its fighting by fools.

- Thucydides

ACKNOWLEDGEMENTS

I would like to thank my main supervisor Professor Samson Khene for guiding me through this research project. I learnt too much and you encouraged me throughout the journey. I gained by being under your tutelage and I am grateful to have learnt under you. I would like to thank my co-supervisor Dr Britton for his support with my work and always being available to have a chat about research. I would like to thank the NIC and the CHPC for allowing me access to their instruments and to grow as a scientist.

I would like to thank my friend and mentor in research, Dr Marcel Louzada. I can never be grateful enough to have met someone who would have such a positive impact on me as a researcher. You taught me so much and you dragged me out for coffee too.

I would like to thank Dr Vincent Smith and Professor Rosa Klein for your contributions to my life, and encouraging me to be better. I would like to thank Thabo, Zelda and Dr Tayo for their input in my work and in my life. Sharing this laboratory with you was truly a blessing. I would like to thank all the members of F3 and F5 for all the advice and constructive conversation and input we shared. It was a pleasure to learn from you all.

And to those friends mine Kef, Lukay, Tendai M, Nontu and Zo for all your support and Samukelo Khumalo, who reminds me everyday that life is short. I would like to thank my good friend Mel, who supported me through it all, I will forever be grateful to have a friend like you.

I would like to thank the National Research Foundation (Thuthuka), CSIR(IBS) and Rhodes University Henderson Scholarship for funding and support with my work. I could not have done this work without your continuous support. I would like to thank John Gillam for assisting me with funding and, more importantly, guiding me on my journey as a postgraduate.

Ngicela ithuba lukobonga umdeni wakaJoseph ngokungikhuthaza, nokunginika usizo ngizengiphumelele.

ABSTRACT

This work reports on the nonlinear optical properties of tetra - and octa substituted phthalocyanines (Pcs) utilising pentane thiol and 4-tertbutyl phenol as substituents. Their nonlinear absorption coefficient (β) and absorption cross sections were determined using the Z-scan technique with a 10 ns pulse laser at 532 nm. The molecular second order hyperpolarizability Im[γ] was observed and the following Im[γ] trend was obtained for α-$H_2Pc(SC_5H_{11})_4$ isomers, 5.93×10^{-31} ($\mathbf{C_s}$) 2.24×10^{-32}($\mathbf{D_{2h}}$) > 1.21×10^{-32}($\mathbf{C_{4h}}$) > 1.05×10^{-32} ($\mathbf{C_{2v}}$) esu, respectively, in chloroform. Symmetry was seen to have an effect on the observed reverse saturable absorption (RSA) response. Based on the five level model rate equation nonlinear fit of the RSA response curves and Real Time Time Dependant Density Functional Theory (RT-TDDFT) results, the singlet excited state population dynamics was found to play a significant role in producing the observed Im[γ] trend.

TABLE OF CONTENTS

Contents

LIST OF ABBREVIATIONS

Abs	**Absorbance**
CD	**Circular Dichroism**
CHPC	**Centre for High Performance Computing**
DCM	**Dichloromethane**
Em	**Emission**
ESA	**Excited State Absorption**
ESR	**Electron Spin Resonance**
Exc	**Excitation**
HOMO	**Highest Occupied Molecular Orbital**
HPLC	**High Performance Liquid Chromatography**
IC	**Internal Conversion**
ISC	**Intersystem Crossing**
IR	**Infrared Spectroscopy**
LUMO	**Lowest Unoccupied Molecular Orbital**
MCD	**Magnetic Circular Dichroism**
MO	**Molecular Orbital**
MS	**Mass Spectrometry**
V_m	**Molecular volume**
Nd:YAG	**Neodymium-doped yttrium aluminium garnet**
NLO	**Nonlinear Optics**
NMR	**Nuclear Magnetic Resonance**
Pc	**Phthalocyanine**

RSA	**Reverse Saturable Absorption**
RT-TDDFT	**Real Time Time Dependent Density Functional Theory**
SA	**Saturable Absorption**
SHG	**Second Harmonic Generation**
TCSPC	**Time Coupled Single Photon Counting**
TDDFT	**Time Dependent Density Functional Theory**
TPA	**Two-Photon Absorption**
TRES	**Time-Resolved Emission Spectra**
UV/Vis	**Ultraviolet-visible Spectrometry**

LIST OF SYMBOLS

θ	**Anisotropy rotational correlation time**
N_A	**Avagadro's number**
k	**Boltzmann constant**
c	**Speed of light**
	Concentration
e	**Charge of electron**
L_{eff}	**Effective path length of the sample**
E	**Electric field vector**
	Energy
χ	**Electrical Susceptibility**
τ	**Fluorescence lifetime**
z_0	**Focal position**
ν	**Frequency of light**
I	**Intensity**
f	**Lorenz local field factor**
m	**Mass**
Q_0	**Maximum value for** $q_0(z_s)$
V_m	**Molecular volume**
η^2	**Nonlinear Refractive Index**
β	**Nonlinearity of transmittance**
β	**Nonlinear absorption coefficient**
	Peripheral position

α	**Non-peripheral position**
	Linear absorption coefficient
μ_0	**Permeability of free space**
ε_0	**Permittivity of free space**
h	**Planck's constant**
P	**Polarisation**
P_0	**Power of laser pulse**
z_R	**Rayleigh range**
L	**Sample thickness**
$Im[\gamma]$	**2^{nd} order nonlinear polarisability**
T	**Temperature**
$T_n(z_s)$	**Normalised Transmittance**
η	**Viscosity**
λ	**Wavelength**
z	**Z-Scan position**
σ_1	**Ground state absorption cross section**
σ_2	**Singlet state absorption cross section**
σ_3	**Triplet state absorption cross section**
σ_{TPA}	**Two-photon absorption cross section**
S_0	**Ground state**
S_1	**First excited state**
S_n	**n^{th} singlet state**
T_1	**First triplet state**
T_n	**n^{th} triplet state**

LIST OF FIGURES

LIST OF SCHEMES

LIST OF TABLES

Chapter 1: Introduction

1.1 Non-Linear Optics

1.1.1 Optical Limiting

Optics is concerned with the genesis and radiation of light and the changes that it undergoes and produces. Amongst the two major branches of optics, geometrical and physical, geometrical optics includes the principles that govern the image-forming properties of mirrors and lenses , whereas physical optics entails the nature and properties of light[1]. From this point the study of the behaviour of this light can be placed into the fields of classical optics (typically conforming to Maxwell's equations)[2] and non-classical optics, or more specifically in these studies, Non Linear Optics (NLO).

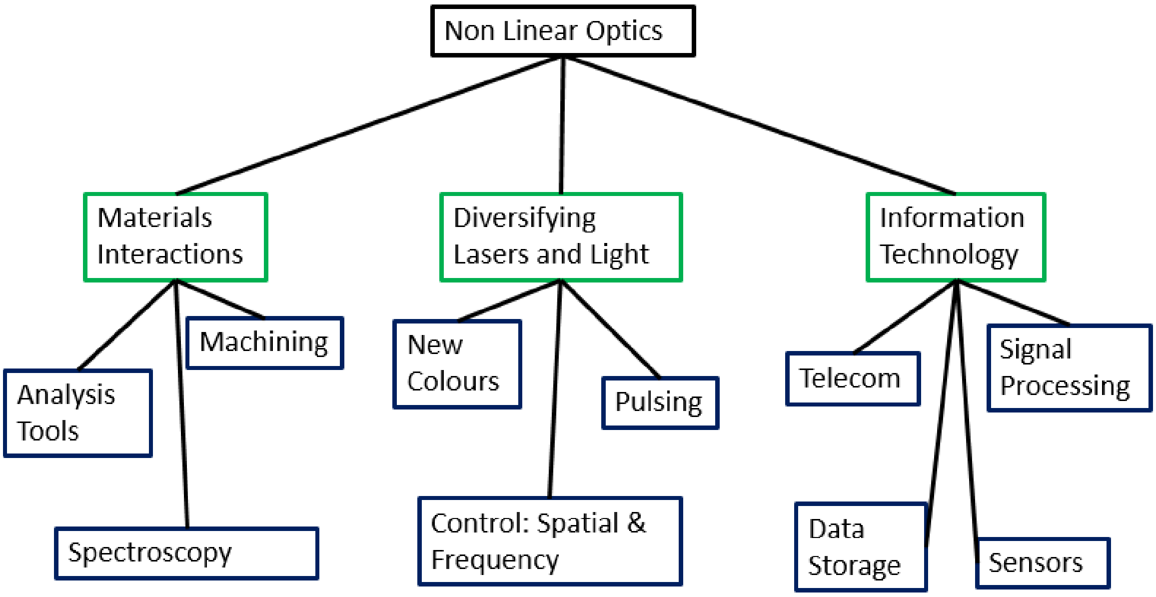

Figure 1.1: A diagram displaying various applications of Non Linear Optics[3].

As seen in **Figure 1.1**, NLO has a wide range of uses in industry and research. NLO limiting materials are of interest due to the need to protect sensitive optical devices, especially human eyes, from high intensity light sources such as lasers. These materials, simply put, have non-linear optical responses to light. When exposed to very intense light, NLO materials limit the output energy of the emerging beam[4]. This effect can be seen in **Figure 1.2** below, displaying the development of nonlinear transmission as intensity rises. NLO materials also provide a non-mechanical method of controlling light intensity. These responses are typically as a result of the atomic or molecular structure of the material[5]. Most materials that show optical properties have non-linear optical properties, but these are seldom observed and typically require the application of an electromagnetic field of such strength that it is in the same order of strength as the interatomic field strength[6].

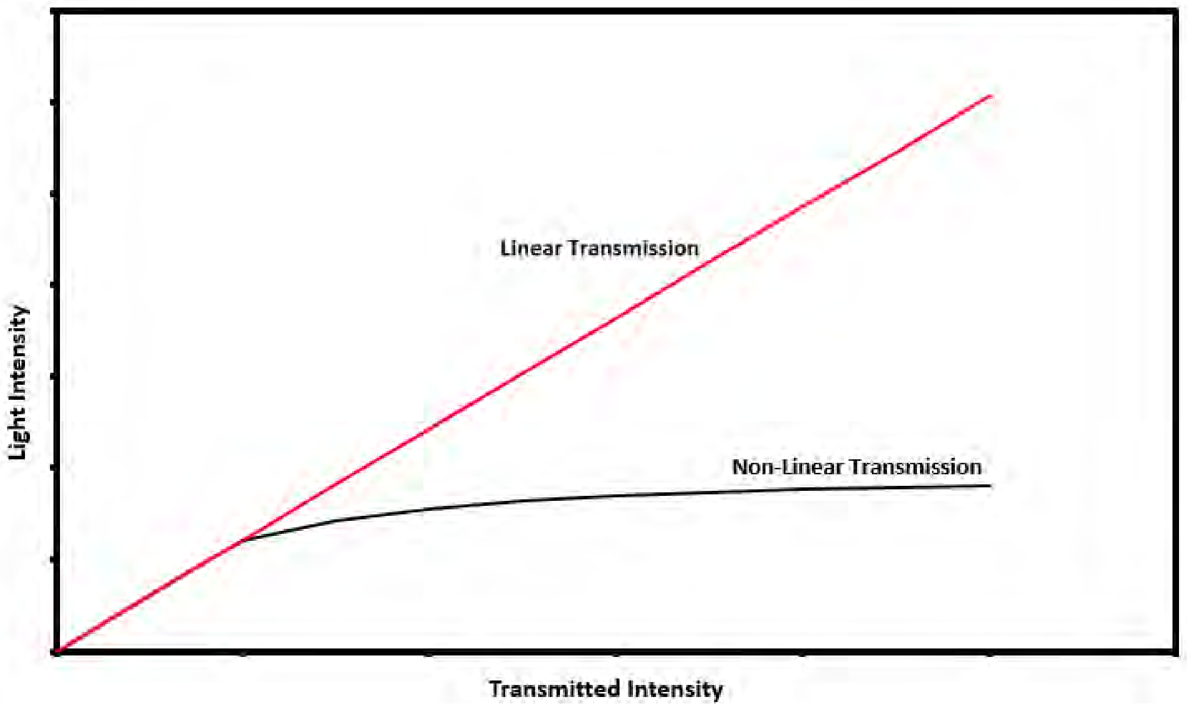

Figure 1.2: Graph of light transmitted in a Non-Linear Optical Limiter.

Lasers and fields where lasers are of importance are at the heart of NLO applications. The first ruby laser was developed by Theodore Maiman in 1960[7], and the next year a team led by Peter Franken at the University of Michigan observed optical second harmonic generation (SHG), a NLO response[8]. This arised from the fact that laser light can have an optical power much larger in magnitude than any other light sources[9]. This discovery led to an expansion of a mostly unknown field, and the discovery of the optical Kerr effect, optical parametric amplification, third harmonic generation and optical rectification[9].

1.1.2 Causes of Optical Nonlinearities

There are many processes that may result in NLO effects, some of which may have already been mentioned; the Kerr effect, difference frequency generation, sum frequency generation, second harmonic generation, third harmonic generation, optical parametric fluorescence, optical parametric amplication and optical parametric oscillation being some of them[10]. As light moves through a material (medium), the electric field of the light results in the development of an electric polarisation in the medium. In low intensity light, the electric polarisation in a medium is proportional to the electric field strength. In high intensity light (typically produced with lasers), the electric polarisation in a medium is non proportional to the electric field strength and can cause the development of nonlinear optical effects. This can be depicted by a Taylor series expansion of the dielectric polarisation *P(t)* response to the electric field *E(t)* in **Equations 1-3**:

$$P(t) = \mu_0 + \varepsilon_0(\chi^{(1)}E(t) + \chi^2E^2(t) + \chi^3E^3(t) + \ldots) \quad \mathbf{(1)}$$

$$P(t) = P^{(1)} + P^{(2)} + P^{(3)} \quad \mathbf{(2)}$$

$$P(t) = P^{(1)} + P^{(NL)} \quad \mathbf{(3)}$$

Where the $\chi^{(n)}$ symbol represents the complex susceptibilities each containing a Real and Imaginary component, μ_0 is the permeability of free space, and ε_0 is the permittivity of free space. While the nonlinear susceptibilities are reliant on the applied electric field *E(t)*, as a result of the assumption that the medium immediately responds to the field and is therefore, due to the Kramers–Kronig relations, lossless and dispersionless, the nonlinear susceptibilities can thus be taken as constants[10].

The first order susceptibility, $\chi^{(1)}$, dictates most of the response to *E(t).* The second order susceptibility, $\chi^{(2)}$, causes the aforementioned NLO processes such as second harmonic generation, Hyper Rayliegh scattering, sum frequency generation and difference frequency generation, optical parametric fluorescence, optical parametric amplication and optical parametric oscillation[5, 11, 12].

The third order susceptibility, $\chi^{(3)}$, causes some absorption processes and is related to real component of refraction. Here the real component of refraction represents the refractive index while the imaginary component represents the absorption of light of the material. Third harmonic generation, self-phase modulation, cross-phase modulation, four-wave mixing and Kerr lensing are effects that can be affected by this susceptibility.

In **Equation 1**, the χ value decreases, by order of 10^{-12} as the order increases. This results in the higher order susceptibilities having minimal effect on the observed resultant light behaviour. The approximate values of $\chi^{(1)}, \chi^{(2)}$ and $\chi^{(3)}$ are defined in **Equations 4-6** as[13]:

$$\chi^{(1)} \simeq 1 \qquad \textbf{(4)}$$

$$\chi^{(2)} \simeq \frac{(4\pi\varepsilon_0)^3\hbar^4}{m^2e^5}m/V \qquad \textbf{(5)}$$

$$\chi^{(3)} \simeq \frac{(4\pi\varepsilon_0)^6\hbar^8}{m^2e^5}m^2/V^2 \qquad \textbf{(6)}$$

Where m is the mass and e is the charge of an electron. While $\chi^{(3)}$ can be seen in both centrosymmetric and noncentrosymmetric media, $\chi^{(2)}$ can only occur in noncentrosymmetric crystals. This is because amorphous solids (such as glass), liquids and gases, display inversion symmetry, and thus $\chi^{(2)}$ disappears. The nonlinearities observed can be placed into two groups, Nonlinear Absorption and Nonlinear Refraction.

For a material in an electric field caused by plane polarized light, the polarization of the molecule can be defined as an induced dipole in **Equation 7**:

$$\vec{u} = \alpha\vec{E} + \beta\vec{E}^2 + \gamma\vec{E}^3 + \cdots \qquad \textbf{(7)}$$

Where α is the linear polarizability, β is the first hyperpolarisability of the molecule and γ is the second hyperpolarisability of the molecule. β is the sum of its dipolar ($\beta_{j=1}$) and octupolar ($\beta_{j=3}$) components, while γ is the sum of its real (Re[γ]) and imaginary (Im[γ]) components.

1.1.3 Nonlinear Absorption

There are a range of nonlinear optical absorptions that can take place once a nonlinear optical limiter experiences irradiation by a light source. Amongst the absorptions that can be observed, multiphoton absorption and excited state absorption are two of the processes that can take place[10]. There are different grouping models that can be used to analyse these absorptions, namely parametric and nonparametric models[5]. Parametric models entail a process where the initial and the final quantum-mechanical states of the system are indistinguishable from each other.

In a parametric process there are instances whereby the population may be removed from the ground state, such as the small instances in time where it resides in a virtual state[10]. This process is defined by a real susceptibility and here the energy of the photon is conserved. Nonparametric processes are defined by a complex susceptibility and the energy of the photon does not need to be conserved.

1.1.3.1 Two-Photon Absorption

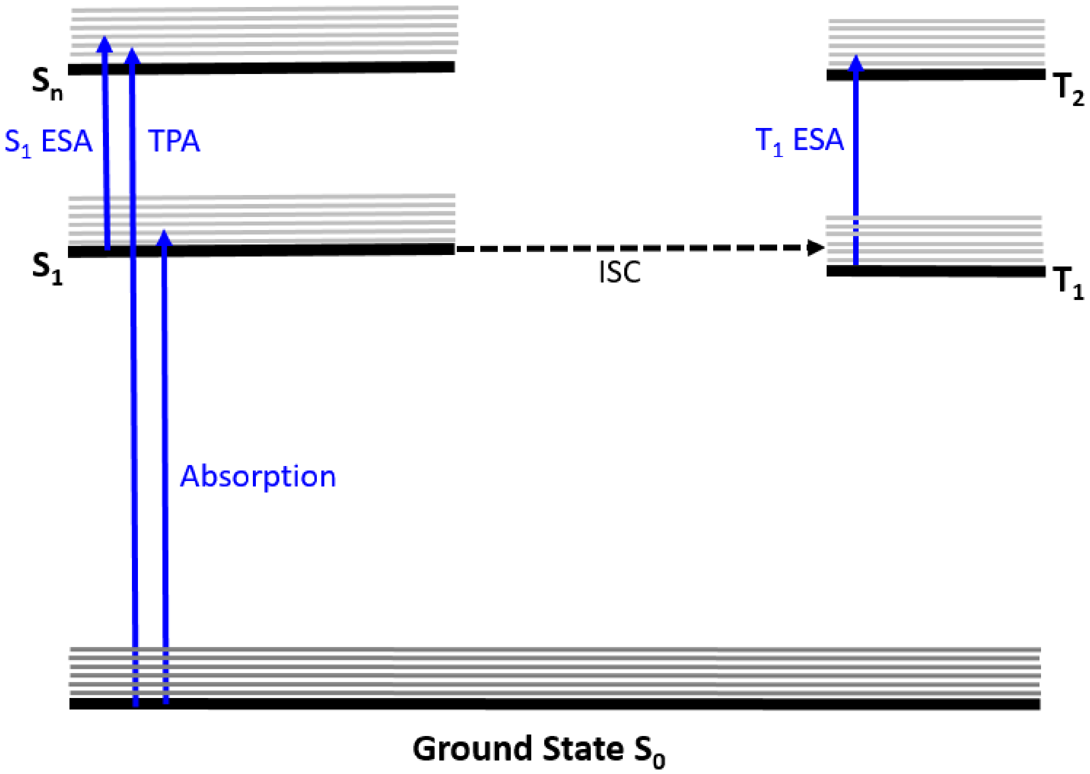

Figure 1.3: Perrin-Jablonski diagram mapping out photophysical absorptions for a phthalocyanine (Pc)[5].

The electronic states shown in **Figure 1.3** above include the ground state(S_0), the first singlet excited state (S_1), the nth singlet excited state (S_n), the first triplet state (T_1) and the nth triplet excited state (T_n). The grey lines show some vibronic states associated with each of those energy levels. The main transitions of absorption are shown in blue arrows and these include $S_0 \rightarrow S_1$ Ground State Absorption, $S_1 \rightarrow S_n$ Excited State Absorption (ESA), $S_0 \rightarrow S_n$ Two-Photon Absorption (TPA) and $T_1 \rightarrow T_n$ ESA. The Intersystem System Crossing (ISC) transition is shown in a black dashed arrow.

Compounds with NLO properties, such as nonlinear absorption, can be studied using experimental and theoretical methods. Due to the nature of these different types of absorptions (that are typically nonparametric)[10], computationally expensive calculations can be made to give insight into the population of various states, the energy associated with these states and the changes in electron density within the molecule.

There are multiple absorption processes that can take place upon irradiating a chromophore. The simplest process is single photon absorption in which a chromophore is excited from a ground state to an excited state. Within a specific concentration range, a linear relationship between absorbance and concentration of a chromophore at a specific wavelength can be observed and defined by a modified Beer-Lambert Law described by **Equation 8**[14]**:**

$$\frac{\partial I}{\partial L} = -L c_{molec} I \sigma \qquad \textbf{(8)}$$

Where L is the sample thickness, c_{molec} is the concentration in molecules/L, I is the intensity and σ is the molecular absorption cross section. The key principle of the Beer-Lambert law is that every photon of light must have an equal chance of absorption. Theoretically, each photon should have the same absorption coefficient, should pass through the same sample thickness and experience the same absorption concentration[15].

A more complicated process that can be observed is when a chromophore absorbs two-photons at the same instant, otherwise referred to as two-photon absorption. This is the simplest type of multiphoton absorption and it occurs when there is no allowed one photon absorption. This process is only observed at high intensities and contributes to the functionality of compounds used in photodynamic cancer therapy, optical limiting and high resolution bioimaging. Theoretical modelling allows for the use of two-photon absorption spectroscopy in conjunction with one photon absorption spectroscopy to give information about molecular electronic structure[16]. The two-photon absorption cross section is computed by considering the lifetime of an intermediary 'virtual state', and the cross sections of both this virtual state and the initial state. The absorption cross section σ, has a linear relationship with the intensity *I* of the laser. This relationship defined is by **Equation 9**:

$$\sigma = \sigma^{(2)} I \tag{9}$$

where $\sigma^{(2)}$ denotes the strength of the two-photon absorption process and I is the intensity of the light[10].

1.1.3.2 Excited State Absorption

While the ground state absorption is a commonly known feature in many chromophores, excited state absorption adds another dimension to nonlinear absorption. Saturable Absorption (SA) and Reverse Saturable Absorption (RSA) are excited state absorptions that can be observed. SA occurs when the excited state cross section is smaller than the ground state at a particular wavelength. RSA occurs when the excited state cross section is larger than the ground state cross section at a particular wavelength[17].

1.1.3.3 Parametric Nonlinear Absorption Model

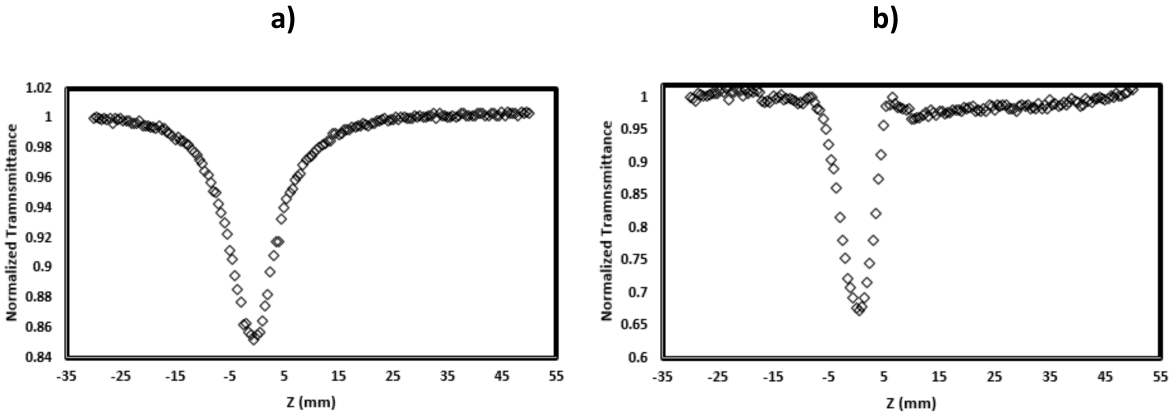

Figure 1.4: The raw experimental results of (a) open aperture Z-scan measurements (b) subtracted closed aperture Z-scan measurements of a sulphur substituted phthalocyanine.

The parametric model of solving for nonlinear absorptions entails using **Equation 1** to understand and interpret **Figure 1.4** above. One of the methods used is a model developed by Tsigaridas and co-workers[18]. The normalized transmittance is given by the **Equation 10**[18]:

$$T_n(z_s) = \frac{1}{Aq_0(z_s)} \int_{-\infty}^{\infty} \ln[1 + q_0(z_s) f(\tau)] \, d\tau \qquad \textbf{(10)}$$

Where the transmittance (T_n) is described as a function with respect to the position along the beam length (*z*). The parameter $q_0(z_s)$ is a position dependant absorption parameter that denotes the strength of the nonlinearity. $f(\tau)$ is a function describing the temporal profile of the laser pulse. (*A*) is the normalisation constant that is described by **Equation 11:**

$$A = \int_{-\infty}^{\infty} f(\tau) d\tau \qquad \textbf{(11)}$$

In **Equation 12** below, $q_0(z_s)$ can be related to the nonlinear absorption coeffient β:

$$q_0(z_s) = \frac{2\beta P_0 L_{eff}}{\pi\omega^2(z_s)} \qquad \textbf{(12)}$$

Where P_0 the power of the laser pulse, $\omega(z_s)$ is the beam width with respect to position z and L_{eff} is the effective path length of the sample defined by **Equation 13**:

$$L_{eff} = \frac{1 - e^{-aL}}{a} \qquad \textbf{(13)}$$

Where L is the sample length and α the linear absorption coefficient. $\omega(z)$ is defined in **Equation 14** as:

$$\omega(z) = \omega_0 \sqrt{1 + \frac{z_s - z_0}{z_R}} \qquad \textbf{(14)}$$

Where ω_0 is the beam width at the focus and z_0 is the location of the beam focus. The parameter z_R is the Rayleigh length is can be related to the beam wavelength λ by **Equation 15**:

$$z_R = \frac{\pi {\omega_0}^2}{\lambda} \qquad \textbf{(15)}$$

Initially, the parameter $q_0(z_s)$ is derived by fitting **Equation 10** to experimental data. **Equations 12-15** are then used to calculate the nonlinear absorption coefficient β. Determining the parameter $q_0(z_s)$ of open Z-scan experiments is complicated and time-consuming, especially when other methods of acquiring applicable values of $q_0(z_s)$ directly from the normalized transmittance $T_n(z_s)$ exist. This is done by recurringly using **Equation 10** for several values of $q_0(z_s)$, in order to produce a series of $q_0(z_s)$: $T_n(z_s)$ values. Upon Fitting this data with the relevant analytical functions, the dependence of the nonlinear absorption parameter $q_0(z_s)$ on the normalized transmittance $T_n(z_s)$ is found and it is given by the **Equation 16:**

$$q_0(z) = \begin{cases} a_0 + a_1 T_n(z) + a_2 {T_n}^2(z) + a_3 {T_n}^3(z), & if\ T_n(z) \leq 0.75 \\ c_0 + c_1[T_n(z)]^{c_2}, & if\ T_n(z) \geq 0.75 \end{cases} \quad \textbf{(16)}$$

Where $a_0, a_1, a_2, a_3, c_0, c_1, c_2$are coefficients for both cases of Gaussian and hyperbolic secant pulses that have been determined by Tsigaridas. Using this simpler approach, the substitution of **Equation 14** into **Equation 12** results in **Equation 17:**

$$q_0(z_s) = \frac{Q_0}{1+(\frac{z_s - z_0}{z_R})^2} \quad \textbf{(17)}$$

Where Q_0 is

$$Q_0 = \frac{2\beta P_0 L_{eff}}{\pi {\omega_0}^2} = \frac{2\beta P_0 L_{eff}}{\lambda z_R} \quad \textbf{(18)}$$

Figure 1.5 below shows that the $q_0(z_s)$ curve takes its maximum value Q_0 at the beam waist ($z_s = z_0$) while at $z_s = z_0 \pm z_R$, the value of $q_0(z_s)$ is equivalent to $Q_0/2$. The result of this is that the full width at half maximum (FWHM) of the $q_0(z_s)$ curve is equal to $2z_R$. As a result, the peak value and the FWHM of the $q_0(z_s)$ curve display the values of Q_0 and z_R.

By using **Equation 18**, the nonlinear absorption coefficient β is calculated by **Equation 19:**

$$\beta = \frac{Q_0 \lambda {z_R}^2}{P_0 L_{eff}} \quad \textbf{(19)}$$

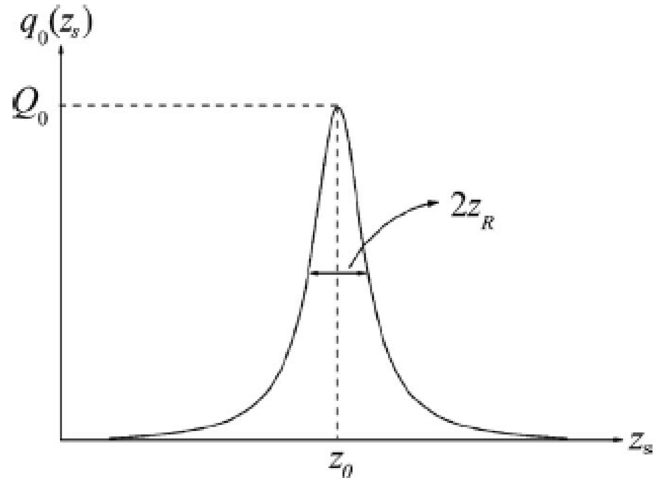

Figure 1.5: Direct determination of the parameters Q_0, z_0, z_R, from a $q_0(z_s)$ curve[18].

The parameter β can then inserted into **Equation 20** to calculate $Im[x^{(3)}]$:

$$Im[x^{(3)}] = \frac{n\varepsilon_0 c^2 \lambda \beta}{2\pi} \qquad \textbf{(20)}$$

Where c is the speed of light in a vacuum. **Equation 20** shares a relation with **Equation 1**. $Im[x^{(3)}]$ defines the nonlinear absorption of the sample. The value of this parameter is determined by finding the imaginary component of the third order polarisability, otherwise referred to as the second-order hyperpolarisability $Im[\gamma]$ in **Equation 21**:

$$Im[\gamma] = \frac{Im[x^{(3)}]}{f^4 N N_A} \qquad \textbf{(21)}$$

Where f is the Lorentz local field factor, N the concentration, and N_A is Avogadro's number. $Im[\gamma]$ determines the response of each molecule resulting in $Im[x^{(3)}]$. The parametric nonlinear absorption model parameters $Im[x^{(3)}]$ and $Im[\gamma]$ are responsible for all nonlinear absorption. **Equation 22** below describes the relationship between International System of Units (SI) as $(m^2.V^2)$ and electrostatic units as (esu), two units that are used to report $Im[x^{(3)}]$ and $Im[\gamma]$. Electrostatic units will be used in this work:

$$Im[x^{(3)}](m^2.V^2) = \frac{4\pi}{9} Im[x^{(3)}](esu) \qquad \textbf{(22)}$$

1.1.3.4 Nonparametric Nonlinear Absorption Model

The parametric nonlinear absorption model, while useful, can not account for all nonlinear aborptions observed. This model in particular can fail to model mechanisms and properties of slow response NLO absorptions. One of the cases that can occur is when a molecule has equal amounts of RSA and SA at a specific Intensity. In this instance it will appear as if the material does not have NLO properties, thus adding difficulty in the ability to analyse and investigate the material’s properties and how tuning external factors like laser intensity will affect those important properties. A model capable of being able to compute the multiple photophysical processes that occur simultaneously would be more computationally complex, but can provide a more accurate model to show nonparametric processes. The Perrin-Jablonski diagram seen in **Figure 1.3** displays some of the absorptions that can take place within a material. Only transitions that were in the energy range of interest were included. The model used sees five energy level, and the **Equations 23-28**[5] are used to describe their population dynamics:

$$\frac{\partial}{\partial t}N_{S_0} = -\sigma_1\frac{IN_{S_0}}{h\nu} - \sigma_{TPA}\frac{IN_{S_0}}{(h\nu)^2} + \frac{IN_{S_1}}{\tau_{S_1,S_o}} + \frac{IN_{T_1}}{\tau_{T_1,S_o}} \tag{23}$$

$$\frac{\partial}{\partial t}N_{S_1} = \sigma_1\frac{IN_{S_0}}{h\nu} - \sigma_n\frac{IN_{S_1}}{h\nu} - \frac{IN_{S_1}}{\tau_{S_1,S_o}} - \frac{IN_{S_1}}{\tau_{S_1,T_1}} \tag{24}$$

$$\frac{\partial}{\partial t}N_{S_n} = \sigma_{TPA}\frac{I^2N_{S_0}}{(h\nu)^2} + \sigma_n\frac{IN_{S_1}}{h\nu} - \frac{IN_{S_n}}{\tau_{S_n,S_1}} \tag{25}$$

$$\frac{\partial}{\partial t}N_{T_1} = -\sigma_3\frac{IN_{T_1}}{h\nu} + \frac{N_{S_1}}{\tau_{S_1,T_1}} + \frac{N_{T_n}}{\tau_{T_n,T_1}} + \frac{N_{T_1}}{\tau_{T_1,S_o}} \tag{26}$$

$$\frac{\partial}{\partial t}N_{T_n} = \sigma_3\frac{IN_{T_1}}{h\nu} - \frac{N_{T_n}}{\tau_{T_n,T_1}} \tag{27}$$

$$N_{total} = N_{S_0} + N_{S_1} + N_{S_2} + N_{T_1} + N_{T_n} \tag{28}$$

In **Equations 23-28**, $N_{S_0}, N_{S_1}, N_{S_2}, N_{T_1}$ and N_{T_n} are the populations of the S_0, S_1, S_n, T_1 and T_n states, respectively. N_{total} is the total population of all the states. σ_1, σ_2 and σ_3 are the absorption cross sections for the ground state, singlet state, and triplet state single photon absorptions, respectively. σ_{TPA} is the two-photon absorption cross section, *h* is Planck's constant, and *v* the frequency of the light. $\tau_{S_1,S_0}, \tau_{T_1,S_0}, \tau_{S_1,T_1}, \tau_{S_n,S_1}, \tau_{S_1,T_1}$ and $\tau_{T_n,T_1}$are parameters that are inverses of the rates of the S_1 → S_0,T_1→ S_0, S_1 → T_1, S_n → S_1 and T_n →T_1 transitions, respectively. By adjusting **Equation 8** for this nonparametric model, **Equation 29** can be written as:

$$\frac{\partial I}{\partial z'} = -I(\sigma_1 N_{S_0} + \sigma_2 N_{S_1} + \sigma_3 N_{T_1} + \sigma_{TPA} N_{S_0} I) \tag{29}$$

To solve **Equations 23-28**, knowing the state lifetime parameters $\tau_{T_1,S_0}, \tau_{S_1,T_1}, \tau_{S_n,S_1}$ and τ_{T_n,T_1} is required. **Equation 29** is a simpler equation to solve but has three unknown variables. To remedy this, three measurements are to be taken at different points, whilst only varying one parameter, such as concentration, z_R, laser pulse duration or laser pulse intensity. Pulse intensity is usually chosen because it is relatively easy to adjust, thus enforcing the principle of keeping all the other variables constant.

A material’s ability to undergo NLO processes is dependent on parameters affecting the excited state population and the difference in magnitude between the ground state absorption and the excited state absorption[5]. Should RSA be the most significant contributor to nonlinear absorption for a material (where excited state cross section is larger than the ground state cross section at a particular wavelength), then its ability as a NLO material will effected by **Equation 30**[19]:

$$\frac{\sigma_{eff}}{\sigma_1} \approx \frac{\sigma_2 \frac{N_{S_1}}{N_{totalE1}} + \sigma_3 \frac{N_{T_1}}{N_{totalE}}}{\sigma_1} \tag{30}$$

Where the ratio between effective excited state cross section (σ_{eff}) and the ground state absorption cross sections (σ_1) is described. N_{totalE} is the total excited state population (N_{T_1}+N_{S_1}).

Substances and compounds that elicit these responses, from solids to gases, are of value. Due to the uses of NLO in medicine, communication and computing. Organic materials with potential modern device application must meet a range of requirements, such as a high decomposition threshold to laser irradiation and photolysis, have large delocalized π-systems and the material must not reabsorb the harmonic frequency it produces. A class of molecules that fit these requirements are porphyrins, cumulenes, platinum acetylides, phthalocyanines and metallophthalocyanines[20, 21]. This work focuses on the use of phthalocyanines as possible NLO materials.

1.2 Phthalocyanines

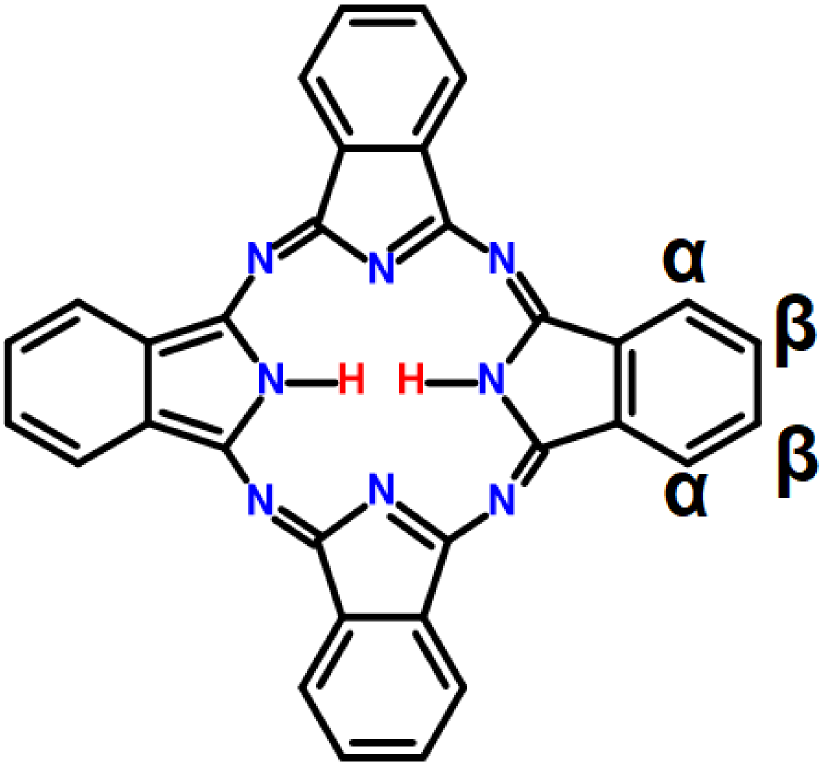

Figure 1.6: General structure of phthalocyanine showing alpha and beta positions available for substitution.

Phthalocyanines (Pcs) are a class of organic aromatic 18-π electron system porphyrin derivatives that contain an open cavity where 70 different metals and non-metal atoms can be inserted. The compounds are thermally and chemically stable complexes, and can be used in pigments, dyes, field effect transistors, light-emitting diodes, photovoltaic cells, or gas sensors. Pcs are one of the most widely investigated molecules for optical limiting (OL) applications[22].

Accidently discovered in 1907 by Braun and Tcherniac at the Grangemouth plant of Scottish Dyes Ltd, as a result of a synthesis for ortho-cyanobenzamide involving phthalimide and acetic acid, the class of compounds did not receive keen interest until 1928[23, 24]. The blue-green product synthesized became the subject of interest by Linstead in 1928, where the name phthalocyanine was derived from the Greek words "naphtha" and "cyanine", meaning rock oil and blue, respectively. There is some dispute about who named the substance in 1928, some sources claiming this was the work of Linstead[25], while others standing by the believe that it was Dandridge[26]. What is confirmed is that Linstead conducted 3 tests in the form of oxidative degradation, elemental analysis and mass determination to study the Pc structure[25]. Robertson was able to show the planar geometry by use of X-Ray crystallography, providing important insight into the features of Pcs and their structural properties[27].

1.2.1 Synthesis

Scheme 1.1: Phthalocyanine Synthesis

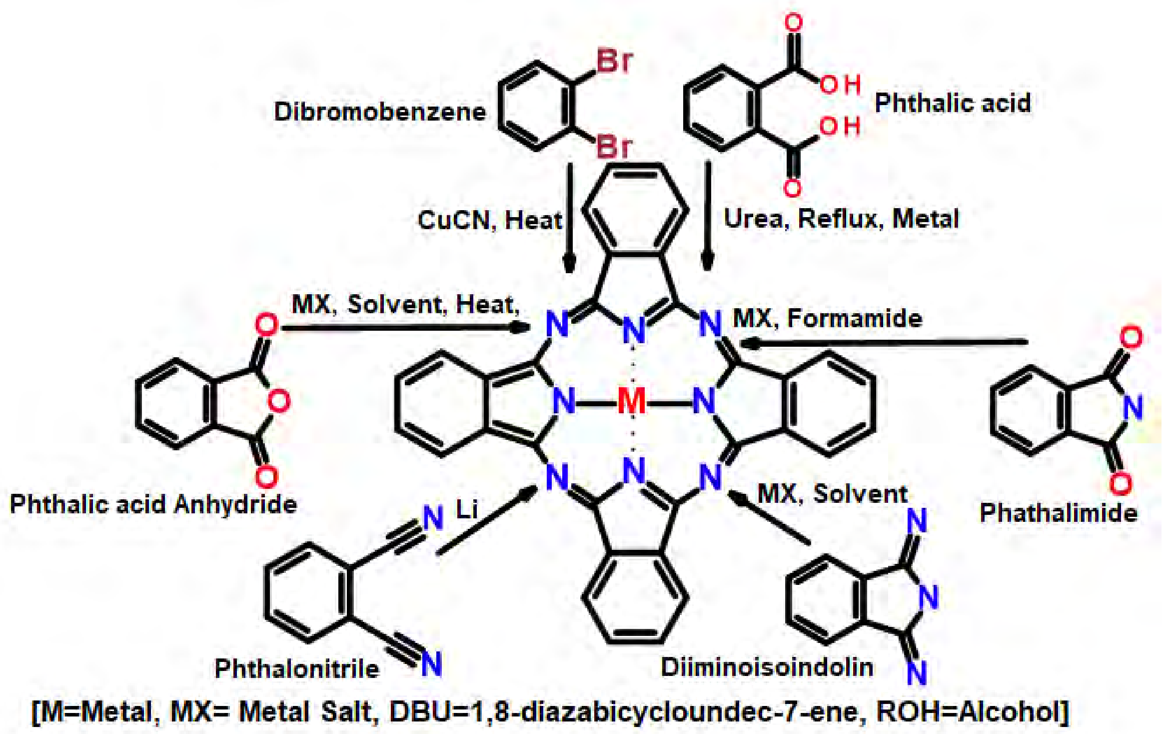

[M=Metal, MX= Metal Salt, DBU=1,8-diazabicycloundec-7-ene, ROH=Alcohol]

One of the reasons Pcs have attracted so much attention is the versatility of their synthetic methods (see **Scheme 1.1**), which allows for structural variation in order to achieve the desired properties for various applications[4, 20]. Unsubstituted metal phthalocyanines are largely insoluble in common solvents, thus making spectroscopic analysis difficult. The addition of functional groups on the peripheral (β) and non-peripheral positions (α) greatly effects solubility, stability and spectroscopic properties of the compound[28]. Octa-substituted Pcs are formed through the condensation of a disubstituted precursor, while tetra-substituted Pcs are formed through the condensation of a mono-substituted phthalonitrile precursor (see **Table 1.1**).

Table 1.1: General Structures of Substituted Phthalocyanines

	Alpha	Beta
Octa		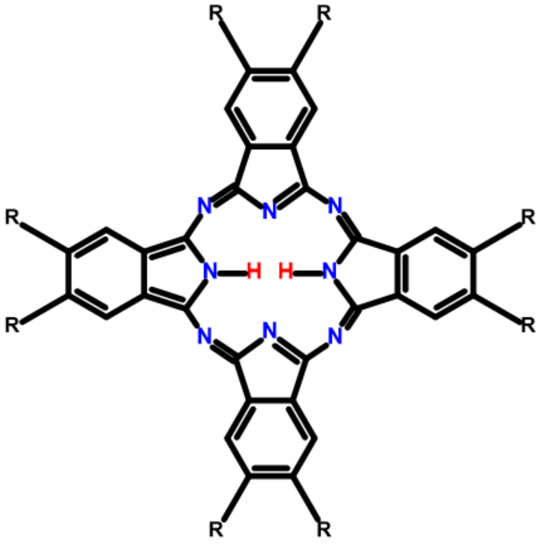
Tetra	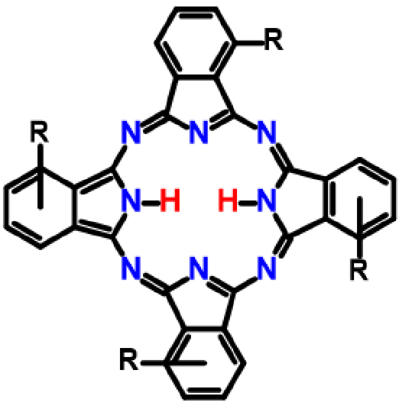	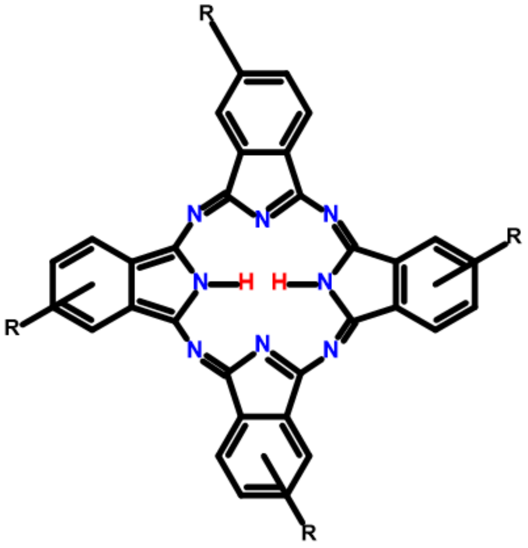

The reaction of mono-substituted phthalonitrile (in the presence of a base catalyst) yields 4 positional isomers that can be separated out by the use of chromatographic methods such as High Performance Liquid Chromatography (HPLC) and Column Chromatography (CC). However, it has been shown in literature that substitution of bulky substituents allows separation of positional isomers by ordinary column chromatography[5, 29, 30]. The separation results in the isolation of 4 isomers of symmetry C_{4h}, C_s, D_{2h} and C_{2v} (see **Table 1.2**). Some have reported a statistical mixture of 12.5% C_{4h}, 50% C_s, 12.5% D_{2h} and 25% C_{2v} by use of HPLC[31, 32]. Isomers displaying lower symmetry typically have higher dipole moments as a result of a higher unsymmetrical arrangement of the substituents in the periphery of the ring[31, 32].

Table 1.2: General Structures of Tetra-Substituted Phthalocyanines

Symmetry	Alpha	Beta
C_{4h}	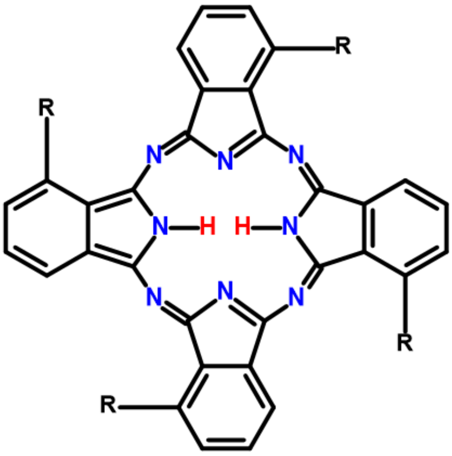	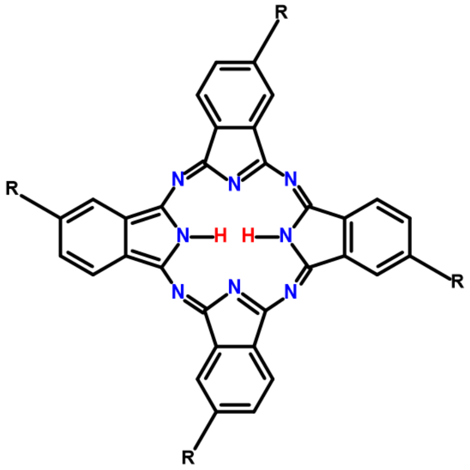
C_s	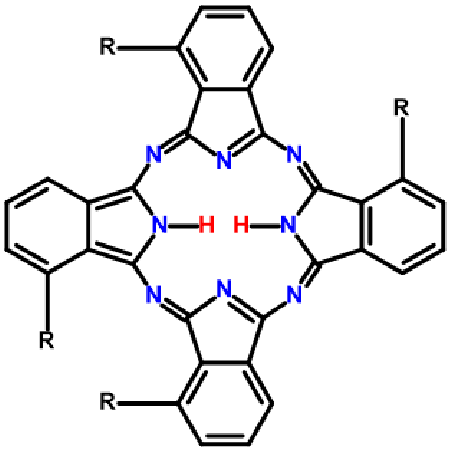	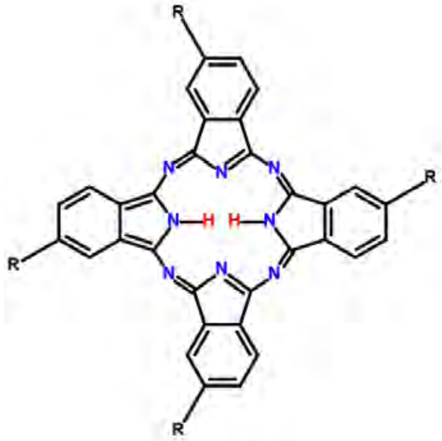

D_{2h}	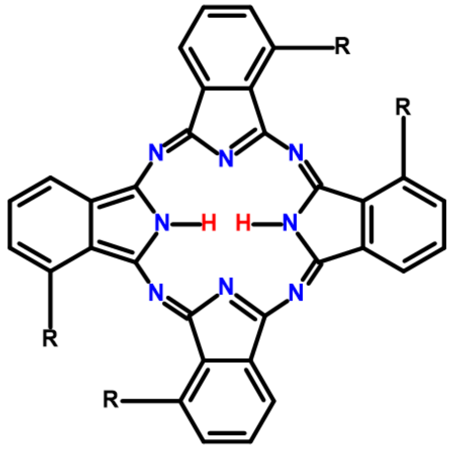	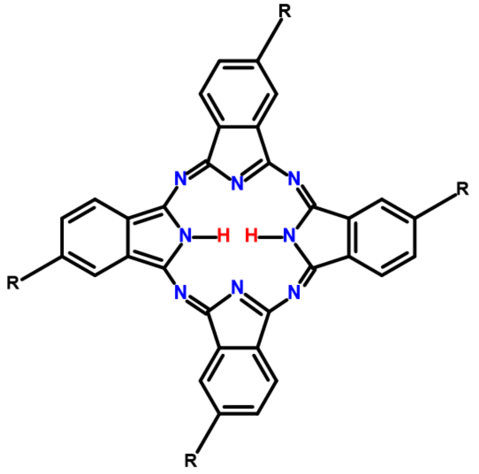
C_{2v}	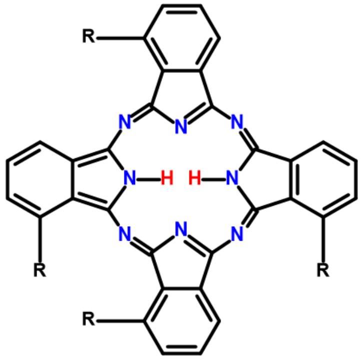	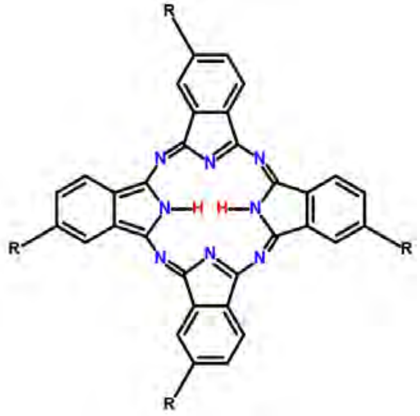

1.2.2 Ultraviolet-visible and Magnetic Circular Dichroism spectroscopy of Phthalocyanines

Phthalocyanines have shown use in various technologies due to their characteristic blue-green colour due to the $a_{1u} \rightarrow e_g$ and $a_{2u} \rightarrow e_g$ transitions[33]. They have large extinction coefficients and high fluorescence quantum yields[34]. The Ultraviolet-visible (UV/vis) absorption spectra of phthalocyanines, shown in **Figure 1.7** below, shows typical observed electronic transitions within the wavelength range of 650–800 and 300–450 nm referred to as the Q-band and B-band, respectively[33]. Phthalocyanines have strong emissions and these emissions can give information such as the Stokes shift, calculated as the difference between the maximum emission and the maximum absorption of the molecule[35].

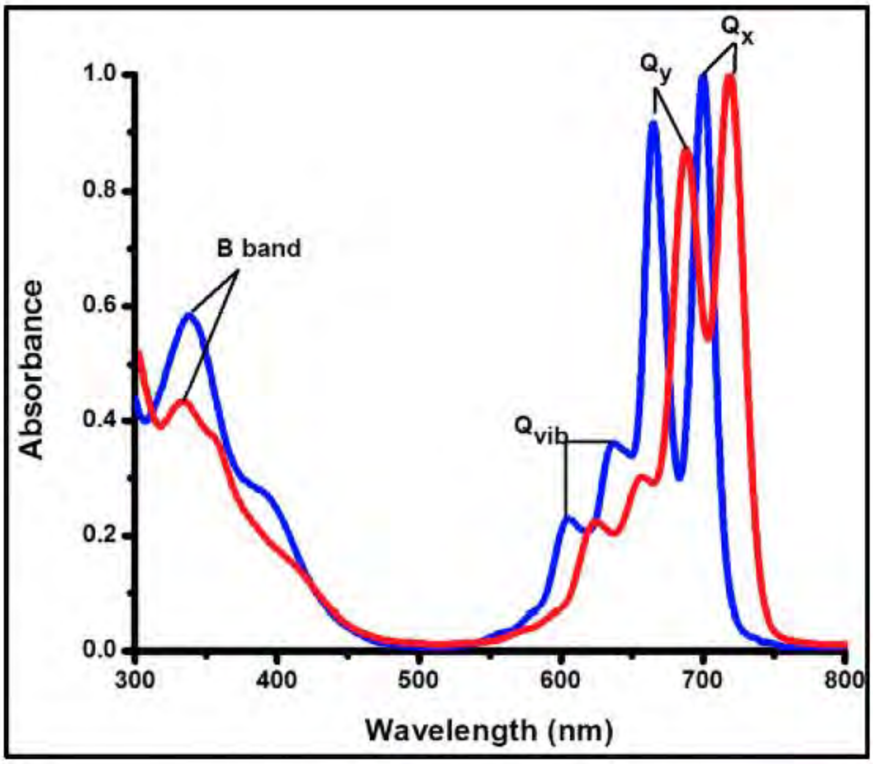

Figure 1.7: An example of a UV/Vis spectra free-base α (red) and β (blue) substituted phthalocyanines[30].

Phthalocyanines can have their properties altered by substitution at the peripheral alpha and beta positions as shown in **Figure 1.7**. Substitution at the more sterically hindered non peripheral alpha position also reduces aggregation tendencies more than substitution at the peripheral beta position. The substituents and metals chosen influence the spectroscopic properties of these phthalocyanines[36]. Substitution at the alpha-positions has been shown to have an increased effect on the energies of the four frontier molecular orbitals of the Pc π-system. The nature of the bonding and the lability of bonds between these substituents and core aromatic Pc system can be observed by using techniques such as mass spectrometry[37]. Assessment of fragmentation patterns can show the strength of bonds between these substituents and the core aromatic Pc system.

The electronic transitions displayed in the UV/Vis spectrum in **Figure 1.7** above can be attributed to electronic transitions between the highest occupied molecular orbital (HOMO) and lowest unoccupied molecular orbital (LUMO). There are two absorption bands noted: the B band (also known as the Soret band) which can be seen at 300-450 nm and the Q band which can be seen at 650-800 nm. These bands (shown in **Figure 1.7** and **Figure 1.8**) are due to π-π* transitions.

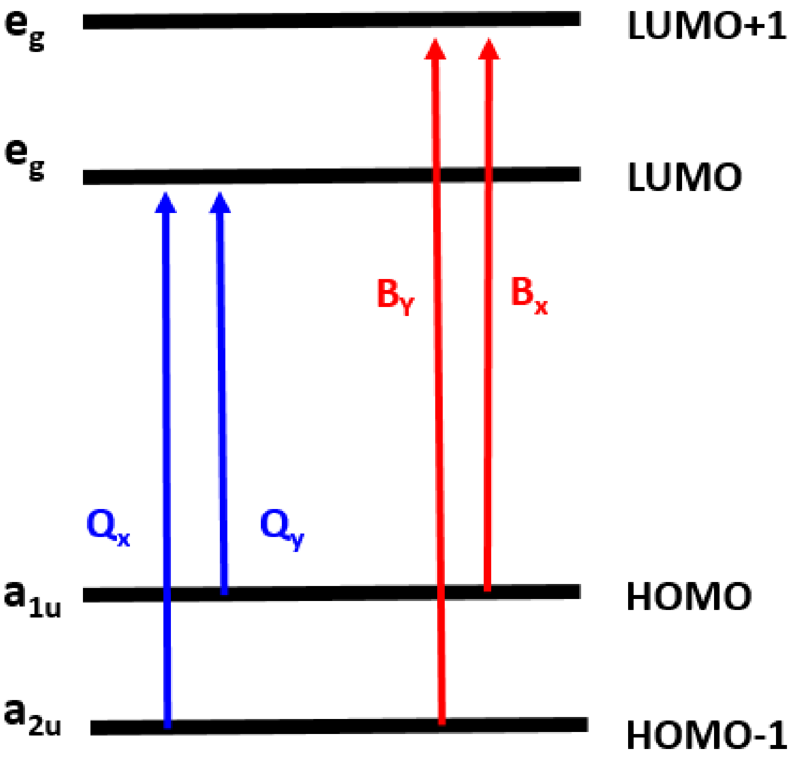

Figure 1.8: Gouterman's four-orbital linear model[38].

These bands were first explained by Martin Gouterman in his research into porphyrinoid absorption spectra[38]. It was deduced that these absorptions were a result of four frontier orbitals: a_{1u} , a_{2u} , e_g (two orbitals), designated using their point groups of symmetry. **Figure 1.9** shows the transitions from occupied orbitals (a_{1u} and a_{2u}) to unoccupied orbitals (e_g).

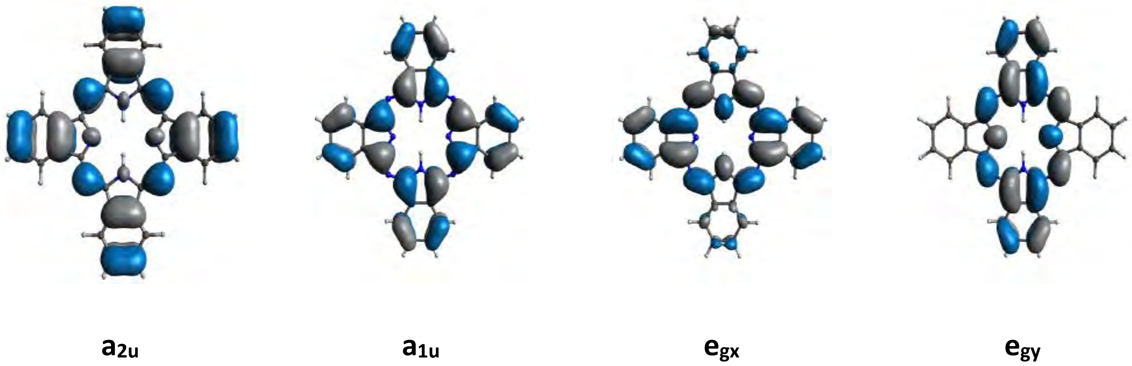

Figure 1.9: The Four Michl Orbitals[5].

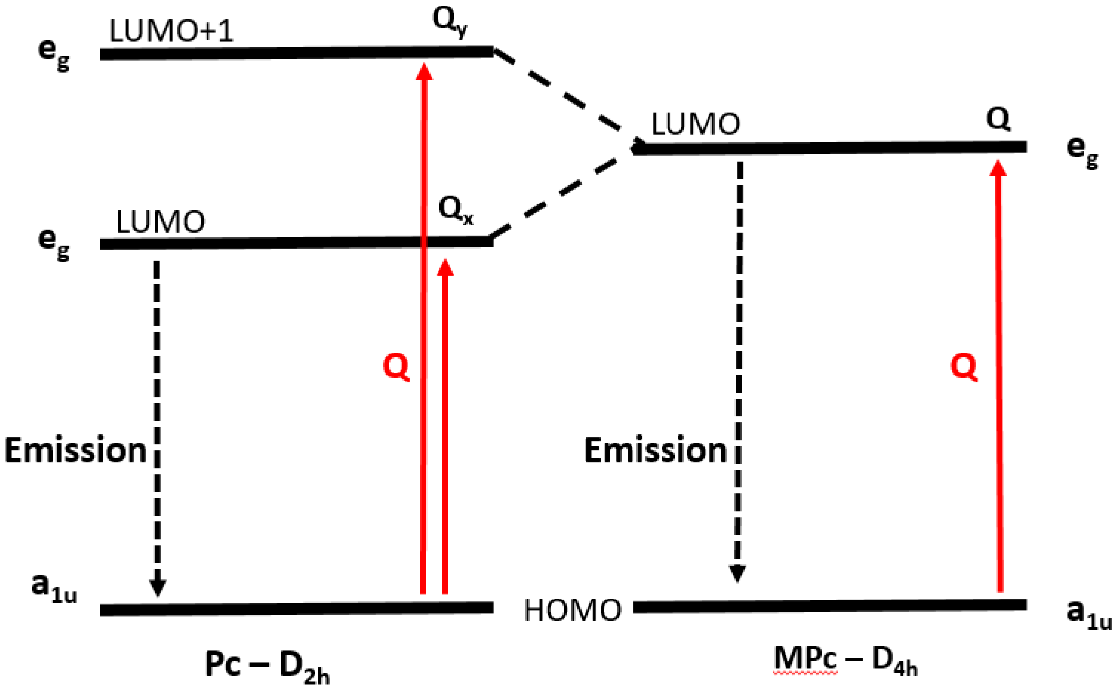

Figure 1.10: An orbital energy diagram of a metalated and unmetalated tetra-substituted Pc[39].

The split Q-band for unmetalated Pcs is as a result of the transitions a_{1u} ,→ e_g and a_{2u} → e_g. Upon metalation, these split peaks merge into one. As shown in **Figure 1.10** above, the MPc has a higher symmetry (D_{4h}) than the unmetalated Pc, as a result of having a four-fold axis of symmetry. As a result of having a higher symmetry, the e_g orbital becomes doubly degenerate. The transitions involving this doubly degenerate orbital are seen in **Figure 1.11** below. The disappearance of the split Q-band to form one peak of energy somewhere in between the two transitions prevalent in the unmetalated Pc.

There are also 2 vibronic bands (Q_{Vib}) that are due to these Q band transitions. These are less intense peaks that appear at higher energies. Upon inspecting **Figure 1.11** below, these two bands can be seen to the left of the Q-band on the unmetallated Pc, in both the unmetalated and metalated analogues of the Pc. In MPcs presence of both vibronic bands despite the single Q band peak is further proof of 2 transitions taking place in the formation of the single peak. The B band of the transitions of a_{1u} ,→ e_g and a_{2u} → e_g are seen at higher wavelengths.

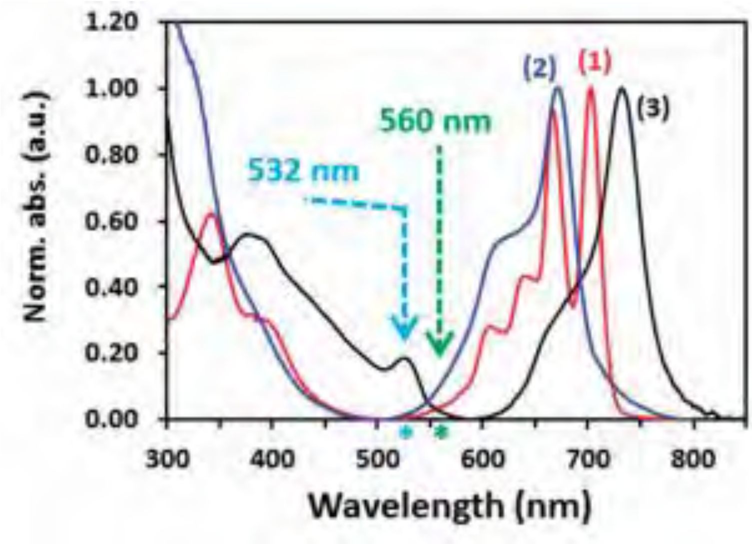

Figure 1.11: Absorption spectra of unmetalated H_2TPrOPhOPc (1), metalated CoTPrOPhOPc (2) and metalated MnTPrOPhOPc (3) in DCM[40].

Metallophthalocyanines and their non-metallic analogues are known to have low solubility in most organic solvents and they aggregate in various ways[36]. This lack of solubility can be addressed by introducing alkyl or alkoxy groups into the peripheral and nonperipheral positions of the phthalocyanine framework.

1.2.2.1 Magnetic Circular Dichroism

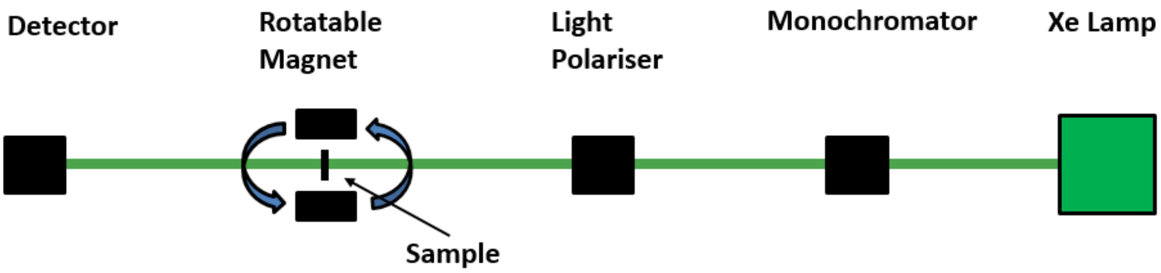

Figure 1.12: Basic layout for a Magnetic circular dichroism machine.

Magnetic Circular Dichroism (MCD) is a spectroscopic technique that has found itself useful in assigning spectra of porphyriniods, amongst which phthalocyanines are included[41]. The effects of ligands (especially on symmetry), the nature of the π-system in the sample and properties induced by varying the central metal, are all factors that have been studied using this technique[41, 42]. The redox and spin states of the central metal, including the redox state of the π-system and the spectral band polarisation, is the specific type of information that can be provided by the MCD technique[41]. Light, in this case being emitted from a Xenon lamp, is monochromated and polarised, and then passes through a sample in a strong magnetic field. MCD not only gives electronic absorption information typically received from UV/Vis spectroscopy, but because polarised light is being applied to the sample, information relating to the spin orientation of the molecular orbitals involved in the transitions seen in absorption spectroscopy is also present. This is not too dissimilar from Circular Dichroism (CD), but while in CD a sample is assessed in its differential absorbance of left (lcp) and right (rcp) circularly polarized light, the difference in the intensity of lcp and rcp light is measured by MCD spectroscopy[41]. To produce a MCD spectrum, two runs are done, each in opposite magnetic orientations, and these runs, when combined, are able to show the differences in asymmetric absorbance in the sample.

The basis of MCD is the interaction of electronic states with an applied magnetic field. Here, magnetic dipole moments are interface with the orbital and spin motion of the electrons[41]. As a result, the five electron quantum numbers form the theoretical basis for magnetic circular dichroism. These are the principal quantum number (*n*), angular/orbital quantum number (*l*), magnetic quantum number (m_l), spin quantum number (*s*) and spin angular momentum (m_s). Between spin and orbital angular momentum the electron spin has been found to be more efficient in terms of producing a magnetic moment[30].

The selection rule for lcp is Δm= +1 and for rcp is Δm= -1. As the sample is within an external magnetic field, the degeneracy of the orbital and spin states (that are in the same or opposite direction as the applied magnetic field) are lifted[41, 43]. The intensity of the MCD spectra is reliant on the association of ground and excited states *via* the magnetic and electric dipole moments[42]. The intensity of the MCD spectra can be represented by **Equation 31**:

$$I \sim A_1 \frac{-\delta f\ E}{\delta E} + B_0 + \frac{C_0}{kT}\ f\ E \qquad \textbf{(31)}$$

Where E is the energy coordinate in cm^{-1} and f is the normalized band shape function (typically assumed to be a Gaussian shaped curve). **Equation 31** is for a fully allowed electronic transition and uses the rigid-shift, Born-Oppenheimer and Franck-Condon approximations[30, 41].

Equation 31 above displays the letter *A*, *B* and *C*, each representing contributions to a MCD spectrum. In **Equation 31,** the terms *A* and *B* are independent of temperature, but *C* is temperature dependent. This is because the *C* term represents the orbital degenerate ground states that are temperature dependent. In **Equation 31,** the *B* term represents the combination of related states that are binded by a magnetic dipole transition moment which can be positive or negative. In **Equation 31,** the *A* term displays excited states that are split by the existence of a magnetic field *via* the Zeeman Effect[42, 44]. The MCD mechanism displaying the genesis of the *A*, *B* and *C* Faraday terms observed in MCD spectra is seen in **Figure 1.13**. Analytes of different symmetry, each result in the display of different terms. Molecules such as unmetalated Pcs have been known to give terms, while their metalated analogues display what are refered to as *A* terms due to their higher symmetry. The higher symmetry in these instances can cause degeneracy between split states, causing an *A* term.

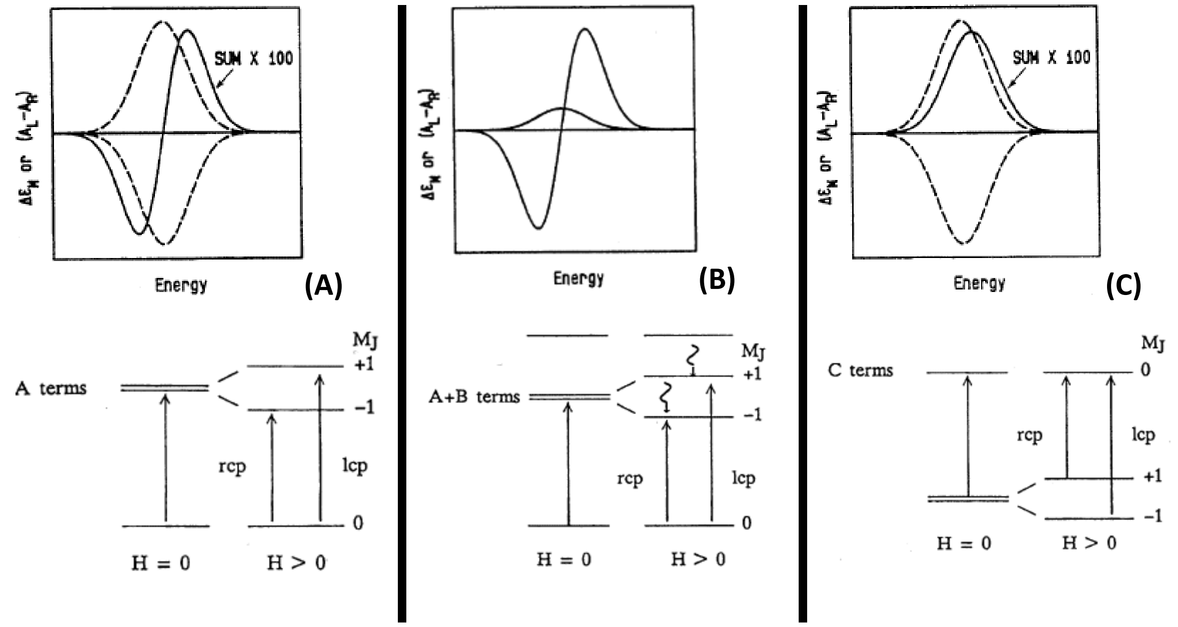

Figure 1.13: MCD mechanism displaying the genesis of the *A, B* and *C* Faraday terms observed in MCD spectra. The dashed curves represent the absorbance of left and right circularly polarized light (l/rcp)[42].

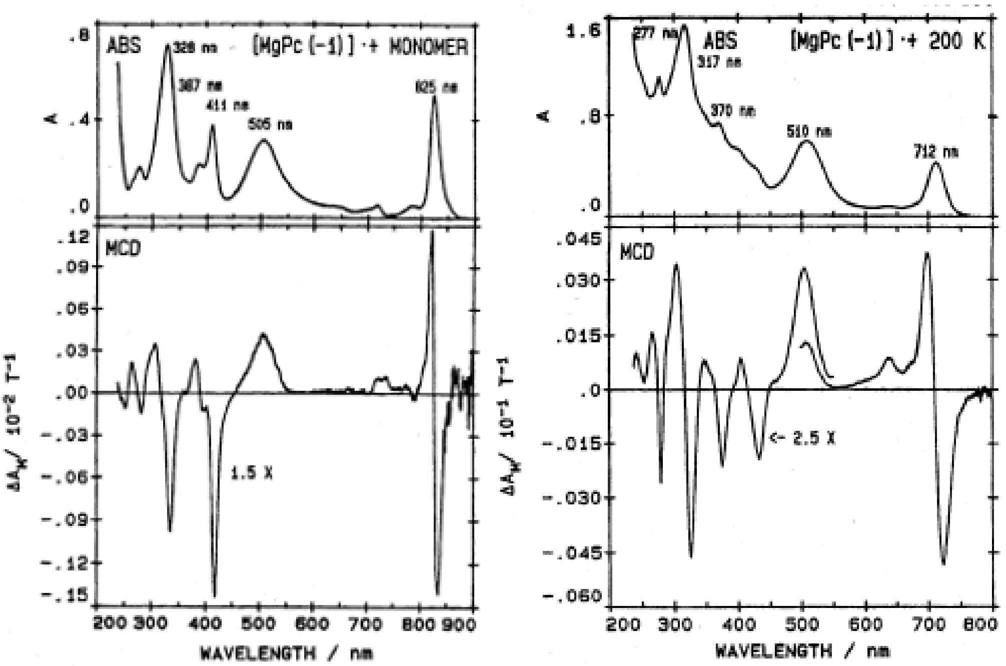

Figure 1.14: Electronic absorption and magnetic circular dichroism (MCD) spectra of [MgPc(−1)]+ prepared photochemically at room temperature and recorded at 298 K (monomer) and at 200 K (dimer) in dichloromethane[42].

A Faraday A1 (independent of temperature) is shown in the Q-band for both species in **Figure 1.14**. The Q-band region in this instance is easier to interprete than when compared to the B-band region. By use of spectral deconvolution of the spectral data of the monomeric species, an intense z-polarized B term was observed at 509nm instead of x/y-polarized A term like the other major bands in the MCD spectrum, giving evidence to the fact that the excited state is clearly non-degenerate.

MCD can complement UV/vis spectroscopy by displaying resolution between the Q_x and Q_y absorption bands. Q_x will absorb right-handed circularly polarised (rcp) light and Q_y left-handed circularly polarised (lcp) light.

1.2.2.2 Aggregation in Phthalocyanines

Phthalocyanines, generally having a planar structure, can form multiple supramolecular structures. Some of these structures have multiple phthalocyanine cores such as covalently bonded binuclear phthalocyanines, while others are as a result of supramolecular interactions and form as aggregates, where the process of the forming of this supramolecular structure is referred to as aggregation. Aggregation is seen when molecules in solution combine and associate themselves. The discovery of aggregation in organic dyes predates phthalocyanine's discovery[45]. A nonlinear relationship between concentration *vs* absorbance using the Beer-Lambert Law was observed in organic dyes. The discovery of this aggregation in phthalocyanines only took place once soluble phthalocyanines were available to be studied spectroscopically. Sometime in the 1930's, research detailing using peripheral substitution to solubilise phthalocyanines was seen[45]. This property of soluble phthalocyanines can be observed when using the UV/Vis spectrometer.

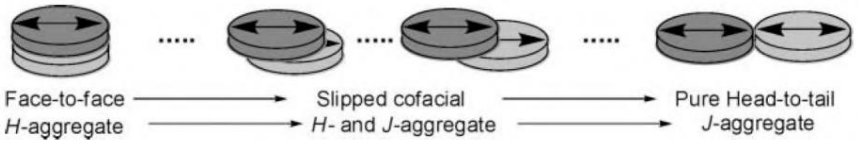

Figure 1.15: A diagram of face-to-face, slipped cofacial and head-to-tail aggregates[46].

Pcs orient themselves into H-aggregates, J-aggregates and intermediate aggregates (see **Figure 1.15** above)[46]. These aggregates form due to supramolecular interactions (known as π-π interactions) between the Pc rings, caused by an interaction between two or more electronic states[39, 47]. This interaction of electronic states effects the ground and excited states of the Pc, thus causing the effects seen in various types of spectroscopy. H-aggregates typically do not show fluorescent behaviour, thus limiting their use in telecoms technology, amongst other industries[48, 49]. J-aggregates however, can be useful in these instances. J-aggregates have been known to have an intense and narrow main absorption band, red-shifted when compared to a singular compound. They also have a strong photoluminescence that tends to show barely any Stokes shift[49, 50].

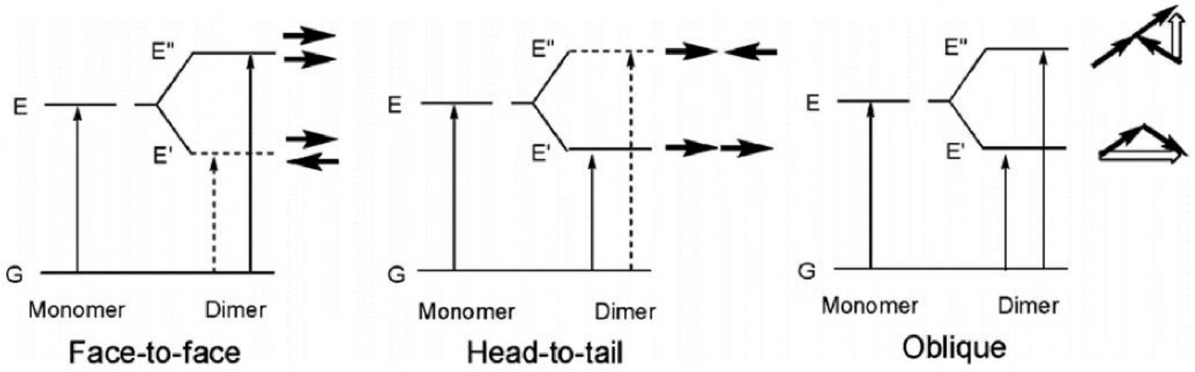

Figure 1.16: A qualitative orbital energy diagram for exciton coupling for monomer and dimer[51].

Figure 1.16 shows two types of dipoles, namely out of phase (E') and in phase (E"). When the dipoles are out of phase, the zero transition moment and the lowered energy combines and the forbidden transition to E' is seen, resulting in a bathochromically (red-shifted) shifted absorption spectrum[30, 46]. When the dipoles are in phase, the zero transition dipole moment and the raised energy combine and the forbidden transition to E" is seen, resulting in a hypsochromically (blue-shifted) shifted absorption spectrum[30, 46]. In the solid state, allowed transitions for both E' and E" can be observed. Proof of this is seen in hypsochromic and bathochromic shifts for both E' and E", otherwise known as Davydov splitting (see Oblique in **Figure 1.16**). Davydov splitting is defined as the splitting of bands in the electronic or vibrational spectra of crystals due to the presence of more than one equivalent molecular entity in the unit cell[30]. The reason for the feature to be observed in solid than compared to liquids is the reduction in the degrees of freedom in the solid state compared to the liquid state, potentially causing a non-zero transition moment.

Upon the formation of the aggregates, the distances between the Pc rings are so small that, as the molecules are excited, energy states interact such that two new exciton splitting energy levels are produced. As seen in **Figure 1.16**, the excitation to the energy levels (indicated by dashes) E' in the Face-to-face orientation and E’’ Head-to-tail orientation are forbidden. Both of these excitations are allowed in the Oblique orientation[46]. This splitting of energy states has shown to be dependent on the distance between the molecules, the orientation of their interaction and the intensity of the Pc transition moments[46].

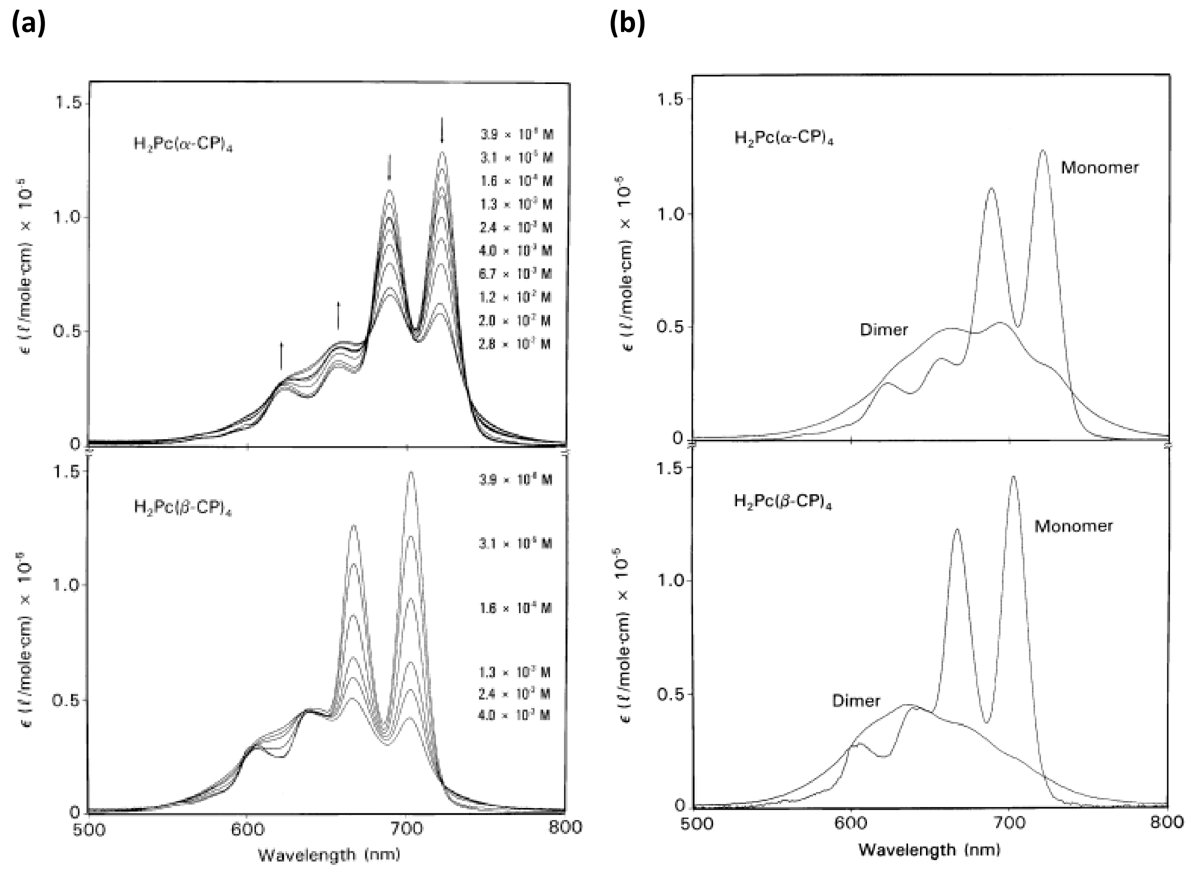

Figure 1.17: UV/Vis spectra of (a) free-base tetra-α-cumylphenoxy phthalocyanine ($H_2Pc(\alpha\text{-}CP)_4$) and free-base tetra-β-cumylphenoxy phthalocyanine ($H_2Pc(\beta\text{-}CP)_4$) displaying concentration dependence, and (b) $H_2Pc(\alpha\text{-}CP)_4$) and $H_2Pc(\beta\text{-}CP)_4$ in monomer and dimer form, all in chloroform solution[47].

A positive correlation between concentration vs absorbance using the Beer-Lambert Law can be seen in **Figure 1.17a**. The impact of aggregation on UV/Vis spectra can be seen in **Figure 1.17b**, where the molar absorption coefficient for the Q-band is altered due to dimerization. Substituents at the alpha and beta sites on the heterocyclic ring can cause the Q-band to be further shifted into the red and also cause a decrease in aggregation effects[36][45]. Alpha substituted Pcs have shown lower aggregation tendencies. This may be as a result of intramolecular sterics causing a warping of the generally planar structure of the Pc. The effect of the dimerization is also shown where there is a decrease in peak intensity.

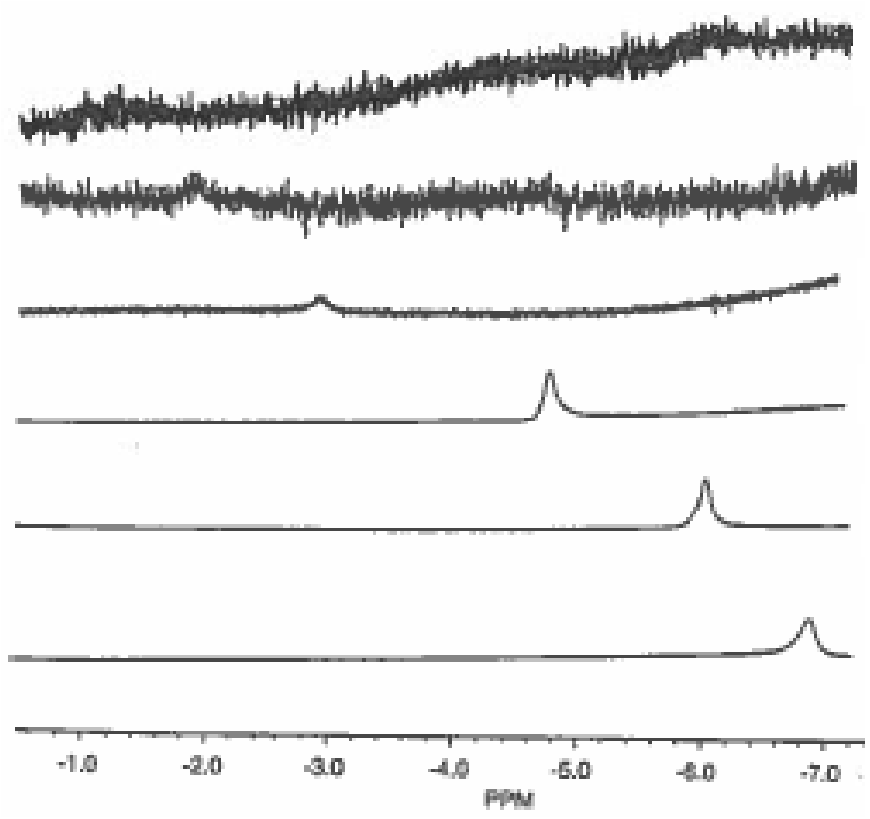

Figure 1.18: ^1H Nuclear Magnetic Resonance(NMR) spectra of cavity proton free-base tetra-β-cumylphenoxy phthalocyanine ($H_2Pc(β\text{-}CP)_4$) at concentrations of (a) 2.1 x 10^{-8} M, (b) 9.8 x 10^{-8} M, (c) 3.7 x 10^{-4} M, (d) 3.9 x 10^{-3} M, (e) 4.3 x 10^{-2} M, and (f) 1.5 x 10^{-1} M[45].

Another technique that can be used to analyse phthalocyanine aggregation is NMR[45]. In these instances, changes in chemical shift are seen with changing concentration. Aromatic rings are noted for deshielding and shielding capabilities based on the position of the nucleus relative to the aromatic ring. In **Figure 1.18**, an increase in ^1H shielding is seen with increasing concentration.

Metalation of the Pc is also a way to remedy the effects of aggregation on electronic spectra. The interaction between the central metal ion and the organic macrocycle determines the spin configuration of the complex[52]. These central metal ions allow for axial ligation, which increases solubility, reduces molecular aggregation and affects the dipole moment of the central metal–axial ligand bond in such a manner that changes to the electronic structure of the phthalocyanines are seen. The axial coordination can result in different molecular conformations. Among these conformations are planar, ruffled, dome, skew-domed and waved. The generally planar conformation of phthalocyanines has been shown to be contorted due to specific substituents due to conformational stress[53].

1.2.2.3 Fluorescence Spectroscopy

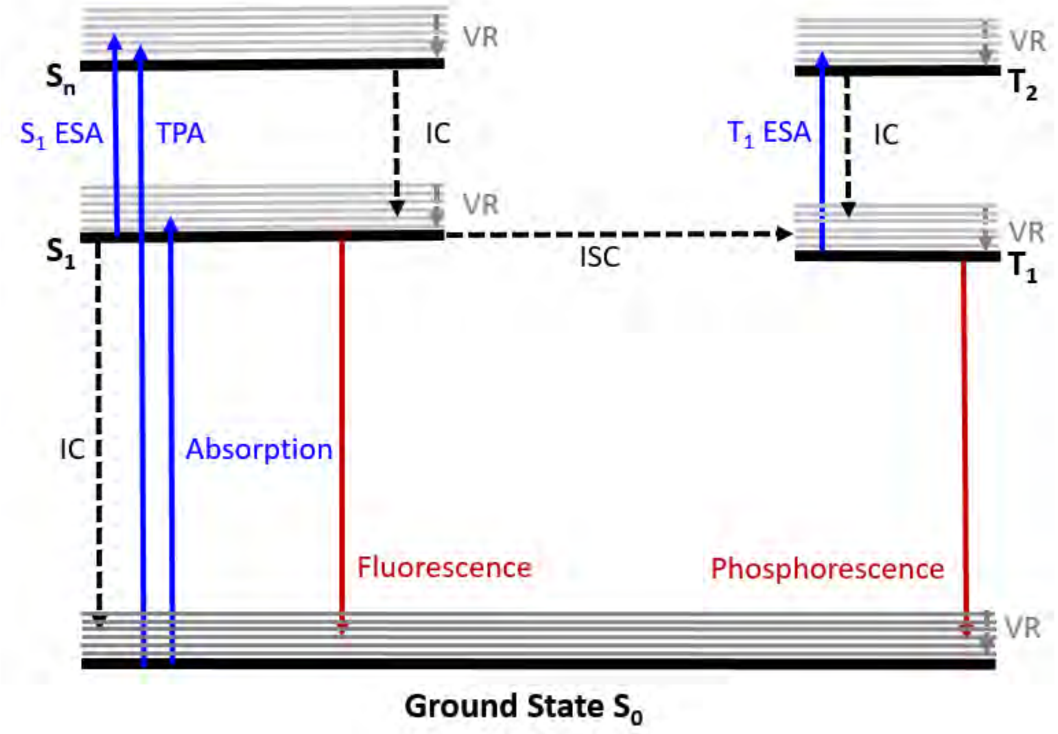

Figure 1.19: Perrin-Jablonski diagram mapping out photophysical transitions for a Pc[5].

Once electrons are excited, a number of photophysical transitions can occur. A Perrin-Jablonski diagram (**Figure 1.19**) can be used to clearly visualize some of these transitions. The electronic states represented in **Figure 1.19** tend to be in the order of 10 000 cm^{-1} , while the vibronic states are in the order of 100 cm^{-1}[54]. The electronic states shown include the ground state (S_0), the first singlet excited state (S_1), the nth singlet excited state (S_n), the first triplet state (T_1) and the nth triplet excited state (T_n). The grey lines show some vibronic states associated with each of those energy levels. The main transitions of absorption are shown in blue arrows and these include $S_0 \rightarrow S_1$ Ground State Absorption, $S_1 \rightarrow S_n$ Excited State Absorption (ESA), $S_0 \rightarrow S_n$ Two-Photon Absorption (TPA) and $T_1 \rightarrow T_n$ ESA. The main transitions of emission are shown in red arrows and these include: $S_1 \rightarrow S_0$ Fluorescence and $T_1 \rightarrow S_0$ Phosphorescence. The Intersystem System Crossing (ISC) and the Internal Conversion (IC) transitions are shown in black dashed arrows. In Pcs metalation using heavy atoms such as tin allows for the enhancement of ISC due to the presence of low lying d orbitals. An increase in spin-orbit coupling occurs, resulting in a crossover between electronic states of different multiplicity[55].

The vibronic relaxation pathways are shown in grey dashed arrows. Some transitions have been omitted to present more clarity and these include the B-band transitions and ICS transitions that occur at higher energies. In some molecules such as biacetyl, ICS has shown to be reversible[56], but since this transition has not been observed in Pcs, it was not included.

The transitions brought forward above and the relative energies associated with them are, as with electron absorption spectra, mainly effected by the chemical structure and the solvent it is contained in. The energy emitted is seen at a lower energy than the absorbance and excitation spectrums. This emission wavelength, as Kasha’s rule states, is independent of the excitation wavelength of the sample[57].

1.2.3 Time Correlated Single Photon Counting

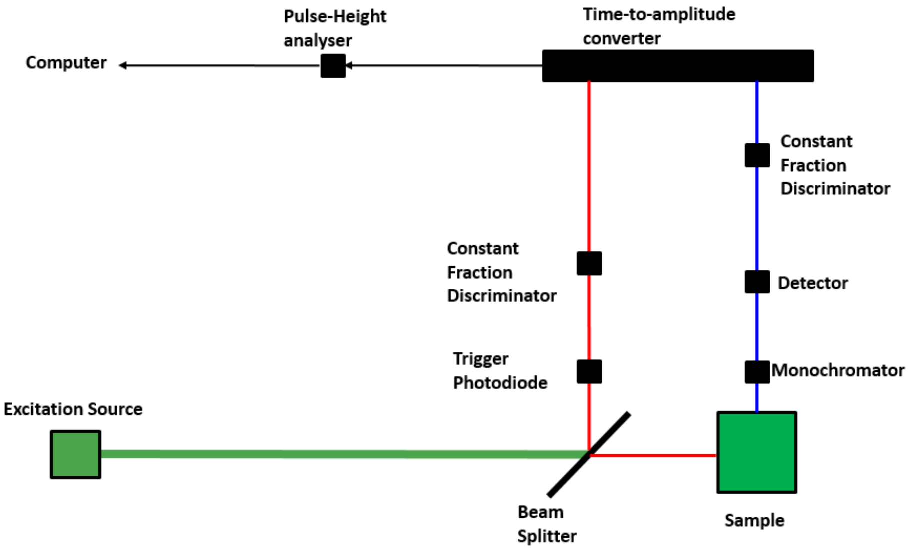

Figure 1.20: Basic layout for a Time Correlated Single Photon Counting machine.

Time Correlated Single Photon Counting (TCSPC) is a spectroscopic technique that is used to measure fluorescence decays. A basis layout of the instrument can be seen in **Figure 1.20** above. The technique can give spectroscopic information on singular analytes about their fluorescence emission, excitation populations, fluorescence lifetimes (τ) and rotational correlation time. These measurements typically provide information about the properties of the analyte in the singlet state.

An excitation source (typically a laser) emits a pulse (in the picosecond range) that excites the sample and primes the emission detector, and the resulting fluorescence emission is observed. The primed emission detector, placed in a position perpendicular to the excitation pathway, can then detect photons emitted from the sample. A time to amplitude converter performs the function of matching up the time of excitation to the beginning of the emission decay curve. The emission spectra for most materials tend to decay sharply after excitation.

Fluorescence anisotropy (*r*) measurements are based on the concept of polarized light causing photoselective excitation of fluorophores. Fluorophores preferentially absorb photons whose electric vectors are aligned parallel to the transition moment of the fluorophore[57]. They are typically used in the field of biochemistry. The maximum anisotropy may be effected by multiple factors, mainly rotational diffusion[57]. The viscosity of the matrix the analyte is submerged in affects this rotational diffusion. The anisotropy is given by the **Equation 32:**

$$r = \frac{r_O}{1+(\tau/\theta)} \tag{32}$$

Where r_o is the anisotropy that would be measured in the absence of rotational diffusion, and Θ is the rotational correlation time for the diffusion process. Rotational correlation time of the molecule can be used to determine the size and shape of the fluorophore. The larger an analyte, the slower its rotation in solution.

Fluorescence lifetime (τ) is defined as the average time between a fluorophore's excitation and its relaxation to the ground state[57]. There are two types of fluorescence measurements, being steady-state and time-resolved emission spectra (TRES). Steady-state is the most commonly used measurement. In the latter technique, a sample is illuminated with a continuous beam of light followed by a recording of the intensity of the emission. In TRES, the discrete times following excitation are shown. TRES measurements have been used to determine lifetime decays[57]. This data can be qualitative or quantitative. TRES has been utilised to provide resolution between emission spectra of two or more fluorophores in solution[58]. This spectra can be the result of different orientations, bonding and packing of the molecules. Both fluorescence lifetime and rotational correlation time measurements are achieved at the nanosecond timescale.

1.2.4 Z-scan

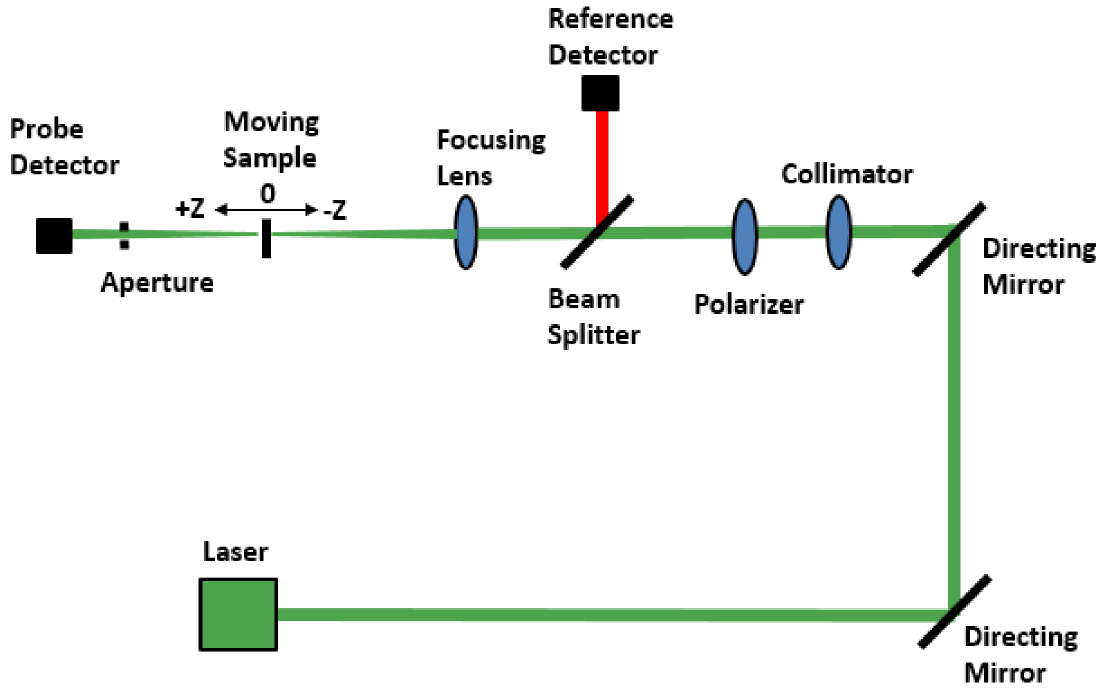

Figure 1.21: Basic layout for a Z-Scan.

Z-Scan is a spectroscopic technique used to measure NLO properties such as nonlinear absorption and nonlinear refraction. The technique allows for the analysis of the transmittance of a sample with respect to its position Z on the position of the focal plane (see **Figure 1.21**)[59]. Slow nonlinearities such as thermal refraction, electrostriction and population redistribution caused by linear absorption can be analysed by using Z-Scan[60]. There are two modes in this setup that are used: Open aperture and Closed aperture. In open aperture mode, the nonlinear absorption coefficient is measured, whereas in closed aperture mode, the nonlinear index refraction is measured. This aperture is placed in front of the probe detector and adjusted based on the mode of analysis taking place.

Table 1.3: Examples of Nonlinear Optical parameters from literature

Substituent Group	Position	Symmetry	Im[x^3](esu)	Im[y](esu)	Source
4-Tertbutyl-phenoxy 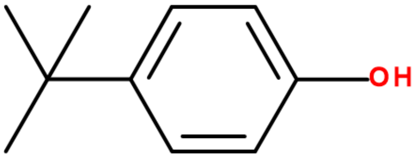	Alpha	C_{4h}		5.25E-37	[5]
	Alpha	C_{2v}		3.82E-37	
	Alpha	C_s		2.67E-37	
	Alpha	D_{2h}		2.65E-37	
4-Tertbutyl-phenoxy 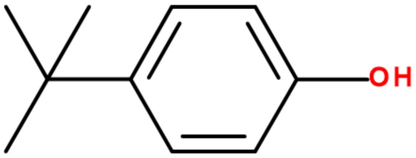	Beta	C_{4h}	35.55E-8	59.71E-28	[29]
	Beta	D_{2h}	43.74E-8	66.29E-28	
	Beta	C_s	30.09E-8	37.68E-28	
	Beta	C_{2v}	48.44E-8	62.30E-28	
Ethylthioxy 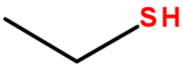	Beta	Octa	5.20E-15	2.35E-34	[61]
	Beta	Asymmetric	11.5E-15	16.6E-34	
	Beta + Co	Octa	5.12E-15	1.02E-34	
	Beta + Co	Asymmetric	23.8E-15	17.5E-34	
	Beta + Zn	Octa	7.01E-15	4.13E-34	
	Beta + Zn	Asymmetric	11.4E-15	8.44E-34	
4-(Methylsulfanyl)thiophenoxy 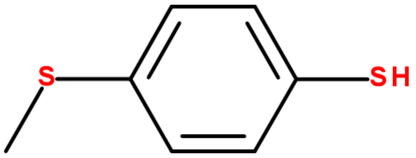	Alpha	Asymmetric	1.75E-7	10.5E-27	[62]
	Alpha + Cu	Asymmetric	3.22E-7	0.97E-27	
	Alpha + Co	Asymmetric	0.81E-7	0.95E-27	
	Alpha + Ni	Asymmetric	0.85E-7	0.22E-27	
4-Tertbutyl-phenoxy 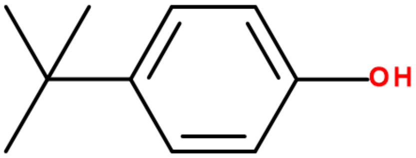	Alpha	C_s	2.30	6.80E-32	[30]
	Alpha	C_{4h}	3.43	2.32E-31	
	Alpha	D_{2h}	1.38	2.11 E-31	
	Alpha	C_{2v}	2.91	1.11 E-31	

The Pcs shown in **Table 1.3** vary from unmetalated to metalated and also have different symmetries based on substitution. Symmetry highly augments the NLO properties of the Pc, than when compared to metalation. The Pc with the lowest symmetry Cs, displayed the lowest Im[γ] value.

1.2.5 Dipolar *vs* Octuploar

Density Functional Theory is capable of calculating a range of different parameters relating to light interacting with matter. Some of those parameters include tensoral components directly related to the aforementioned dipolar and octopolar contributions to the Hyper-Rayleigh scattering response coeffiecient (β_{HRS}). Symmetry dictates the number of nonzero components in the β tensor and as a result is of high interest when defining the NLO properties of a material. The number of electrons in the system affects the magnitude of the values of the dipolar contribution and the octopolar contribution. **Equations 33-38** are used to calculate the β_{HRS} response[63]:

$$\beta_{HRS}(-2\omega;\omega,\omega) = \sqrt{\langle\beta^2_{ZZZ}\rangle + \langle\beta^2_{ZXX}\rangle} \tag{33}$$

Where $\langle\beta^2_{ZZZ}\rangle$ and $\langle\beta^2_{ZXX}\rangle$ are the orientation averages of the molecular β tensor components. The tensors $\langle\beta^2_{ZZZ}\rangle$ and $\langle\beta^2_{ZXX}\rangle$ are calculated using **Equation 34** and **Equation 35**:

$$\langle\beta^2_{ZZZ}\rangle = \frac{1}{7}\sum_{\zeta}^{x,y,z}\beta^2_{\zeta\zeta\zeta} + \frac{6}{35}\sum_{\zeta\neq\eta}^{x,y,z}\beta_{\zeta\zeta\zeta}\beta_{\zeta\eta\eta} + \frac{9}{35}\sum_{\zeta\neq\eta}^{x,y,z}\beta^2_{\eta\zeta\zeta} + \frac{3}{35}\sum_{\zeta\neq\eta\neq\xi}^{x,y,z}\beta_{\eta\zeta\zeta}\beta_{\eta\xi\xi} + \frac{2}{35}\sum_{\zeta\neq\eta\neq\xi}^{x,y,z}\beta^2_{\zeta\eta\xi} \tag{34}$$

$$\langle\beta^2_{ZXX}\rangle = \frac{1}{35}\sum_{\zeta}^{x,y,z}\beta^2_{\zeta\zeta\zeta} - \frac{2}{105}\sum_{\zeta\neq\eta}^{x,y,z}\beta_{\zeta\zeta\zeta}\beta_{\zeta\eta\eta} + \frac{11}{105}\sum_{\zeta\neq\eta}^{x,y,z}\beta^2_{\eta\zeta\zeta} - \frac{1}{105}\sum_{\zeta\neq\eta\neq\xi}^{x,y,z}\beta_{\eta\zeta\zeta}\beta_{\eta\xi\xi} + \frac{4}{105}\sum_{\zeta\neq\eta\neq\xi}^{x,y,z}\beta^2_{\zeta\eta\xi} \tag{35}$$

The depolarisation ratio (DR), which gives insight into molecular geometry, is calculated by the ratio $DR = \frac{\langle\beta^2_{ZZZ}\rangle}{\langle\beta^2_{ZXX}\rangle}$. $\langle\beta^2_{HRS}\rangle$ can be seen as the sum of the dipolar and octupolar tensorial components, seen in **Equations 36-38**:

$$\beta_{HRS} = \sqrt{\langle \beta_{HRS}^2 \rangle} = \sqrt{\tfrac{10}{45}\left|\beta_{J=1}\right|^2 + \tfrac{10}{105}\left|\beta_{J=3}\right|^2} \qquad \textbf{(36)}$$

$$\left|\beta_{J=1}\right|^2 = \tfrac{3}{5}\sum_{\zeta}^{x,y,z} \beta_{\zeta\zeta\zeta}^2 + \tfrac{6}{5}\sum_{\zeta\neq\eta}^{x,y,z} \beta_{\zeta\zeta\zeta}\beta_{\zeta\eta\eta} + \tfrac{3}{5}\sum_{\zeta\neq\eta}^{x,y,z} \beta_{\eta\zeta\zeta}^2 + \tfrac{3}{5}\sum_{\zeta\neq\eta\neq\xi}^{x,y,z} \beta_{\eta\zeta\zeta}\beta_{\eta\xi\xi} \qquad \textbf{(37)}$$

$$\left|\beta_{J=3}\right|^2 = \tfrac{2}{5}\sum_{\zeta}^{x,y,z} \beta_{\zeta\zeta\zeta}^2 - \tfrac{6}{5}\sum_{\zeta\neq\eta}^{x,y,z} \beta_{\zeta\zeta\zeta}\beta_{\zeta\eta\eta} + \tfrac{12}{5}\sum_{\zeta\neq\eta}^{x,y,z} \beta_{\eta\zeta\zeta}^2 - \tfrac{3}{5}\sum_{\zeta\neq\eta\neq\xi}^{x,y,z} \beta_{\eta\zeta\zeta}\beta_{\eta\xi\xi} + \sum_{\zeta\neq\eta\neq\xi}^{x,y,z} \beta_{\zeta\eta\xi}^2 \qquad \textbf{(38)}$$

The ratios ([$\phi_{j=1} = 1/(1+\rho)$] for Dipolar) and ([$\phi_{j=3} = \rho/(1+\rho)$] for Octupolar) are used to calculate the corresponding dipolar and octupolar contributions to hyperpolarizability tensor β where the nonlinear anisotropy parameter $\rho = \left|\beta_{J=1}\right| / \left|\beta_{J=3}\right|$. Nonlinear anisotropy parameter values for pure dipolar components tend to be closest to 0, while the pure octupolar can reach up to ∞[62].

The theoretical normalized HRS intensity can be determined by using Bersohn's expression[63], which assumes a general elliptically polarised incident light propagating along the X direction, the intensity of the harmonic light is scattered at 90° along the Y direction and the vertically polarised light along the Z-axis. The orientational averages $\langle (\beta_{ZXZ}\beta_{ZZX})^2 - 2\beta_{ZZZ}\beta_{ZXX} \rangle$ are seen in **Equation 39**:

$$\langle (\beta_{ZXZ}\beta_{ZZX})^2 - 2\beta_{ZZZ}\beta_{ZXX} \rangle = 7\langle \beta_{ZXX}^2 \rangle - \langle \beta_{ZZZ}^2 \rangle = -\tfrac{2}{45}\left|\beta_{J=1}\right|^2 + \tfrac{22}{105}\left|\beta_{J=3}\right|^2 \qquad \textbf{(39)}$$

Due to symmetry constraints there is no permanent dipole moment for octupolar molecules, hence octupolar molecules present an isotropic β tensor. The octupolar contribution to the total β_{HRS} is the main contributor.

1.3 Methodology and Goals

Scheme 1.2: Methodology

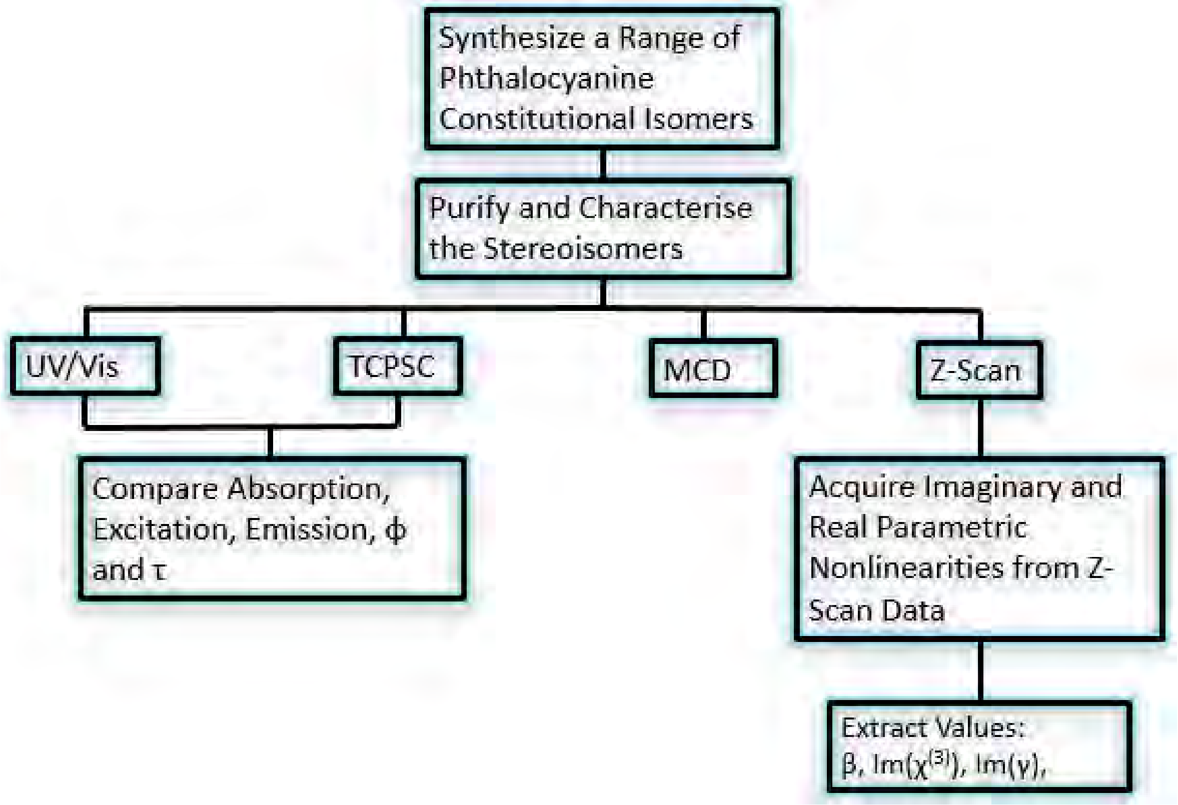

The work aims to investigate the effects of symmetry on NLO properties of Pcs constitutional isomers using a combination of computational methods and z-scan analysis of cross sections. The goals include the synthesis of these phthalocyanines with the corresponding purification and characterisation. The phthalocyanines to be synthesized and studied are 3 different octa-substituted Pcs (1 alpha and 2 beta) and 4 constitutional isomers. Upon isolation, the Pcs shall be studied spectroscopically and computationally to determine, and provide, a further understanding of the NLO features of these materials. This process is illustrated in **Scheme 1.2**.

Chapter 2: Experimental

2.1 Materials

Methanol, chloroform, dichloromethane, hexane and acetone were purchased from Saar Chem.

Hexanol, 4-tertbutyl phenol, 2,3-dicyanohydroquinone, 1-pentane thiol and octanol were purchased from Sigma-Aldrich.

Acetic acid and magnesium sulphate were purchased from B&M Scientific.

Dimethyl formamide (DMF) was purchased from Associated Chemical Enterprises.

Potassium carbonate was purchased from Minema.

2.2 Synthesis of Phthalonitriles

2.2.1 Synthesis of 4,5-bis(4-tertbutyl-phenol)- phthalonitrile

4,5-dichloro phthalonitrile (0.5173.g, 2.62 x 10^{-3}mol) was dissolved in a mixture of dry DMF (4.74g, 6.48 x 10^{-2}mol), anhydrous potassium carbonate (0.4g, 2.89 x 10^{-3} mol) and 4-tert-butyl phenol (0.8544g, 5.68 x 10^{-3} mol) in a 20mL round-bottomed flask equipped with a stirrer bar. The mixture was purged with nitrogen gas for 5 mins and then a septum with a nitrogen gas balloon was attached. The mixture was stirred for 12 hours during which the mixture turned dark brown. Ice water was added to precipitate the product out of solution and the mixture was stirred until the ice melted. The mixture was then filtered under vacuum. The raw product was then recrystallized in methanol. The conversion of 4,5-dichloro phthalonitrile to **1** is seen in **Scheme 2.1** below.

Scheme 2.1: Synthesis of 4,5-bis(4-tertbutyl-phenol)-phthalonitrile

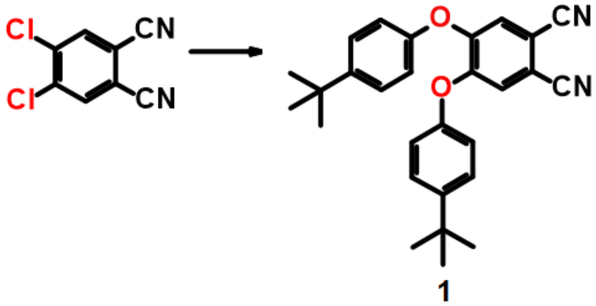

1

Reaction Yield: 0.755g, 68%; IR[(KBr) v_{max}/cm^{-1}]: 1201 cm^{-1}, 1011 cm^{-1}(Ph-O-Ph); 2233 cm^{-1}(C≡N); MALTDI-TOF- 2,3-Naphthalenedicarboxylic acid m/z - Expected m/z=424/Experimental m/z=424.3

2.2.2 Synthesis of 4,5-bis(pentylsulfanyl)-phthalonitrile

4,5-dichloro phthalonitrile (0.5025g, 2.62 x 10^{-3}mol) was dissolved in a mixture of dry DMF (4.74g, 6.48 x 10^{-2}mol) and anhydrous potassium carbonate (0.4g, 2.89 x 10^{-3} mol) in a 20ml round-bottomed flask equipped with a stirrer bar. The mixture was purged with nitrogen gas for 5 mins and then a septum with a nitrogen gas balloon was attached. 1-Pentanethiol (0.84g, 0.806 x 10^{-3} mol) was added quickly *via* syringe. The mixture was stirred for 12 hours during which the mixture turned dark yellow. Ice water was added to precipitate the product out of solution and the mixture was stirred until the ice melted. The mixture was then filtered under vacuum and the residue washed with brine (3 x 30mL) and extracted with chloroform (3 x 30mL).The combined organic layers were dried over anhydrous magnesium sulphate, filtered and evaporated. The residue was then purified by column chromatography . The raw product was eluted from the column (silica gel in choloroform) with chloroform, and recrystallized in methanol. The conversion of 4,5-dichloro phthalonitrile to **2** is seen in **Scheme 2.2** below.

Scheme 2.2: Synthesis of 4,5-bis(pentylsulfanyl)-phthalonitrile

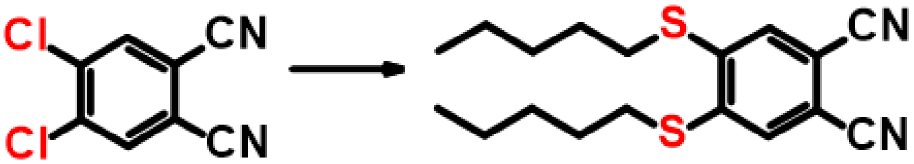

2

Reaction Yield: 0.461g, 53%; IR[(KBr) v_{max}/cm^{-1}]: 730 cm^{-1}(C-S); 2229 cm^{-1}(C≡N) MALTDI-TOF-2,3-Naphthalenedicarboxylic acid m/z - Expected m/z=332/Experimental m/z=330.0[M-2H]

2.2.3 Synthesis of 3,6-bis(pentylsulfanyl)- phthalonitrile

2,3-Dicyano tosylhydroquinone (0.644g, 1.42 x 10^{-3}mol) was dissolved in a mixture of dry DMF (4.74g, 6.48 x 10^{-2}mol) and anhydrous potassium carbonate (0.4g, 2.89 x 10^{-3} mol) in a 20ml round-bottomed flask equipped with a stirrer bar. The mixture was purged with nitrogen gas for 5 mins and then a septum with a nitrogen gas balloon was attached. 1-Pentanethiol (0.84g, 0.806 x 10^{-3} mol) was added quickly *via* syringe. The mixture was stirred for 12 hours during which the mixture turned yellow. Ice water was added to precipitate the product out of solution and the mixture was stirred until the ice melted. The mixture was then filtered under vacuum and the residue washed with brine (3 x 30mL) and extracted with chloroform (3 x 30mL).The combined organic layers were dried over anhydrous magnesium sulphate, filtered and evaporated. The residue was then purified by column chromatography. The raw product was eluted from the column (silica gel in choloroform) with chloroform, and then recrystallized in methanol. The conversion of 2,3-dicyano tosylhydroquinone to **3** is seen in **Scheme 2.3** below.

Scheme 2.3: Synthesis of 3,6-bis(pentylsulfanyl)- phthalonitrile

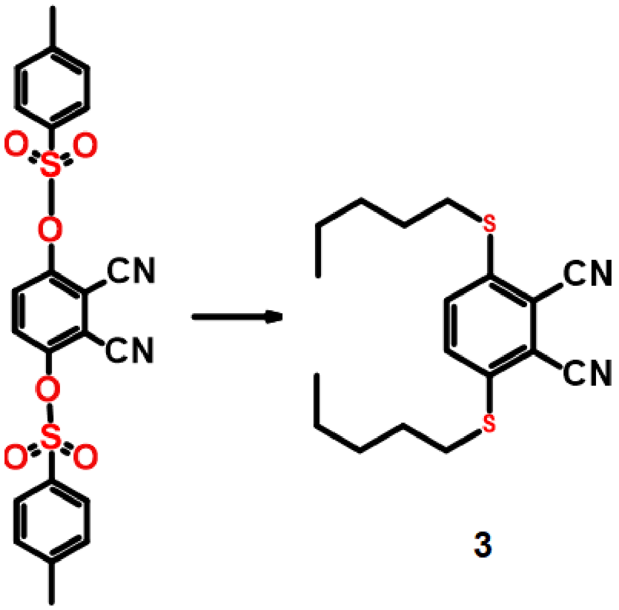

Reaction Yield: 0.226g, 48%; IR[(KBr) v_{max}/cm^{-1}]: 725 cm^{-1} (C-S), 2220 cm^{-1} (C≡N); MALTDI-TOF-2,3-Naphthalenedicarboxylic acid m/z - Expected m/z=332/Experimental m/z=:331[M-H]

2.2.4 Synthesis of 3-pentylsulfanyl-phthalonitrile

3-Nitro phthalonitrile (0.776g, 4.48 x 10^{-3}mol) was dissolved in a mixture of dry DMF (4.74g, 6.48 x 10^{-2}mol) and anhydrous potassium carbonate (0.4g, 2.89 x 10^{-3} mol) in a 20mL round-bottomed flask equipped with a stirrer bar. The mixture was purged with nitrogen gas for 5 mins and then a septum with a nitrogen gas balloon was attached. 1-Pentanethiol (0.84g, 0.806 x 10^{-3} mol) was added quickly *via* syringe. The mixture was stirred for 12 hours during which the mixture turned yellow. Ice water was added to precipitate the product out of solution and the mixture was stirred until the ice melted. The mixture was then filtered under vacuum and the residue washed with brine (3 x 30mL) and extracted with chloroform (3 x 30mL).The combined organic layers were dried over anhydrous magnesium sulphate, filtered and evaporated. The residue was then purified by column chromatography . The raw product was eluted from the column (silica gel in choloroform) with chloroform, and recrystallized in methanol. The conversion of 3-nitro phthalonitrile to **4** is seen in **Scheme 2.4** below.

Scheme 2.4: Synthesis of 3-pentylsulfanyl-phthalonitrile

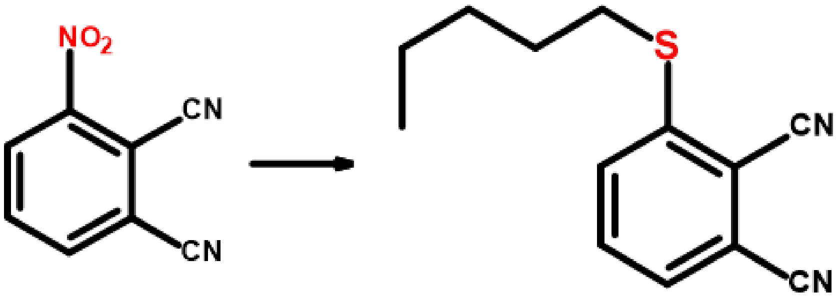

4

Reaction Yield: 0.566g, 55%; IR[(KBr) v_{max}/cm^{-1}]: 689 cm^{-1}(C-S), 2225cm^{-1} (C≡N); MALTDI-TOF-alpha cyano-4-hydroxycinnamic acid m/z - Expected m/z=230/Experimental m/z=229.1

2.3 Synthesis of Phthalocyanines

2.3.1 Synthesis of β-$H_2Pc(tert\text{-}BPh)_8$

0.256g of **1** and a catalytic amount of lithium in hexanol (1 mL) was stirred under nitrogen gas at 140 °C for 8 hours. After cooling, the raw product was precipitated in methanol and separated by column chromatography (silica gel, chloroform) to yield the phthalocyanine after evaporation. The conversion of **1** to **5** is seen in **Scheme 2.5** below.

Scheme 2.5: Synthesis of β-$H_2Pc(tert\text{-}BPh)_8$

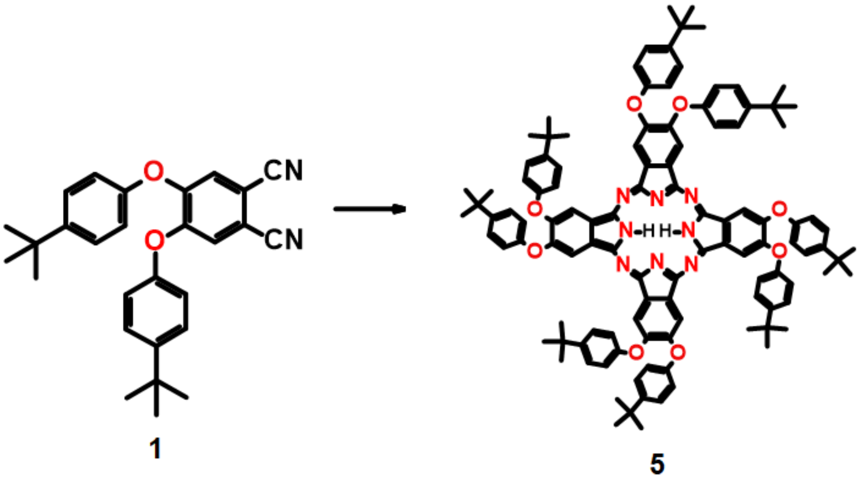

IR[(KBr) ν_{max}/cm^{-1}]: 2916 cm^{-1}, 2849 cm^{-1}(N-H); MALTDI-TOF- 2,3-Naphthalenedicarboxylic acid m/z - Expected m/z=1700/Experimental m/z=:1702[M+2H]. UV/Vis: λ_{max} [nm](logε): 702 (5.10), 669 (5.08), 395 (4.59), 345 (4.95).

2.3.2 Synthesis of β-$H_2Pc(SC_5H_{11})_8$

0.115g of **2** and a catalytic amount of lithium in octanol (1 mL) was stirred under nitrogen gas at 140 °C for 2 hours. After cooling, the raw product was precipitated in methanol and separated by column chromatography (silica gel, chloroform) to yield the phthalocyanine after evaporation. The conversion of **2** to **6** is seen in **Scheme 2.6** below.

Scheme 2.6: Synthesis of β-$H_2Pc(SC_5H_{11})_8$

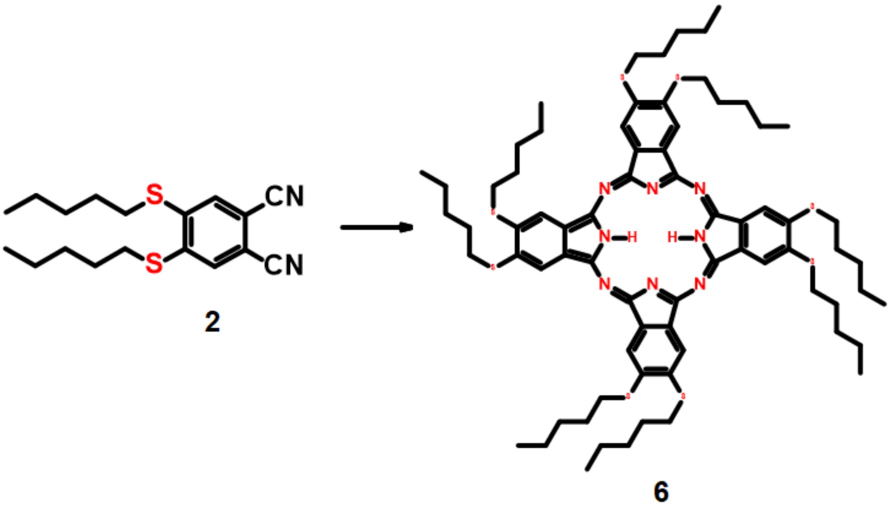

IR[(KBr) v_{max}/cm^{-1}]: 3283 cm^{-1}, 2913 cm^{-1}, 2844 cm^{-1} (N-H); MALTDI-TOF- 2,3-Naphthalenedicarboxylic acid m/z - Expected m/z=1330/Experimental m/z=:1348[See Section 3.2.1] UV/Vis: λ_{max} [nm](logε): 705(4.20), 669(4.29), 335(4.39), 306(4.44).

2.3.3 Synthesis of α-$H_2Pc(SC_5H_{11})_8$

0.107g of **3** and a catalytic amount of lithium in octanol (1 mL) was stirred under nitrogen gas at 140 °C for 2 hours. After cooling, the raw product was precipitated in methanol and separated by column chromatography (silica gel, chloroform) to yield the phthalocyanine after evaporation. The conversion of **3** to **7** is seen in **Scheme 2.7** below.

Scheme 2.7: Synthesis of α-$H_2Pc(SC_5H_{11})_8$

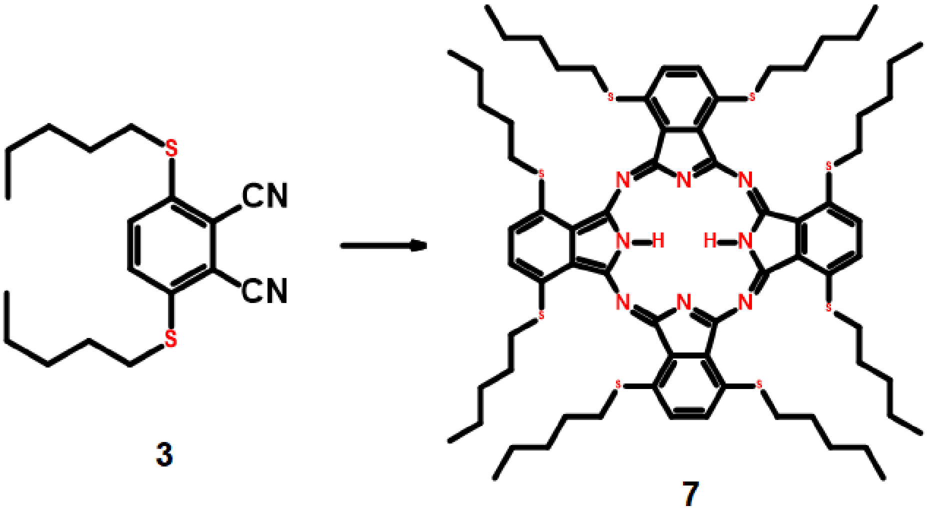

IR[(KBr) v_{max}/cm^{-1}]: 2915 cm^{-1}, 2846 cm^{-1} (N-H); MALTDI-TOF- 2,3-Naphthalenedicarboxylic acid m/z - Expected m/z=1330/Experimental m/z=:1296[See Section 3.2.1] UV/Vis: λ_{max} [nm](logε): 777(3.03), 337(3.27).

2.3.4 Synthesis of α-$H_2Pc(SC_5H_{11})_4$

0.256g of **4** and a catalytic amount of lithium in octanol (1 mL) was stirred under nitrogen gas at 140 °C for 2 hours. After cooling, the raw product was precipitated in methanol and separated by column chromatography (silica gel, chloroform) to yield the phthalocyanine after evaporation. During separation, the first 3 layers were eluted with chloroform and the 4th layer with chloroform:methonol of 90:10. Chloform:hexane mixtures were used to provide resolution between the layers. The conversion of **4** to **8** is seen in **Scheme 2.8** below.

Scheme 2.8: Synthesis of α-$H_2Pc(SC_5H_{11})_4$

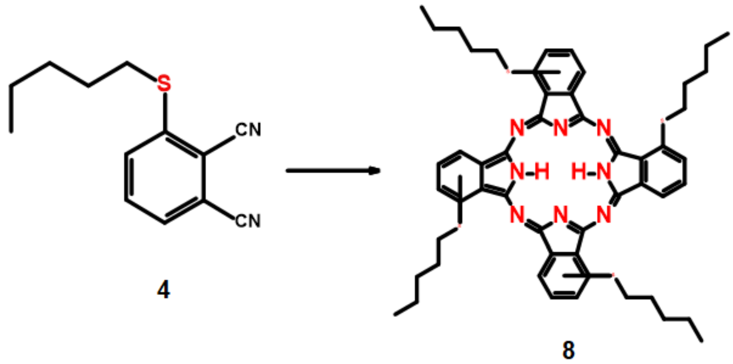

4

8

IR[(KBr) v_{max}/cm^{-1}]: 2917 cm^{-1}, 2846 cm^{-1} (N-H); MALTDI-TOF- 2,3-Naphthalenedicarboxylic acid m/z - Expected m/z=922/Experimental m/z= of **8a** - 923.5[M+H] UV/Vis: λ_{max} [nm](logε): 702(3.92), 675(3.87), 442(3.60), 344(3.85); **8b** - 923.2[M+H] UV/Vis: λ_{max} [nm](logε): 690(3.23), 668(3.09), 372(3.21), 335(3.33); **8c** - 922.8[M+] UV/Vis: λ_{max} [nm](logε): 694(3.40), 669(3.29), 439(3.25), 325(3.62); **8d** - 923.0[M+] UV/Vis: λ_{max} [nm](logε): 702(3.39), 668(3.26), 440(3.13), 335(3.58).

2.4 Equipment/Instrumentation

Ground state electronic absorption spectra were performed on a ThermoFisher Scientific Multiskan SkyHigh Microplate Spectrophotometer between 300 and 900nm.

Emission and excitation spectra were obtained on a FluoTime 300 'EasyTau' spectrometer.

Infra-red spectra were collected on a Perkin-Elmer Universal ATR Sampling accessory spectrum 100 FT-IR spectrometer using KBr disks and bands were assigned using literature[64].

Mass spectra data were collected on a Bruker AutoFLEX III Smart-beam MALDI-TOF mass spectrometer using various matrices and modes of operation depending on the sample.

Fluorescence lifetimes and Isometric lifetimes were measured with a FluoTime 300 'EasyTau' spectrometer (PicoQuant GmbH) using a time correlated single photon counting (TCSPC). The samples were excited at 670 nm with a diode laser (LDH-P-670, 20 MHz repetition rate, 44 ps pulse width, PicoQuant GmbH). The detector employed was a Peltier cooled Photomultiplier (PMA-C 192-M, PicoQuant GmbH).

All Z-scans done in this study were performed with a frequency-doubled Nd:YAG laser (Quanta-Ray, 1.5 J /10 ns FWHM pulse duration) as the excitation source. The laser was operated in a near Gaussian transverse mode at 532 nm (second harmonic), with a pulse repetition rate of 10 Hz and energy range of 8-12 µJ. The beam was spatially filtered to remove the higher order modes and tightly focused with a 15 cm focal length lens. No damage was found between sample runs.

2.5 Modeling

The Gaussian 09 software package running on an Intel/Linux cluster was used to perform all of the DFT calculations, except for RT-TD DFT. The DFT geometric optimisations and Time Dependant DFT calculations were run using B3LYP hybrid functional with the LAND2LZ basis set. The CAM-B3LYP functional was used to calculate hyperpolarisabilty values using Coupled Perturbation Hartree Fock where LAND2LZ was used as the basis set.

The NWChem6.8 Software package running on an Intel/Linux cluster was used to perform all RT-TD DFT calculations. The calculations were run using M06 hybrid functional with the cc-pvdz basis set.

The large size of the phthalocyanines analysed brought forward multiple challenges. While some of these have been negated by advancements in computational power, not all issues were overcome and, as a result, some concessions made to be made. Highly complex basis sets and accurate functionals could not be used to calculate the properties of the phthalocyanines. Also, a truncation of the molecule size was required due to steric hinderance inhibiting the completion of optimisation simulation. β-H_2Pc(tert-BPh)$_8$ could not be analsysed with RT-TDDFT due to molecule size.

Chapter 3: Spectroscopic and Nonlinear Optical Characterization

3. Results and Discussion

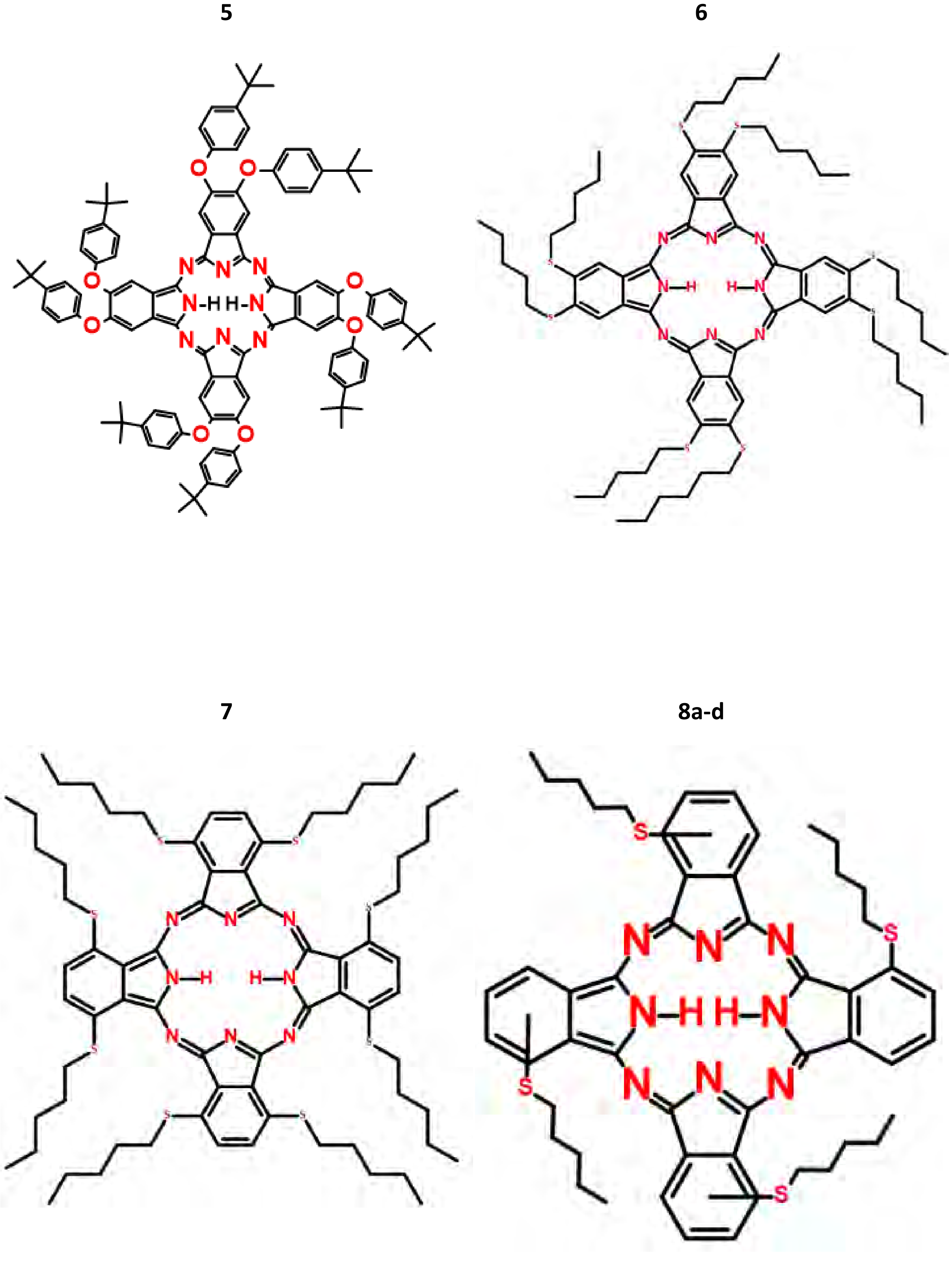

Figure 3.1: Summary of phthalocyanines synthesised in this work β-$H_2Pc(tert\text{-}BPh)_8$ (5), β-$H_2Pc(SC_5H_{11})_8$ (6), α-$H_2Pc(SC_5H_{11})_8$ (7), and α-$H_2Pc(SC_5H_{11})_4$ (8a-d).

3.1 Spectroscopic characterization of phthalonitriles

Scheme 3.1: Synthesis of 4,5-bis(4-tertbutyl-phenol)-phthalonitrile

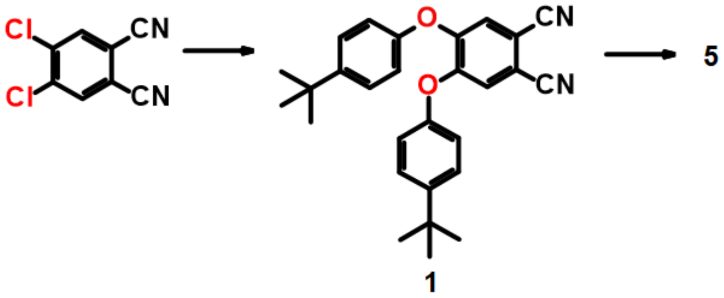

The conversion of 4,5-dichloro phthalonitrile to **1** is seen in **Scheme 3.1** above. The structure of **5** can be seen in **Figure 3.1**. In **Figure 3.2** below, the $\mathrm{C \equiv N}$ nitrile (2237 cm^{-1}) and $\mathrm{C-H}$ alkane (3014 cm^{-1}) stretches can be seen in addition to a $\mathrm{C-Cl}$ (683 cm^{-1}) stretch. This electron withdrawing chlorine group is a very good leaving group and this characteristic allows for simple nucleophilic action from the deprotonated 4-tert butyl phenoxy group, resulting in the synthesis of **4,5-bis(4-tertbutyl-phenol)-phthalonitrile (1).** The oxygen atom in **1** has an electron withdrawing effect resulting in the weaker appearance of the $\mathrm{C \equiv N}$ nitrile (2233 cm^{-1}) and more intense $\mathrm{C-H}$ alkane (2959 cm^{-1}) stretches in the spectra, including the shift in energy of these bands provides evidence of this synthesis. 4,5-Dichloro phthalonitrile also has a thin aromatic $\mathrm{C-H}$ stretch (1466 cm^{-1}) that widens due to the appearance of more varied aromatic $\mathrm{C-H}$ stretches in **1**. Furthermore, the disappearance of the $\mathrm{C-Cl}$ (683 cm^{-1}) stretch bands and appearance of the $\mathrm{C-O}$ aryl-aryl ether bonds (1201 cm^{-1} and 1011 cm^{-1}) gives more evidence to the completion of the reaction. MALDI-TOF MS confirmed the synthesis of **1** with a m/z of 424.3.

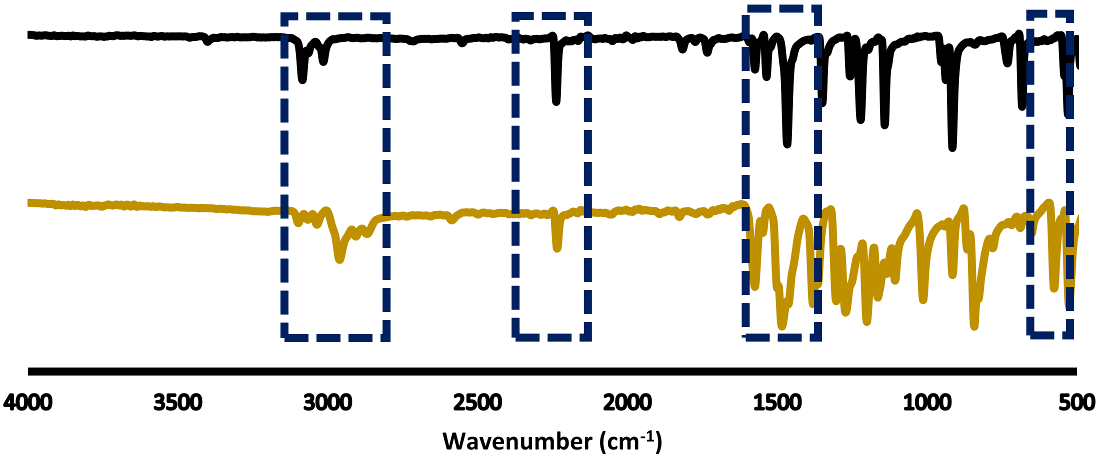

Figure 3.2: Infrared spectra of 4,5-bis(4-tertbutyl-phenol)-phthalonitrile (Black) and 4,5-dichloro phthalonitrile (1) (Orange)

Scheme 3.2: Synthesis of 4,5-bis(pentylsulfanyl)-phthalonitrile

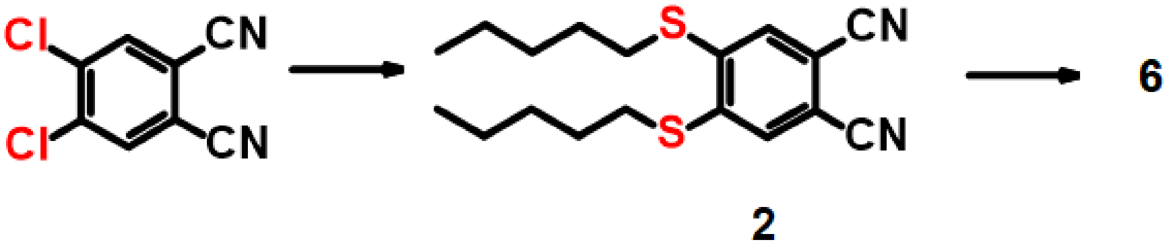

The conversion of 4,5-dichloro phthalonitrile to **2** is seen in **Scheme 3.2** above. The structure of **6** can be seen in **Figure 3.1.** In **Figure 3.3** below, the weak $\mathrm{C \equiv N}$ nitrile (2237 cm^{-1}) and $\mathrm{C-H}$ alkane (3014 cm^{-1}) stretches can be seen in addition to a $\mathrm{C-Cl}$ (683 cm^{-1}) stretch. This electron withdrawing chlorine group is a very good leaving group and this characteristic allows for simple nucleophilic action from the deprotonated pentane thiol group, resulting in the synthesis of **4,5-bis(pentylsulfanyl)-phthalonitrile (2).** The stronger absorption of the $\mathrm{C \equiv N}$ nitrile (2229 cm^{-1}) and $\mathrm{C-H}$ alkane (2928 cm^{-1}) stretches in the spectra, including the shift in energy of these bands provides evidence of this synthesis. Furthermore, the disappearance of the $\mathrm{C-Cl}$ (683 cm^{-1}) stretch bands and appearance of the $\mathrm{C-S}$ sulphide (730 cm^{-1}) gives more evidence to the completion of the reaction. MALDI-TOF MS confirmed the synthesis of **2** with a m/z of 330.0.

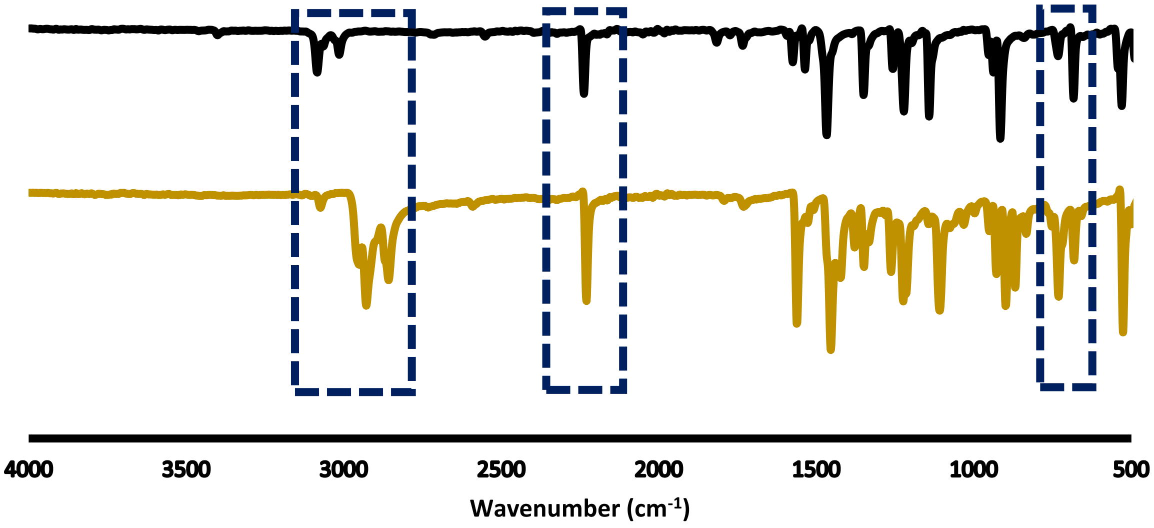

Figure 3.3: Infrared spectra of 4,5-bis(pentylsulfanyl)-phthalonitrile (Black) and 4,5-dichloro phthalonitrile (2) (Orange)

Scheme 3.3: Synthesis of 3,6-bis(pentylsulfanyl)-phthalonitrile.

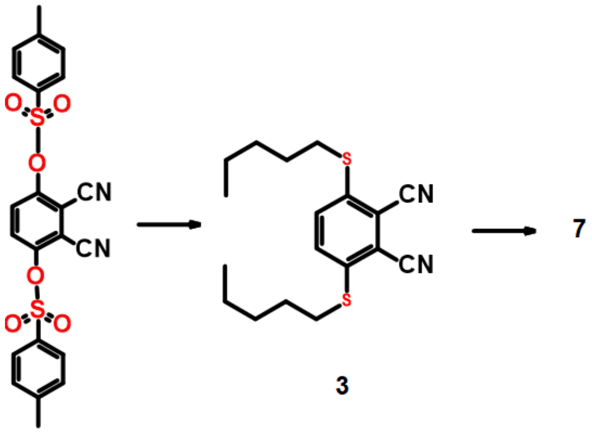

The conversion of 2,3-dicyano tosylhydroquinone to **3** is seen in **Scheme 3.3** above. The structure of **7** can be seen in **Figure 3.1.** In **Figure 3.4** below the electron withdrawing effects of the sulfonate group were seen in the weak $\mathrm{C \equiv N}$ nitrile (2242 cm^{-1}) and $\mathrm{C - H}$ alkane (2950 cm^{-1}) stretches. This 4-toluenesulfonyl group is a very good leaving group and this characteristic allows for simple nucleophilic action from the deprotonated pentane thiol group, resulting in the synthesis of **3,6-bis(pentylsulfanyl)-phthalonitrile(3)**. The stronger absorption of the $\mathrm{C \equiv N}$ nitrile (2220 cm^{-1}) and and $\mathrm{C - H}$ alkane (2947 cm^{-1}) stretches in the spectra, including the shift in energy of these bands provides evidence of this synthesis. Furthermore, the disappearance of the sulfonate bands (1380 cm^{-1} and 1175 cm^{-1}) and appearance of the $C-S$ sulphide (725 cm^{-1}) gives more evidence to the completion of the reaction. MALDI-TOF MS confirmed the synthesis of **3** with a m/z of 331.0.

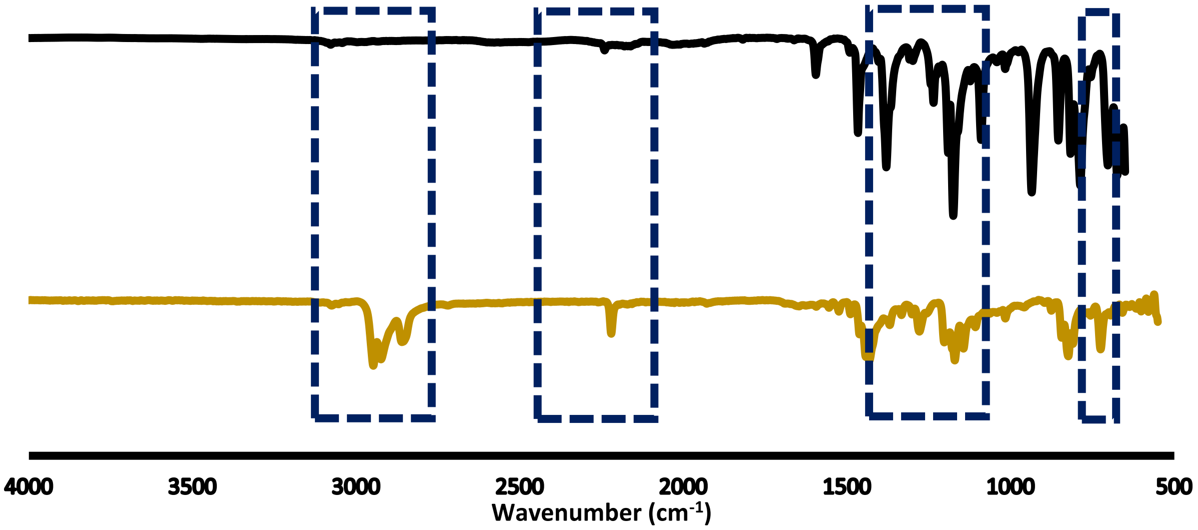

Figure 3.4: Infrared spectra of 3,6-bis(pentylsulfanyl)-phthalonitrile (Black) and 2,3-dicyano tosylhydroquinone (3) (Orange)

Scheme 3.4: Synthesis of 3-pentylsulfanyl-phthalonitrile

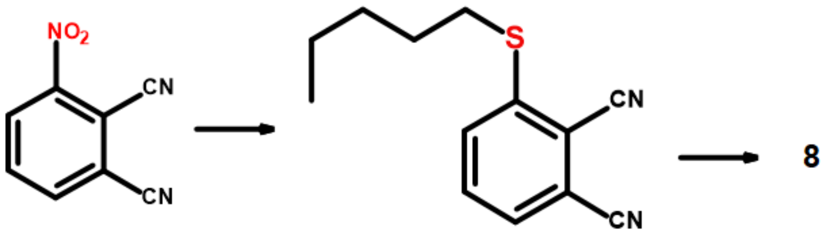

4

The conversion of 3-nitro phthalonitrile to **4** is seen in **Scheme 3.4** above. In **Figure 3.5** below, the electron withdrawing effects of the nitro group were seen in the weak $C \equiv N$ nitrile (2242 cm^{-1}) stretch. This nitro group is a very good leaving group and this characteristic allows for simple nucleophilic action from the deprotonated pentane thiol group, resulting in the synthesis of **3-pentylsulfanyl-phthalonitrile (4)**. The stronger appearance of the $C \equiv N$ nitrile (2225 cm^{-1}) stretch in the spectra, including the shift in energy of that band from 2236cm^{-1} to 2225cm^{-1} provides evidence of this synthesis. Furthermore, the disappearance of the nitro bands (1529 cm^{-1} and 1346 cm^{-1}) and appearance of the $C-S$ sulphide (689 cm^{-1}) gives more evidence to the completion of the reaction. MALDI-TOF MS confirmed the synthesis of **4** with a m/z of 229.1.

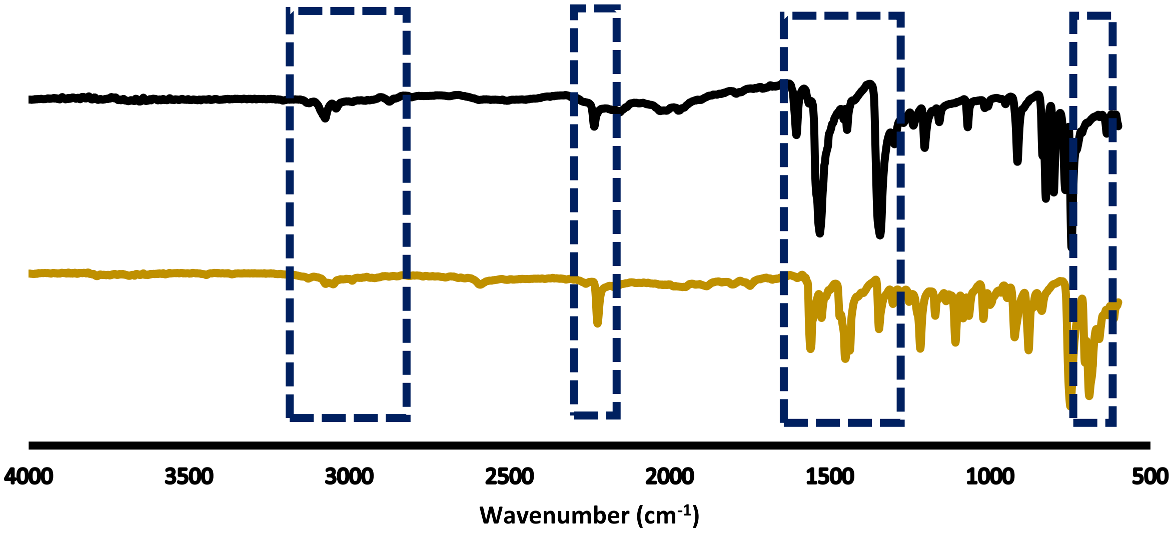

Figure 3.5: Infrared spectra of 3-pentylsulfanyl-phthalonitrile(Black) and 3-nitro phthalonitrile (4) (Orange)

3.2 Spectroscopic characterization of phthalocyanines

3.2.1 Synthesis confirmation

Scheme 3.5: Synthesis of β-H_2Pc(tert-BPh)$_8$

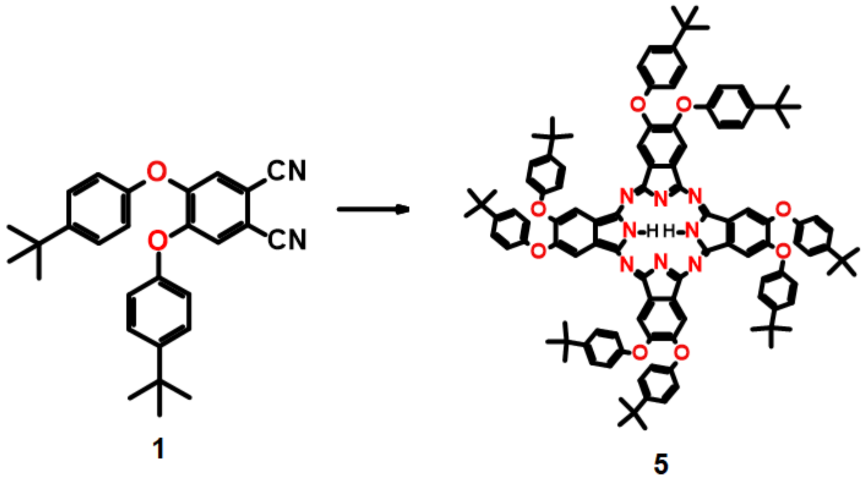

The conversion of **1** to **5** is seen in **Scheme 3.5** above. In **Figure 3.6** below, the $C \equiv N$ nitrile (2233 cm^{-1}) and $C-H$ (3034 cm^{-1}) stretches in the phthalonitrile **1** disappear and the IR spectrum of **5** is dominated by $C-H$ (2916 cm^{-1} and 2849 cm^{-1}) stretches that appear. This is proof of the completion of the reaction.

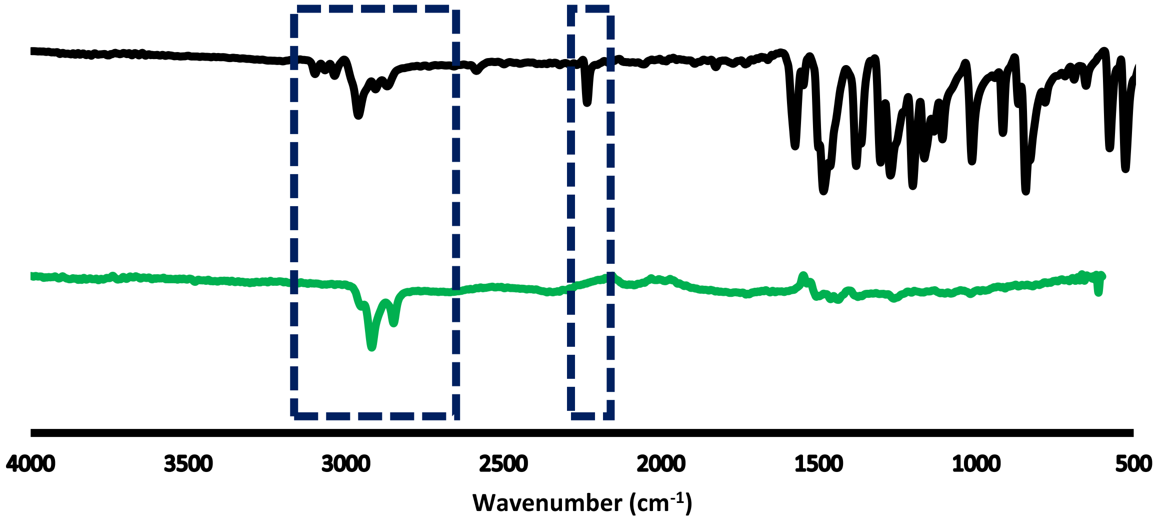

Figure 3.6: Infrared spectra of 4,5-bis(4-tertbutyl-phenol)-phthalonitrile (1) (Black) and β-H_2Pc(tert-BPh)$_8$ (5) (Green)

MALDI-TOF MS confirmed the synthesis of **1** with a m/z of 1702.5. TCSPC analysis in chloroform displayed a single lifetime of 6.09 ns and single emission of 710 nm. As seen in literature, TCSPC is a highly sensitive technique that can detect minor impurities in samples[65]. These impurities can be seen during the detection of emission, the measurement of fluorescent lifetimes or use of Time-Resolved Emission Spectra(TRES), where multiple chromophores capable of fluorescence in one sample can be detected.

Scheme 3.6: Synthesis of β-$H_2Pc(SC_5H_{11})_8$

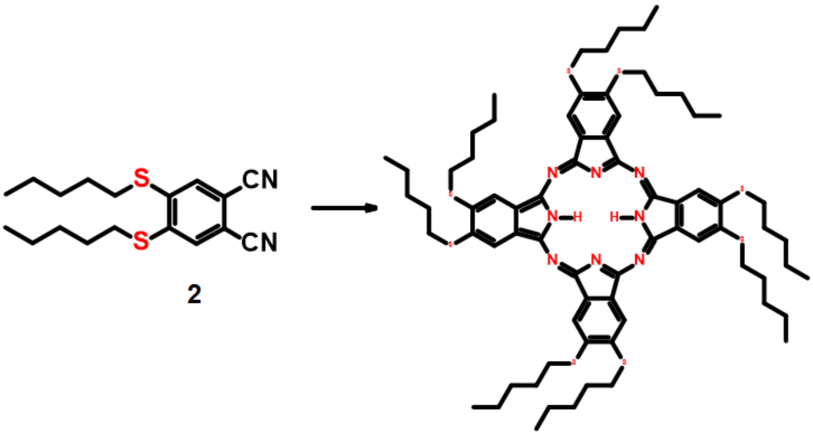

2

6

The conversion of **2** to **6** is seen in **Scheme 3.6** above. In **Figure 3.7** below, the $\mathrm{C \equiv N}$ nitrile (2229 cm^{-1}) and $\mathrm{C-H}$ (3073 cm^{-1}) stretches in the phthalonitrile **2** disappear and the IR spectrum of **6** displays the appearance of $\mathrm{N-H}$ (3283 cm^{-1}) and $\mathrm{C-H}$ (2913 cm^{-1} and 2844 cm^{-1}) stretches. This is proof of the completion of the reaction.

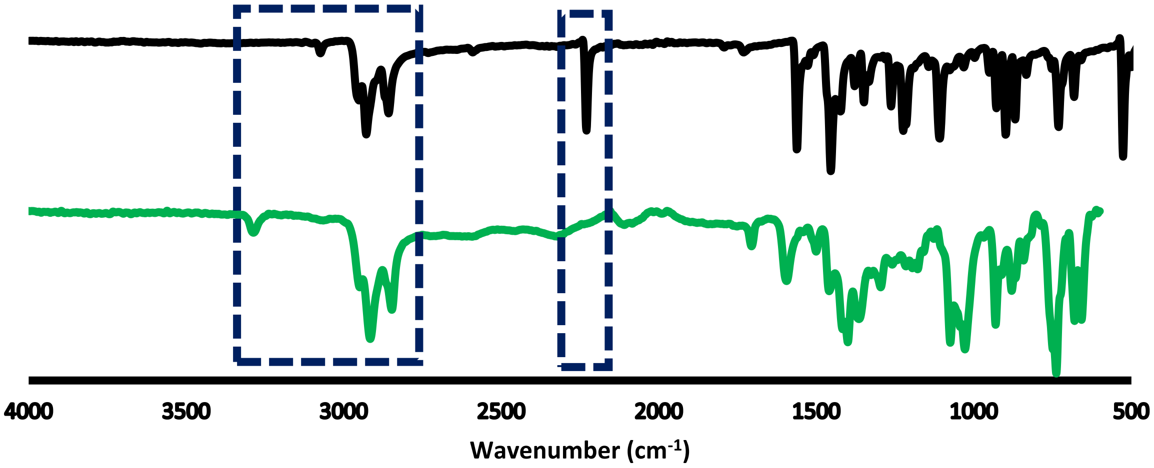

Figure 3.7: Infrared spectra of 4,5-bis(pentylsulfanyl)-phthalonitrile (2) (Black) and β-$H_2Pc(SC_5H_{11})_8$ Octa beta pentanethiol phthalocyanine (6) (Green)

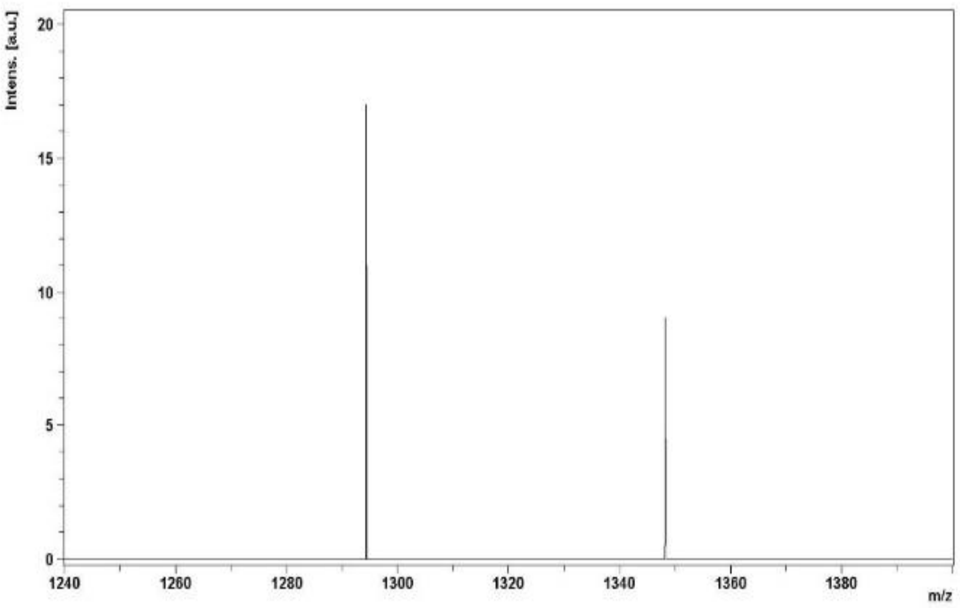

Figure 3.8: MALDI-TOF Mass Spectra of β-$H_2Pc(SC_5H_{11})_8$.

The β-$H_2Pc(SC_5H_{11})_8$ sample as analysed with 2,3-naphthalenedicarboxylic acid in DMF as the matrix, as seen in **Figure 3.8**. If fragmentation occurred, then the m/z value of 1348 could be the expected. Based on this hypothesis, mass of the sample (1330) = the mass of –OH (17) breaking off as a fragment of the matrix 2,3-naphthalenedicarboxylic acid and forming an adduct, would result in a value similar to the observed m/z value of 1348**.** The lability of the sulphur-carbon bond results in a possible cleavage between the substituent and the rest of the phthalocyanine. TCSPC analysis in chloroform displayed a single lifetime of 4.88 ns and single emission of 713 nm.

Scheme 3.7: Synthesis of α-$H_2Pc(SC_5H_{11})_8$

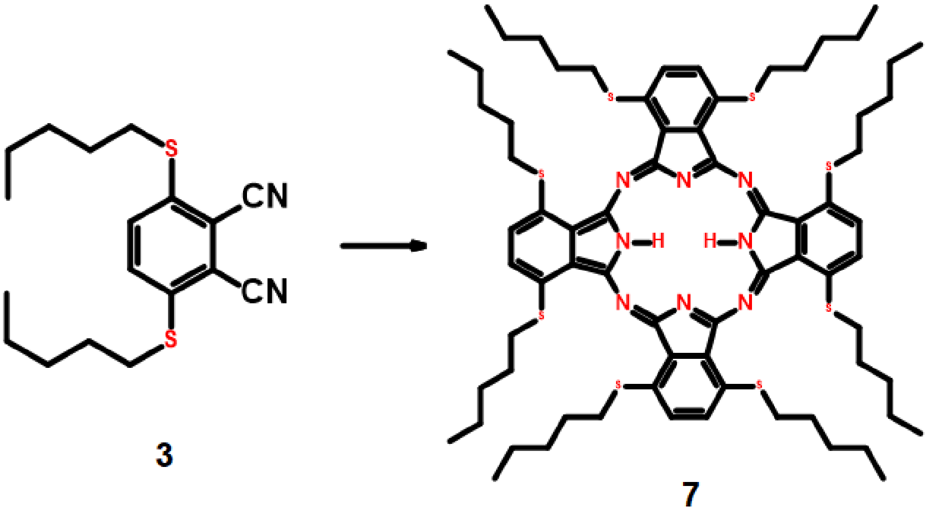

The conversion of **3** to **7** is seen in **Scheme 3.7** above. In **Figure 3.9** below, the $C \equiv N$ nitrile (2220 cm^{-1}) and $C-H$ (3073 cm^{-1}) stretches in the phthalonitrile **3** disappear and the IR spectrum of **7** contains $C-H$ (2915 cm^{-1} and 2846 cm^{-1}) stretches that appear. This is proof of the completion of the reaction.

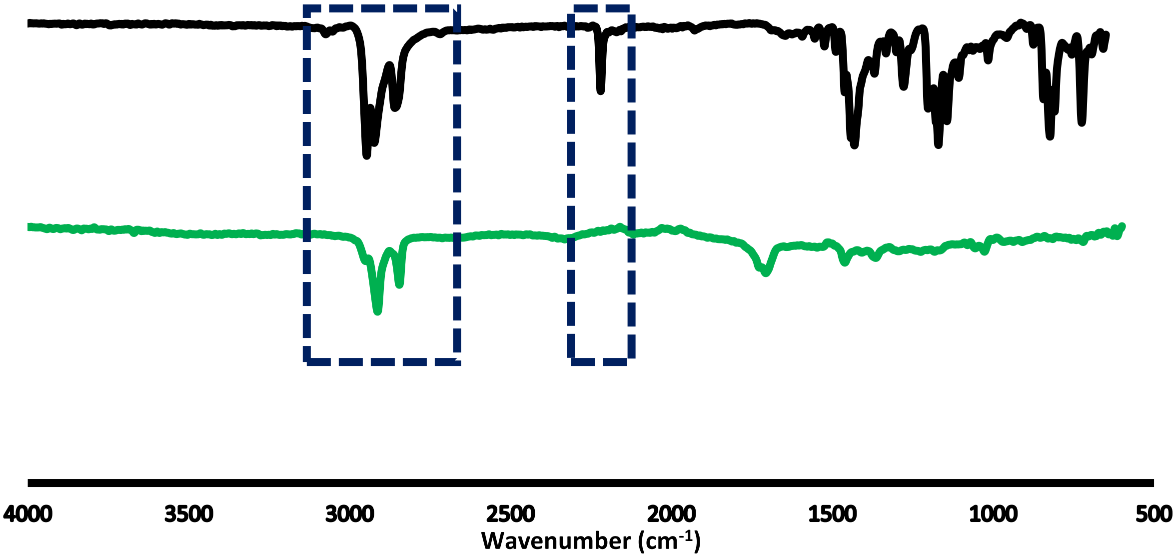

Figure 3.9: Infrared spectra of 3,6-bis(pentylsulfanyl)-phthalonitrile (3) (Black) and α-$H_2Pc(SC_5H_{11})_8$ (6) (Green)

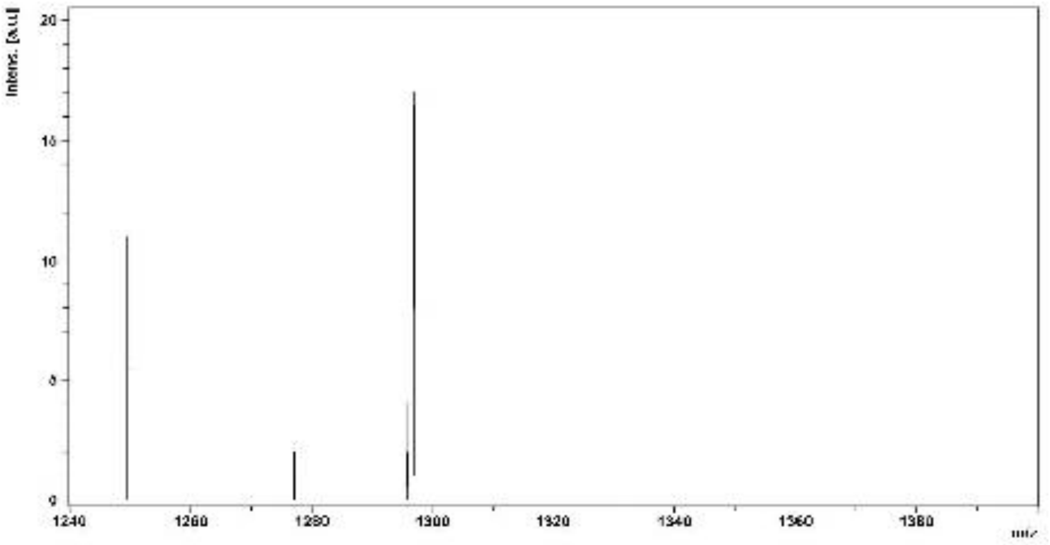

Figure 3.10: MALDI-TOF Mass Spectra of α-$H_2Pc(SC_5H_{11})_8$

The α-$H_2Pc(SC_5H_{11})_8$ sample was analysed with 2,3-Naphthalenedicarboxylic acid in DMF as the matrix, as seen in **Figure 3.10**. If fragmentation occurred, then the m/z value of 1296 could be the expected mass of the sample (1330) – the labile substituent(pentylsulfanyl) breaking off (103) + the mass of DMF (73), forming an adduct and resulting a value similar to the observed m/z value of 1296**. This same adduct can be seen in the Figure 3.8 above.** TCSPC analysis in chloroform displayed a single lifetime of 5.40ns and single emission of 710nm.

Scheme 3.8: Synthesis of α-$H_2Pc(SC_5H_{11})_4$ (C_s, C_{4h}, D_{2h} and C_{2v})

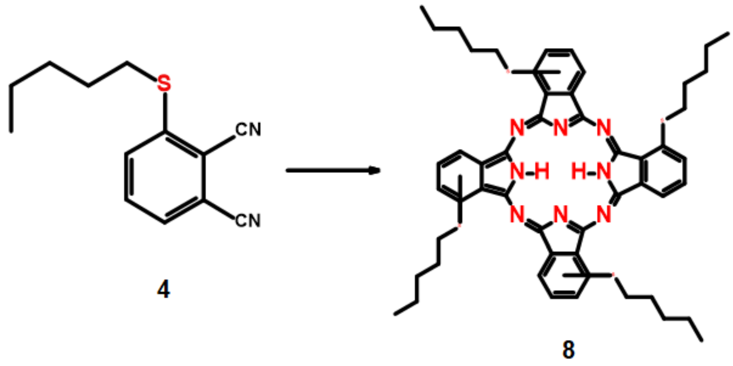

The conversion of **4** to **8** is seen in **Scheme 3.8** above. In **Figure 3.11** below, the $\mathrm{C \equiv N}$ nitrile (2225 cm^{-1}) and $\mathrm{C - H}$ (3049 cm^{-1}) stretches in the phthalonitrile **3** disappear and the IR spectrum of **7** contains $\mathrm{C - H}$ (2917 cm^{-1} and 2846 cm^{-1}) stretches that appear.This is proof of the completion of the reaction.

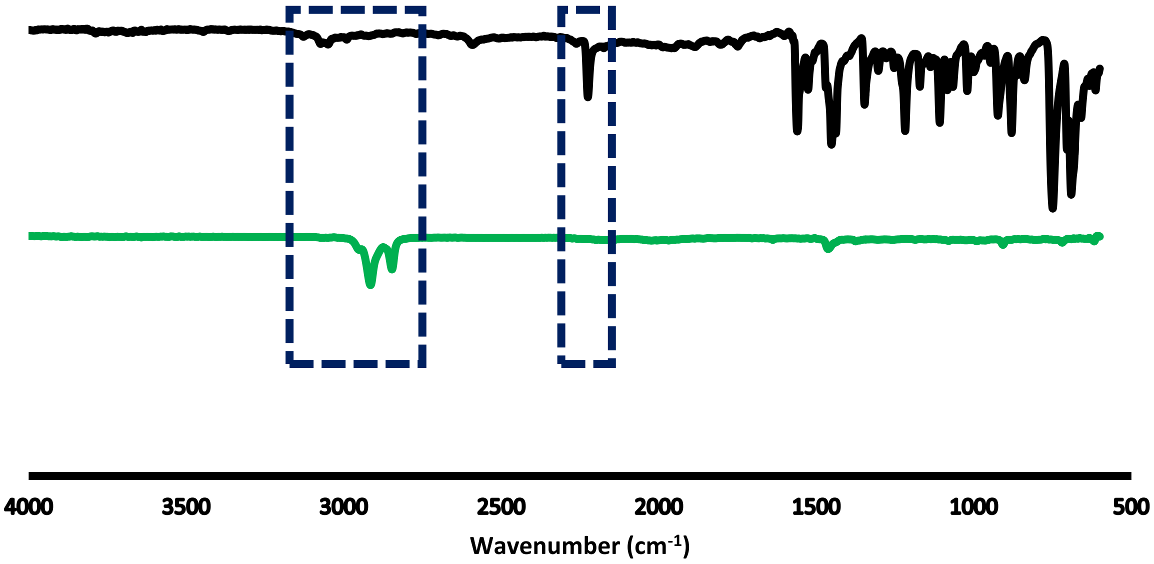

Figure 3.11: Infrared spectra of 3-pentylsulfanyl-phthalonitrile (4) (Black) and α-$H_2Pc(SC_5H_{11})_4$ (8) (Green)

MALDI-TOF MS confirmed the synthesis of **8a** with a m/z of 923.5, **8b** with a m/z of 923.2, **8c** with a m/z of 922.8 and **8d** with a m/z of 923.0. TCSPC analysis in chloroform displayed a single lifetime of 4.79ns and single emission of 714nm for **8a**, a single lifetime of 5.04ns and single emission of 705nm for **8b**, a single lifetime of 4.77ns and single emission of 711nm for **8c**, a single lifetime of 4.37ns and single emission of 714nm for **8d**. The structures for the constitutional isomers of **8** are indicated in **Table 3.1**.

Table 3.1: Constitutional Isomers of Compound 8

8a-C_s	**8b-C_{4h}**
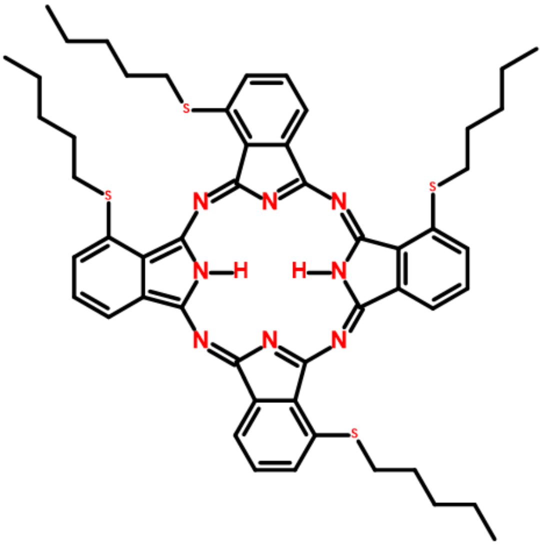	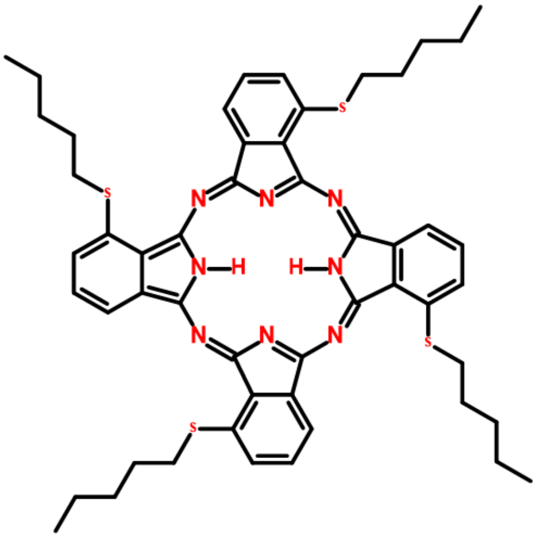
8c-D_{2h}	**8d-C_{2v}**
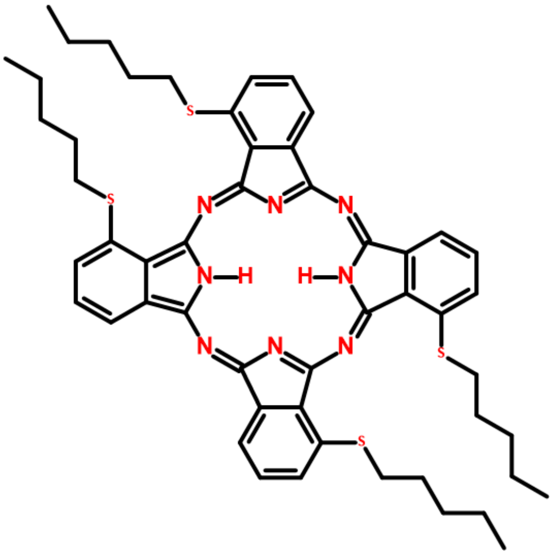	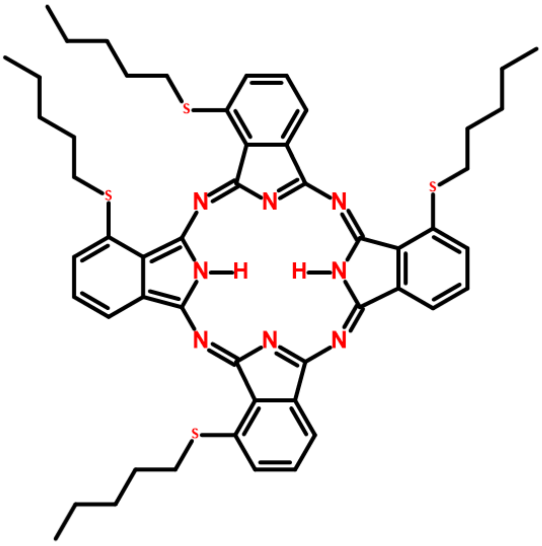

3.2.1 Assignment of Constitutional Isomer symmetries

The mixture of isomers that constitute α-$H_2Pc(SC_5H_{11})_4$ have been synthesized before as seen in literature[66], however in this instance the isomers where not separated and purified from each other and all analysis occurred on the mixture of isomers. In this work, the isomers where meticulously separated by use of column chromatography, instead of the expensive method of HPLC (High Performance Liquid Chromatography). There was inadequate resolution between the isomers, which required the use of chloroform:hexane solvent mixtures, where the percentage of hexane decreased with each layer that eluted out of the column. In many instances, a sample would be purified and would be analysed for its emission spectra, where multiple emissions could be detected, displaying the multiple fluorescing chromophores in the sample. This required some of these fractions to be purified 3-4 times to ensure that only one chromophore (a single isomer in this case), was giving fluorescence data such as emission and fluorescence lifetime data. This issue was not as prevalent with the fourth fraction, as minor amounts of methanol were required in the chloroform-based solvent mixture to elute the isomer out.

The symmetries of the Pc fractions were assigned by assessing the emission, absorption and excitation values and cross referencing them with literature[30] to give trends where, due to the difference in dipoles between different symmetries, varying emission, absorption and excitation values were expected for each of the symmetries. RT-TDDFT data was also used to determine the symmetries of the Pc fractions as seen in **Table 3.2** below. TDDFT data was used to determine the symmetries of the Pc fractions as seen in **Table 3.3** below. While computational methods display different results for absorbance compared to the experimental data (due to limitations such as the molecule being optimised and analysed in the gas phase *in silico*, the accuracy of the functional and basis set being used, truncation of molecule groups and other factors like solvation), trends in the computational results can give insight into experimental trends. In Both **Table 3.2** and **Table 3.3**, the trend in increasing experimental energy values for the Q-band maxima correlated with the trend of the increasing DFT-calculated energy values of the transitions responsible for the Q-bands in phthalocyanine electronic spectroscopy. This lead to the conclusion that Fraction 1 of **8** could be assigned with C_S symmetry, Fraction 2 of **8** could be assigned with C_{4h} symmetry, Fraction

3 of **8** could be assigned with D_{2h} symmetry and Fraction 4 of **8** could be assigned with C_{2v} symmetry. Geometrically optimised models of the Pcs are displayed in **Table 3.4**, with the necessary truncation of the alkyl groups clearly visible in the models of the sulphur substituted Pcs. The Pcs were not analysed using NMR spectroscopy because the Pcs were highly aggregated. MALDI-TOF-MS spectra of the Pcs can be found in the appendix section in **Table 6.2**.

Table 3.2: UV/Vis Q_{max} and RT-TDDFT results of sulphur substituted phthalocyanines ranging from longest to shortest wavelength.

Experimental (nm)	RT-TDDFT (nm)
α-$H_2Pc(SC_5H_{11})_8$ - 777	α-$H_2Pc(SC_5H_{11})_8$ - 757
β-$H_2Pc(SC_5H_{11})_8$ – 705	β-$H_2Pc(SC_5H_{11})_8$ – 705
Fraction 4 – 702	C_{2v} – 782
Fraction 1 - 702	C_S – 687
Fraction 3 – 694	D_{2h} – 684
Fraction 2 – 690	C_{4h} – 651

Table 3.3: UV/Vis Q_{max} and TDDFT results of sulphur substituted phthalocyanines ranging from longest to shortest wavelength.

Experimental (nm)	TDDFT (nm)
α-$H_2Pc(SC_5H_{11})_8$ - 777	α-$H_2Pc(SC_5H_{11})_8$ – 795
β-$H_2Pc(SC_5H_{11})_8$ – 705	β-$H_2Pc(SC_5H_{11})_8$ – 635
Fraction 4 – 702	C_{2v} – 676
Fraction 1 - 702	C_S – 671
Fraction 3 – 694	D_{2h} – 684
Fraction 2 – 690	C_{4h} – 684

Table 3.4: DFT geometrically optimised structures of phthalocyanines.

C_{2v} 	**C_{4h}** 
C_S 	**D_{2h}** 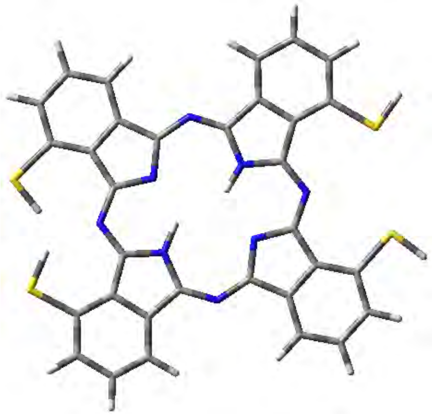
α-$H_2Pc(SC_5H_{11})_8$ 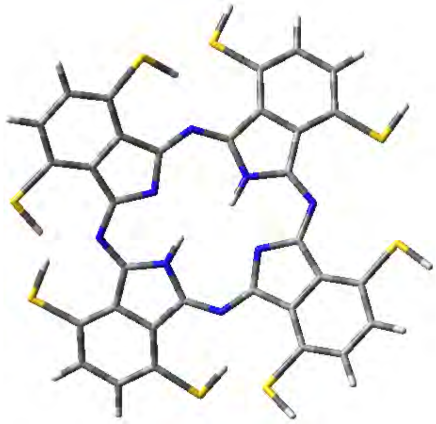	**β-$H_2Pc(SC_5H_{11})_8$** 

Table 3.4: DFT geometrically optimised structures of phthalocyanines. (continued)

β-H_2Pc(tert-BPh)$_8$

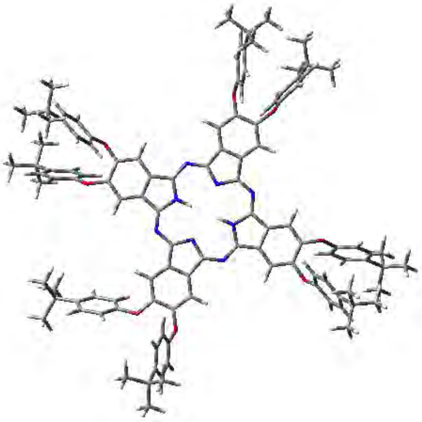

3.3 Electronic aborption and MCD spectroscopy

3.3.1 MCD and UV/Vis and TDDFT data of phthalocyanines.

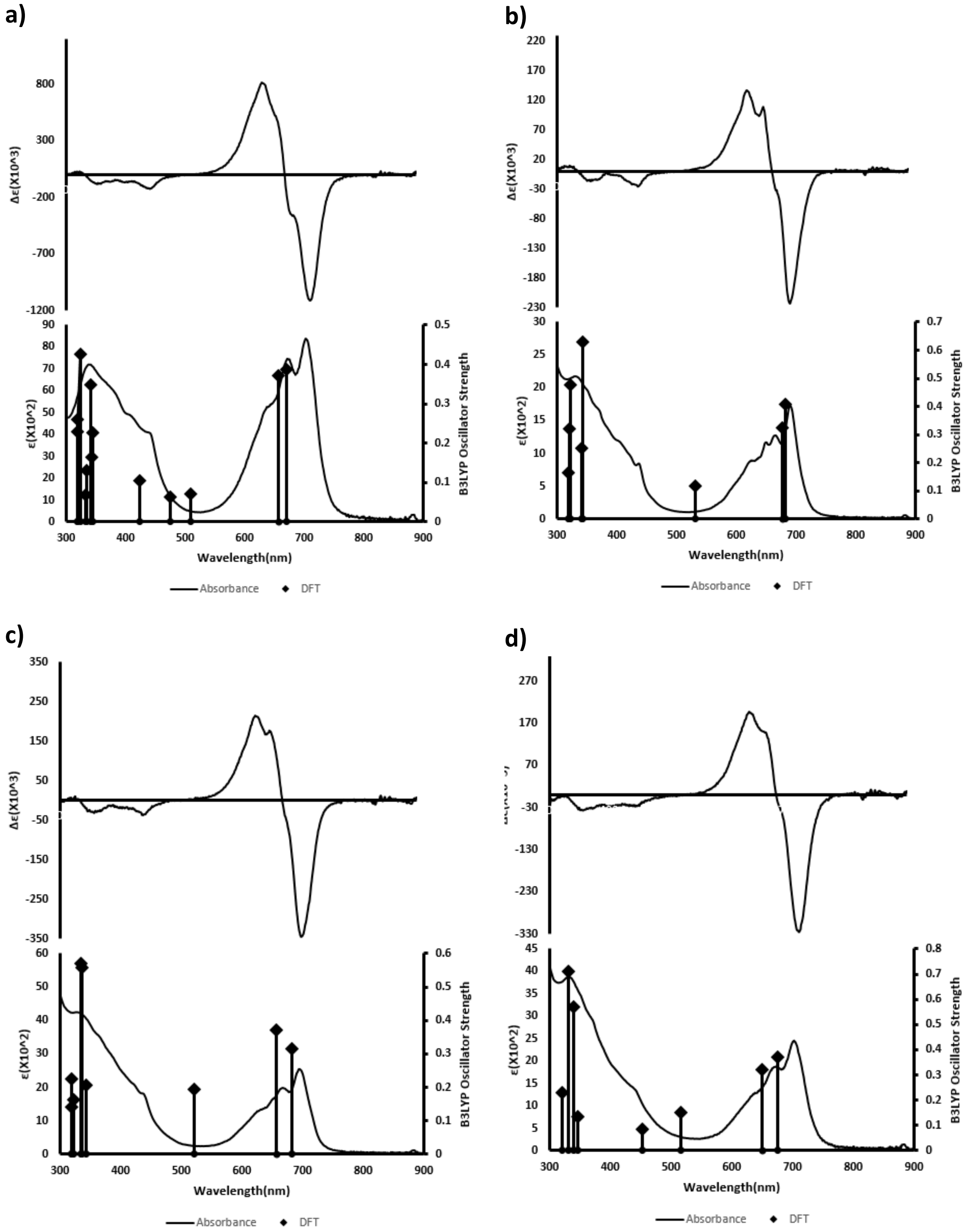

Figure 3.12: MCD, UV/Vis and TDDFT data of a-$H_2Pc(SC_5H_{11})_4$ phthalocyanine isomers of C_s (a), C_{4h} (b), D_{2h} (c) and C_{2v} (d) in chloroform.

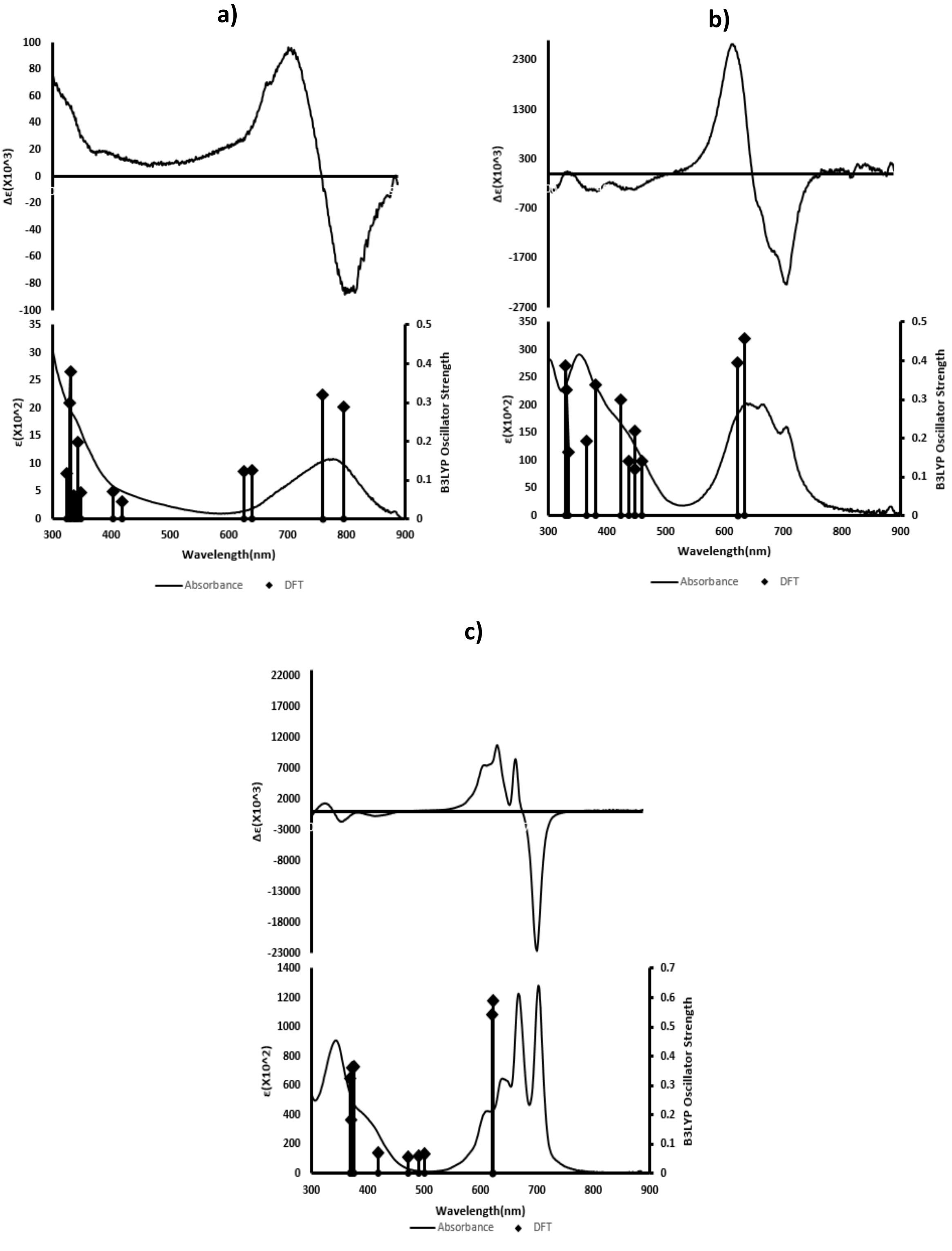

Figure 3.13: MCD, UV/Vis and TDDFT data of α-$H_2Pc(SC_5H_{11})_8$ (a), β-$H_2Pc(SC_5H_{11})_8$ (b) and β-H_2Pc(tert-BPh)$_8$ (c) in chloroform

All of the Pc's MCD spectra in **Figure 3.12** and **Figure 3.13** displayed Faraday B_0 terms (often observed in unmetalated Pcs), which was expected due to the mixing of closely related states that are linked by a magnetic dipole transition moment. The TDDFT data displayed adequate correlation with UV/Vis data and this correlation was seen in **Table 3.5.** The Q- and B-Band were seen with no transitions predicted to take place in between them. The 4 frontier orbitals that participate in these transitions can be seen in **Figure 3.14** below. The accuracy of the simulated absorbances can be improved by the addition of solvents, amongst other solutions. In **Figure 3.15** below, the differences in the HOMO and LUMO are indicated next to the arrows in black. α-$H_2Pc(SC_5H_{11})_8$ has a smaller band gap than β-$H_2Pc(SC_5H_{11})_8$ and this is seen in the redshifted Q-band of α-$H_2Pc(SC_5H_{11})_8$.

3.3.2 Time Dependant DFT Results

Table 3.5: TDDFT result of Phthalocyanines

C_s

Band[a]	#[b]	Calc[c]			Exp[d]		Wavefunction[e]
-	1	-	-	-	-	-	Ground State
Q	2	0.388	671	14.9	702	14.2	a→-a
Q	3	0.370	657	15.2	690	14.5	74% a→-s; 16% a→-a
B	25	0.228	345	29.0	442	22.6	31% s→-a; 47% H-12→-a
B	27	0.164	343	29.2	410	24.4	17% s→-s; 36% H-12→-a; 20% a→L+3(E_{gx})

C_{4h}

Band[a]	#[b]	Calc[c]			Exp[d]		Wavefunction[e]
-	1	-	-	-	-	-	Ground State
Q	2	0.409	684	14.6	690	14.5	80% a→-a; 20% a→-s
Q	3	0.326	677	14.8	669	14.9	86% a→-s
B	23	0.629	344	29.1	439	22.8	55% s→-a; 17% H-6(E_{gy})→-a
B	24	0.253	342	29.2	408	24.5	56% s→-s; 29% a→L+3(E_{gx})

D_{2h}

Band[a]	#[b]	Calc[c]			Exp[d]		Wavefunction[e]
-	1	-	-	-	-	-	Ground State
Q	2	0.315	683	14.6	694	14.4	a→-a
Q	3	0.372	657	15.2	675	14.8	a→-s
B	26	0.558	337	29.7	440	22.7	25% s→-a; 34% H-9→-s; 13% H-5(B_{1u})→-a
B	27	0.569	335	29.9	389	25.7	43% s→-s; 42% H-9→-a; 18% H-5(B_{1u})→-s

C_{2v}

Band[a]	#[b]	Calc[c]			Exp[d]		Wavefunction[e]
-	1	-	-	-	-	-	Ground State
Q	2	0.371	676	14.8	702	14.2	a→-a
Q	3	0.323	650	15.4	673	14.9	86% a→-s
B	25	0.571	340	29.4	439	22.8	34% s→-a; 35% a→-s; 31% a→-s
B	27	0.710	332	30.1	321	31.2	40% s→-a; 26% H-9→-a

α-$H_2Pc(SC_5H_{11})_8$

Band[a]	#[b]	Calc[c]			Exp[d]		Wavefunction[e]
-	1	-	-	-	-	-	Ground State
Q	2	0.289	795	12.6	777	12.9	a→-a
Q	3	0.125	640	15.6			a→-s
		0.320	759	13.2			83% H-1→-a; 17% a→-s
		0.122	624	16.0			84% H-1→-s; 16% a→-a
B	33	0.197	344	29.1	394	25.4	30% s→-a; 26% H-9(B_{1u})→-a; 22% H-16→-s; 22% a→-L+5
B	37	0.379	331	30.2	340	29.4	39% s→-s; 50% H-9(B_{1u})→L+2(B_{2u})

β-$H_2Pc(SC_5H_{11})_8$

Band[a]	**#**[b]	**Calc**[c]			**Exp**[d]		**Wavefunction**[e]
	1						Ground State
Q	2	0.456	635	15.7	705	14.2	85% a→-a; 15% H-3(A_{1u})→-s
Q	3	0.394	622	16.1	665	15.0	83% a→-s; 17% H-9(A_{1u})→-a
B	7	0.141	459	21.8	432	23.1	78% s→-a; 22% H-3(B_{1u})→-s;
B	9	0.218	447	22.4	358	27.9	s→-s

β-H_2Pc(tert-BPh)$_8$

Band[a]	**#**[b]	**Calc**[c]			**Exp**[d]		**Wavefunction**[e]
-	1	-	-	-	-	-	Ground State
Q	2	0.588	623	16.1	702	14.2	a→-a
Q	3	0.542	621	16.1	669	14.9	54% a→-s; 46% a→-a
B	34	0.364	374	26.7	410	24.4	60% s→-a; 16% H-18(B_{1u})→-a;
B	40	0.326	368	27.2	344	29.1	53% s→-s; 23% H-24(B_{1u})→-s

a - Band assignment described in the text. b - The number of the state assigned in terms of ascending energy within the TDDFT calculation. c - Calculated band energies (10^3 cm^{-1}), wavelengths (nm) and oscillator strengths in parentheses (f). d - Observed energies (10^3 cm^{-1}) and wavelengths (nm) from UV/Vis Experimental Data. e - The wave functions based on the eigenvectors predicted by TDDFT. One-electron transitions associated with Michl's perimeter model are highlighted in bold[67]. H and L refer to the HOMO and LUMO, respectively.

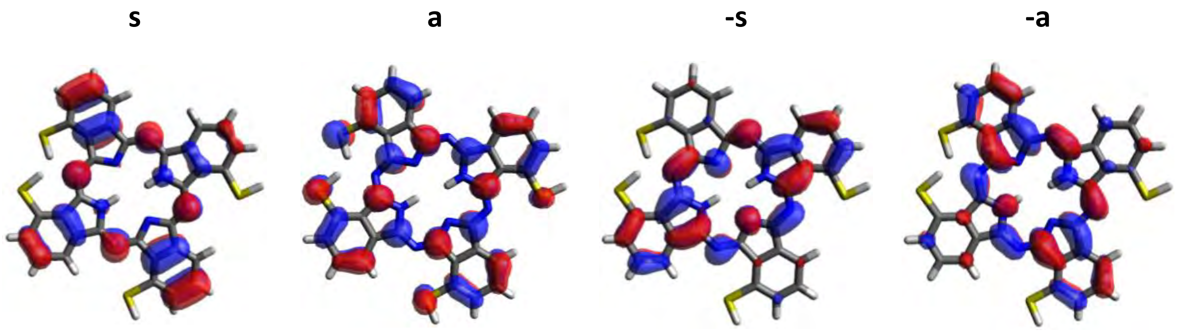

Figure 3.14: Michl's frontier orbitals of C_s

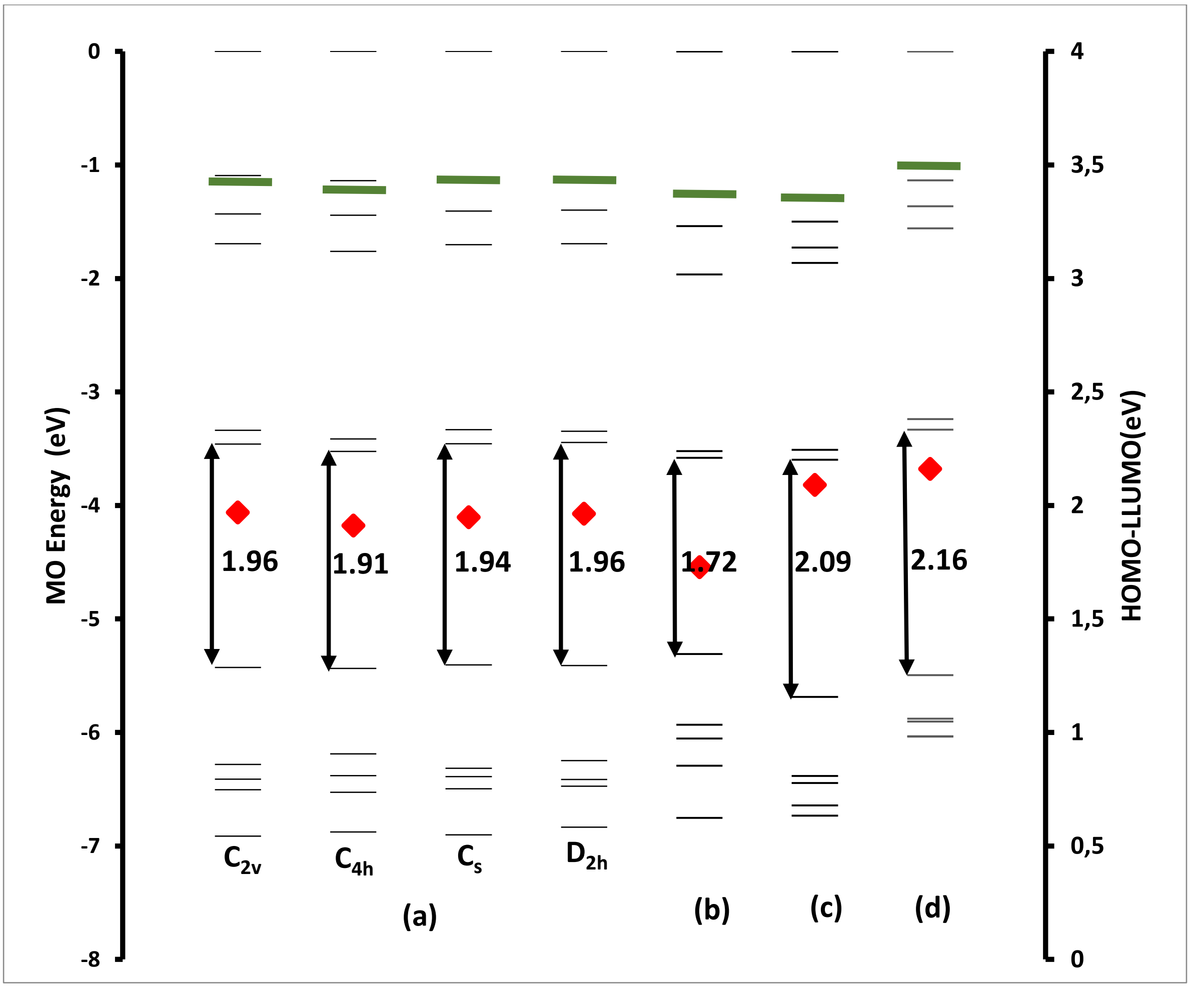

Figure 3.15: The MO energies (black line-primary axis), HOMO-LUMO band gaps (red diamond-secondary axis) and virtual states (green line-primary axis) of α-$H_2Pc(SC_5H_{11})_4$ isomers (C_{2v}, C_{4h}, C_s and D_{2h}) (a), α-$H_2Pc(SC_5H_{11})_8$ (b), β-$H_2Pc(SC_5H_{11})_8$ (c) and β-H_2Pc(tert-BPh)$_8$ (d).

3.3.3 RT-TDDFT

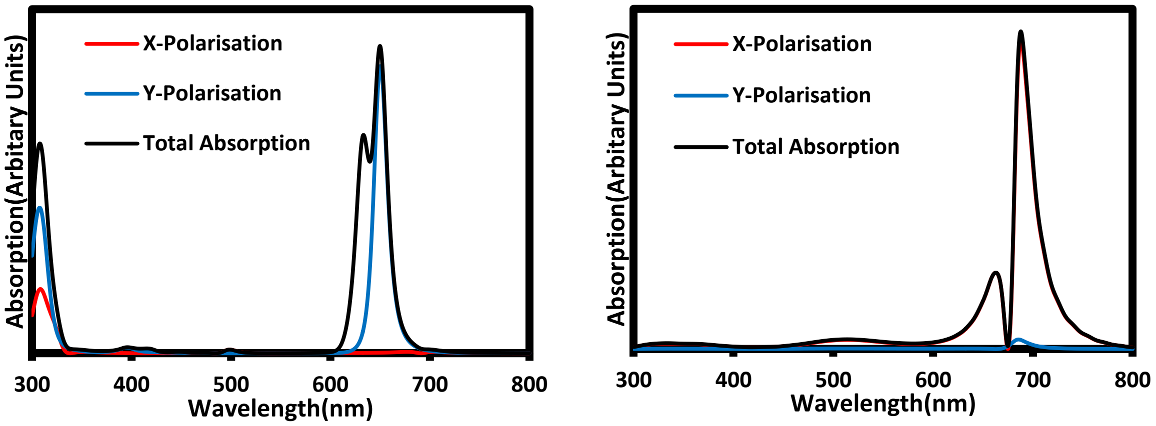

Figure 3.16: RT-TDDFT ground state and excited state graph of C_{4h}

While most of the data acquired relates to absorptions taking place from the ground state, once a molecule is in the excited state, there are other absorptions that can take place. To bring further understanding of the effect of light to a molecule in the excited state, RT-TDDFT studies were performed. Upon inspection of the ground state and excited state RT-TDDFT data in **Figure 3.16**, it can be seen that the x or the y-polarisation contributes a minimal amount to the total polarisation of the Q-band transition. This is because the majority of the polarisation observed corresponds with the lowest lying energy state, and this changes from x to y based on the molecule. As seen in **Figure 3.17**, the excited state absorption tends to occur at a lower energy than the ground state absorption. A resonance from an excited state caused the absorption in the 520nm region. The vibration in the ground state data is as a result of contamination from an excited state. Due to the mechanism of the RT-TDDFT simulation, it is possible that the observed vibrations can be attributed to higher or lower lying states that contaminate the current perturbation of the self consistent field, as seen in **Figure 3.17** below.The RT-TDDFT data for the other Pcs can be seen in the appendix section in **Table 6.1**.

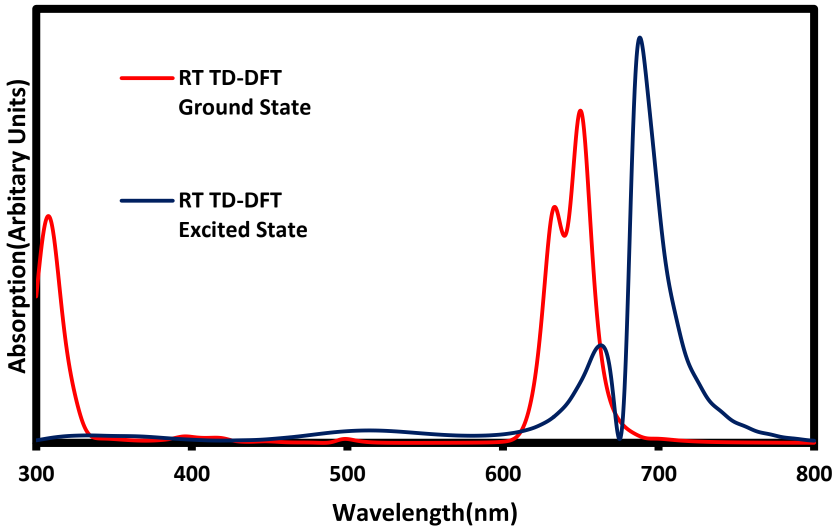

Figure 3.17: RT-TDDFT ground and excited state graph of C_{4h}

3.4 Absorbance, Fluorescence and Excitation

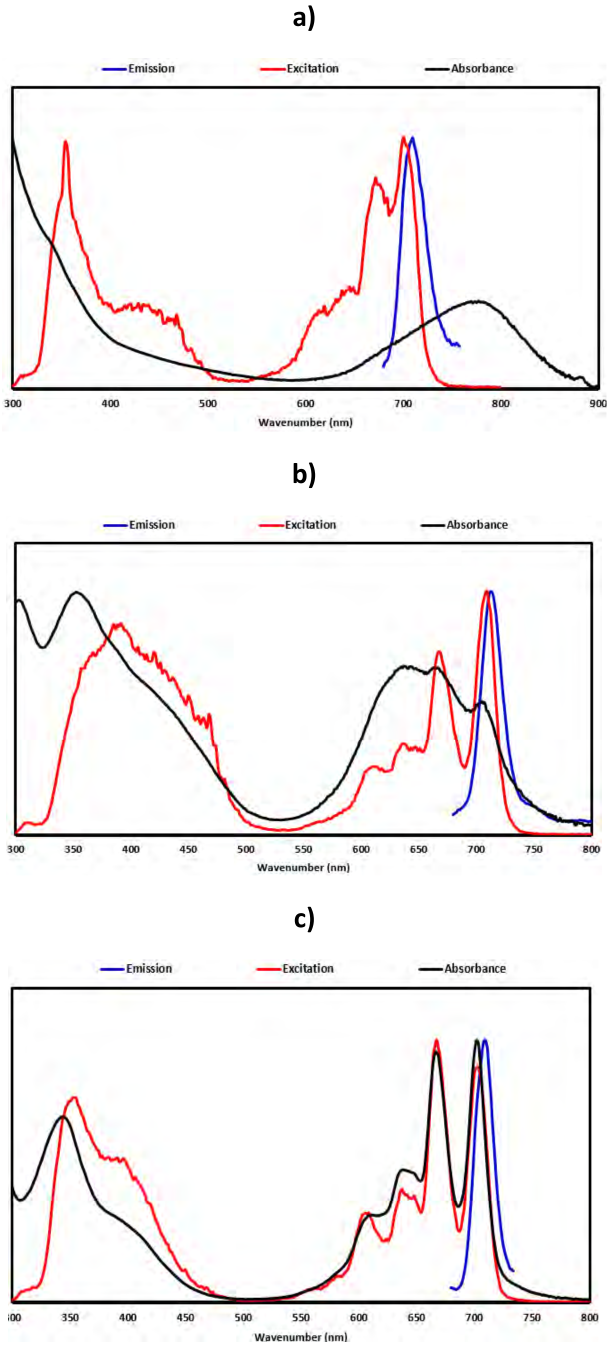

Figure 3.18: Normalised Emission, Excitation and Absorbance spectra of α-$H_2Pc(SC_5H_{11})_8$ (a), β-$H_2Pc(SC_5H_{11})_8$ (b) and β-H_2Pc(tert-BPh)$_8$ (c) in chloroform.

Upon inspection of **Table 3.6**, it can be seen that the Q-Band of α-$H_2Pc(SC_5H_{11})_8$ was red-shifted by at least 75 nm when compared to the rest of the Pc's. Here the effect of substititution at the alpha position is seen. The sulphur group is electron withdrawing, thus augmenting the dipole existent within the aromatic ring of the Pc. α-$H_2Pc(SC_5H_{11})_8$ was redshifted to β-H$_2$Pc(SC$_5$H$_{11}$)$_8$ because the substituent in α-H$_2$Pc(SC$_5$H$_{11}$)$_8$ is closer to the central aromatic system, resulting in a smaller HOMO-LUMO band gap. The UV/Vis spectra of α-H$_2$Pc(SC$_5$H$_{11}$)$_8$ displayed aggregation as seen in **Figure 3.18**. The wide band, not clearly displaying resolution between the Q-Band transitions, leads to the belief that the planar conformation of the central aromatic ring of the Pc did not warp despite the positioning of the alkyl sulphur substituent groups, as warping would have caused steric hinderance. The warping was seen upon inspection of geometrically optimised models of the Pcs. This warping typically takes place when substituents are bonded to the Pc aromatic ring through the alpha position[47, 68]. In **Figure 3.18**, this aggregation is not seen in the β-H$_2$Pc(tert-BPh)$_8$ due to the large 4-tert butyl phenoxy groups. In this case, the substituent is in the beta position instead of the alpha position, so while warping is not a factor, the large 4-tert butyl phenoxy groups cause enough steric hinderance to stop the formation of an aggregate.

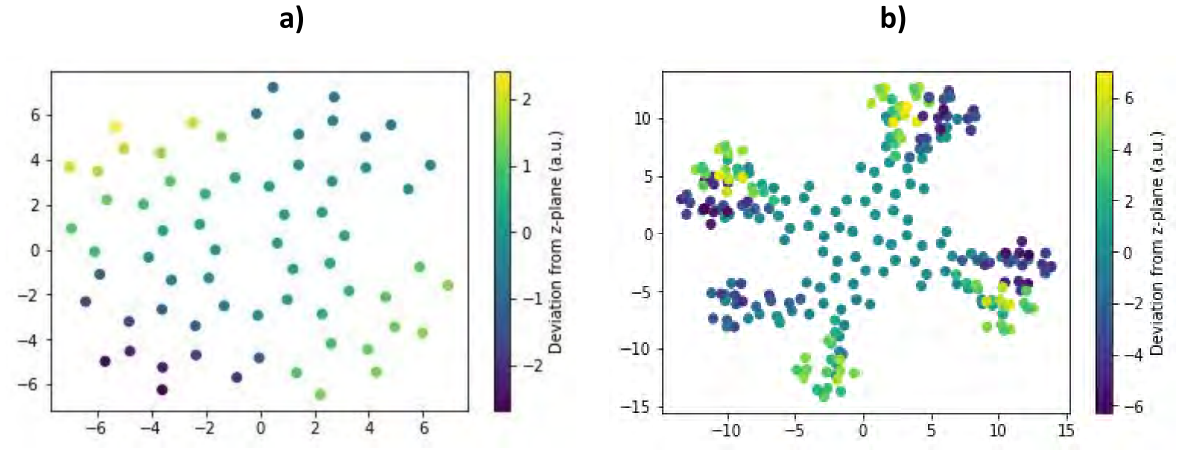

Figure 3.19: Central carbon position with respect to z plane of geometrically optimised phthalocyanine models of α-H$_2$Pc(SC$_5$H$_{11}$)$_8$ (a) and β-H$_2$Pc(tert-BPh)$_8$ (b).

In **Figure 3.19** above, the position of the central carbons in the z plane can be seen. The yellow and indigo colours of the 4 tertbutyl phenoxy substituent show a deviation from the z plane, show much to the extent that the previous mentioned steric hinderance takes place. The uniform turquoise colour in the central carbons in β-H$_2$Pc(tert-BPh)$_8$ clearly shows that the molecule has not undergone warping with respect to the z plane, while investigation of the central carbons of α-H$_2$Pc(SC$_5$H$_{11}$)$_8$ shows that the carbons have undergone warping with respect to the x, y and z plane. This warping however, was not sufficient to stop aggregates from forming, as seen in the absorbance data of α-$H_2Pc(SC_5H_{11})_8$. Graphs displaying the central carbon position with respect to the z-plane of all the Pcs can be found in **Table 6.3**.

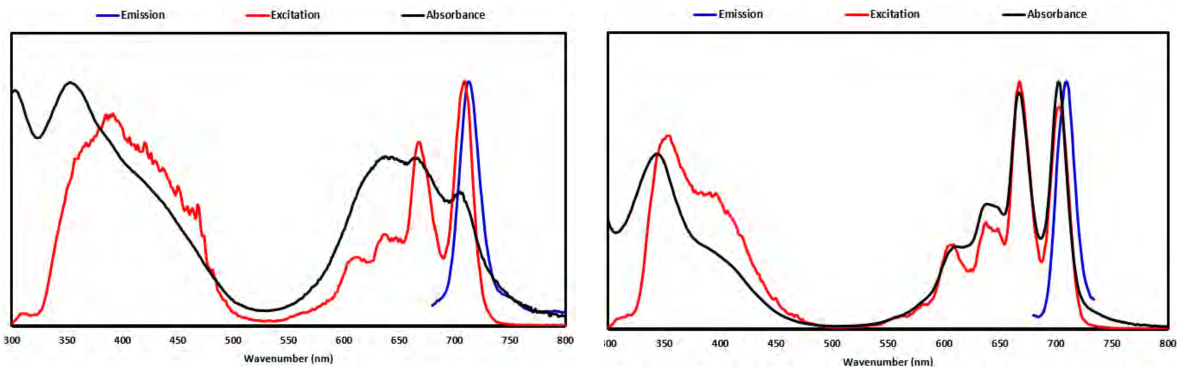

a) b)

Figure 3.20: Normalised Emission, Excitation and Absorbance spectra of β-$H_2Pc(SC_5H_{11})_8$ (a) and β-H_2Pc(tert-BPh)$_8$ (b) in chloroform

The UV/Vis spectra of β-H_2Pc(tert-BPh)$_8$ in **Figure 3.20** and **Table 3.5** showed that the oxygen groups of 4-tertbutyl phenol do not cause much shift in the Q-bands when compared to β-$H_2Pc(SC_5H_{11})_8$. Here the electron withdrawing characteristics of both β-$H_2Pc(SC_5H_{11})_8$ Pc's sulphur and β-H_2Pc(tert-BPh)$_8$ Pc's oxygen were observed. The Stokes shift of most of the Pc's displayed the same consistency in magnitude in chloroform.

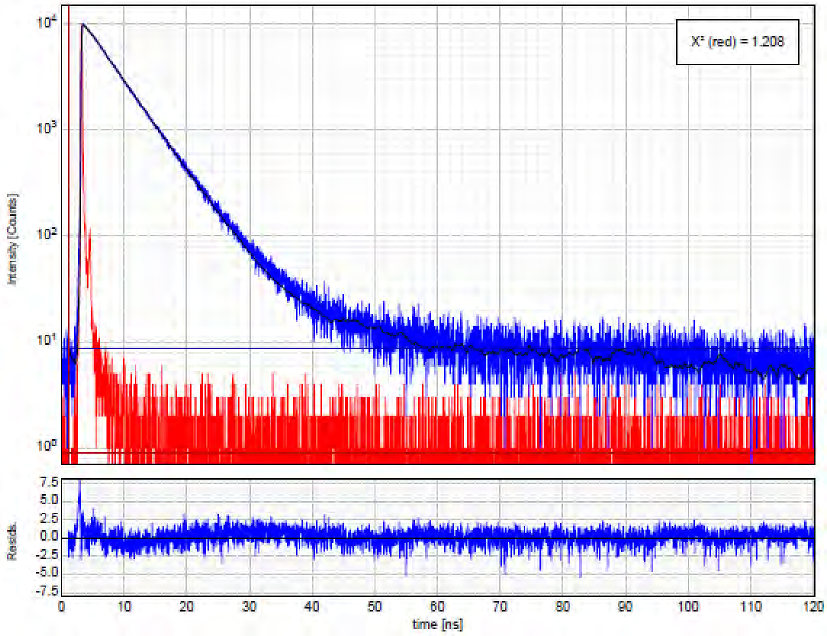

Figure 3.21: A time resolved mono-exponential fluorescence decay curve (obtained from TCSPC) for the β-$H_2Pc(SC_5H_{11})_8$ in chloroform.

The C_{4h} Pc also had the longest fluorescence lifetime of the all the isomers, followed by C_s, D_{2h} and then C_{2v}, where the lifetimes ranged between 4.3-5.0 ns. Amongst the Octa substituted Pcs, β-$H_2Pc(SC_5H_{11})_8$ (shown in **Figure 3.21** above) had the lowest fluorescent lifetime, followed by α-$H_2Pc(SC_5H_{11})_8$ and then β-H_2Pc(tert-BPh)$_8$, where the lifetimes ranged between 4.8-6.0 ns.

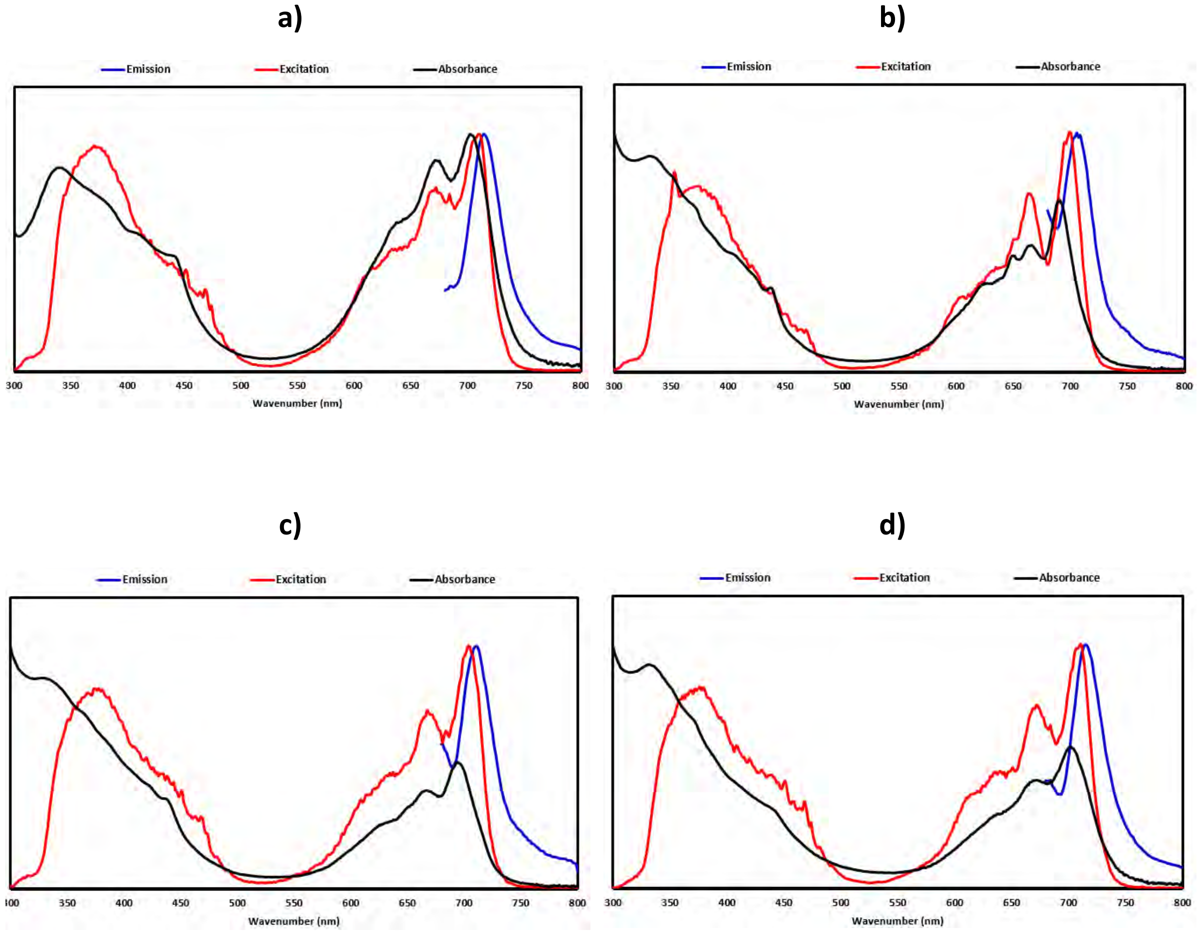

Figure 3.22: Normalised Emission, Excitation and Absorbance spectra of α-$H_2Pc(SC_5H_{11})_4$ isomers C_s (a), C_{4h} (b), D_{2h} (c), and C_{2v} (d) in chloroform.

Upon inspection of the UV/Vis spectra of C_{4h} in **Figure 3.22** above, the absorbance peaks of both Q-bands and both vibronic bands can be seen unlike the rest of the isomers. This can be attributed to aggregation.

Table 3.6: Q band maxima in the absorption (Abs), fluorescence emission(Em) and excitation (Exc) spectra, fluorescence lifetime (τ), anisotropy rotational correlation time (ϕ) values and molecular volumes (V_m) in chloroform.

	λ_{max} (nm)								
Pc	Abs	Em	Exc	Stokes Shift(nm)	τ(ns)		ϕ(ns)		$V_m/10^{-27}m^3$
C_s	702	714	709	12	4.7943	±0.0235	0.287	±0.0693	2.14
C_{4h}	690	705	699	15	5.0466	±0.0155	0.255	±0.0129	1.90
D_{2h}	694	711	703	17	4.7700	±0.0365	0.181	±0.0431	1.35
C_{2v}	702	714	711	12	4.375	±0.00806	0.502	±0.107	3.75
α-$H_2Pc(SC_5H_{11})_8$	777	710	700	67	5.4016	±0.01076	0.5029	±0.0853	3.76
β-$H_2Pc(SC_5H_{11})_8$	705	713	709	8	4.8817	±0.0275	0.513	±0.265	3.83
β-H_2Pc(tert-BPh)$_8$	702	710	700	8	6.0924	±0.0166	0.467	±0.0874	3.49

The rotational correlation times (**ϕ**) were used to calculate the molecular volume (V_m) occupied by each phthalocyanine using **Equation 40**:

$$V_m = \frac{\eta\phi}{kT} \quad \textbf{(40)}$$

where, η is the viscosity, k is the Boltzman constant and T the absolute temperature.

It was not expected to get lower V_m values for β-$H_2Pc(tert\text{-}BPh)_8$ (3.49 x 10^{-27} m^3) than when compared to β-$H_2Pc(SC_5H_{11})_8$ (3.83 x 10^{-27} m^3), considering that the substituents of β-$H_2Pc(tert\text{-}BPh)_8$ are larger than those of β-$H_2Pc(SC_5H_{11})_8$. The rotational correlation times can be alterted by molecular aggregation and solvent viscosity[57]. Considering that all the sulphur substituted Pcs experienced aggregation including β-$H_2Pc(SC_5H_{11})_8$, the rotational correlation time of β-$H_2Pc(SC_5H_{11})_8$ was probably altered by this aggregation, resulting in a larger V_m for β-$H_2Pc(SC_5H_{11})_8$ than compared to β-$H_2Pc(tert\text{-}BPh)_8$. Amongst the isomers, the isomer C_{2v} had the largest V_m value, followed by C_s, C_{4h} and then D_{2h}.

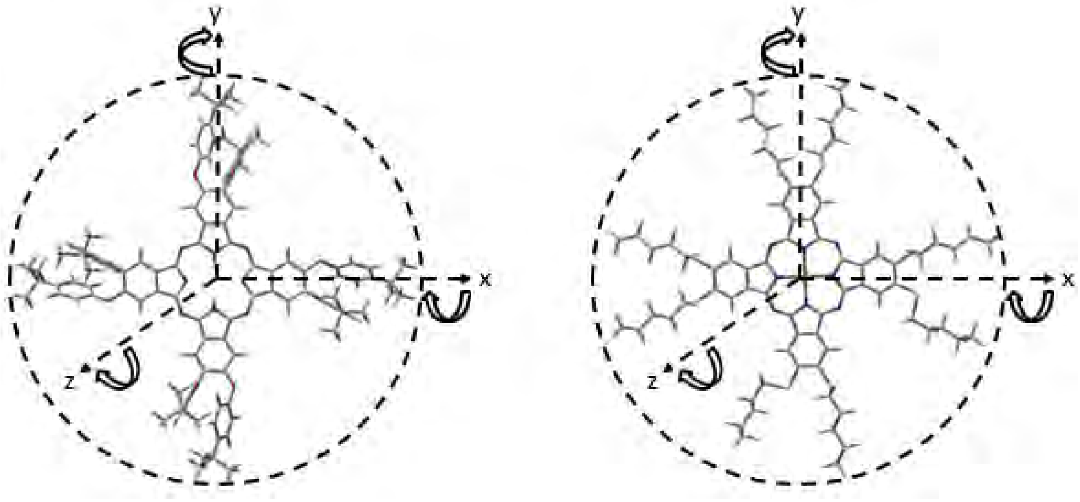

Figure 3.23: Theorectical Models of volume occupied by phthalocyanines in solution

3.5 Experimental and computational nonlinear optical properties

3.5.1 Z-scan properties of phthalocyanines

Closed Aperture Z-Scan analysis

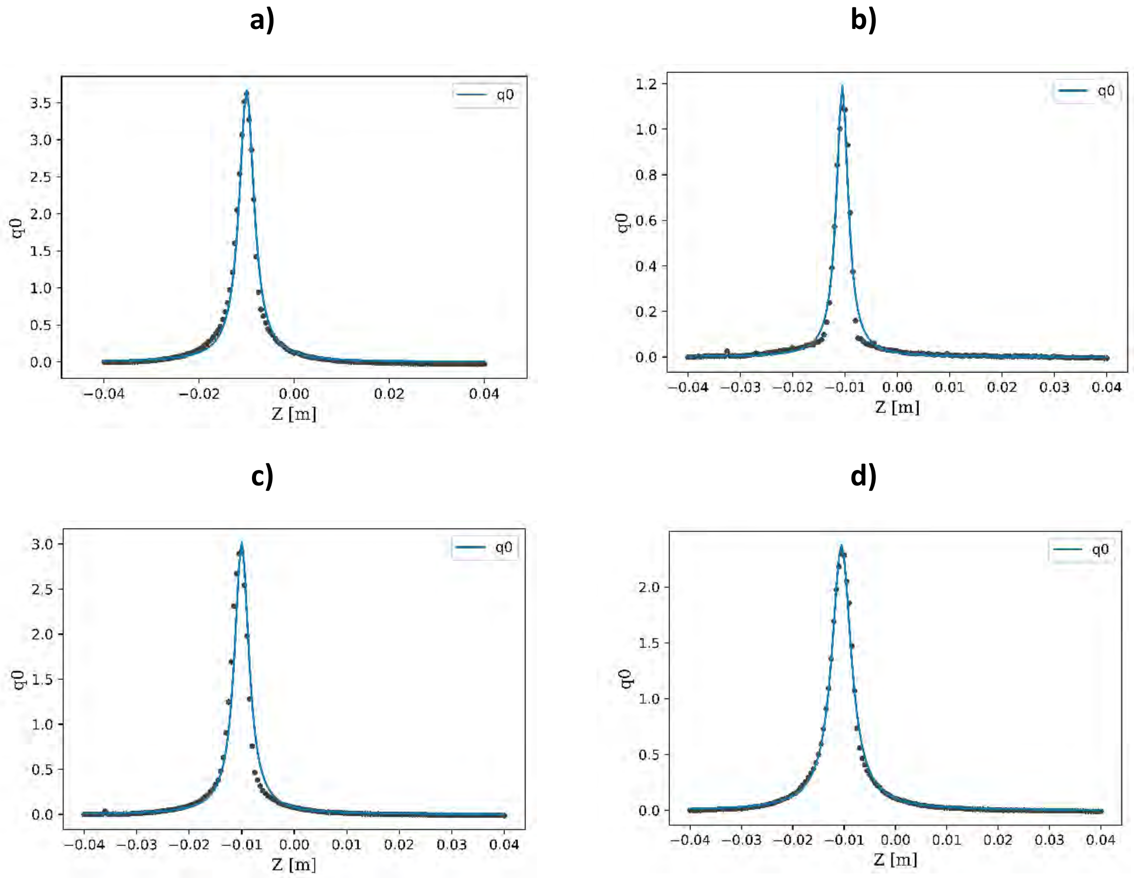
a)

b)

c)

d)

Figure 3.24: Open aperture nonlinear fit z-scan curve for C_s α-$H_2Pc(SC_5H_{11})_4$ isomer (a) at a focal intensity of 2.96 x 10^{12} $W.m^{-2}$, α-$H_2Pc(SC_5H_{11})_8$ (b) at a focal intensity of 4.06 x 10^{12} $W.m^{-2}$, β-$H_2Pc(SC_5H_{11})_8$ (c) at a focal intensity of 3.52 x 10^{12} $W.m^{-2}$ and β-H_2Pc(tert-BPh) (d) at a focal intensity of 2.22 x 10^{12} $W.m^{-2}$ in chloroform.

Figure 3.24 show the open aperture Z-scan nonlinear fit plots of $q_0(Z_s)$ for C_s α-$H_2Pc(SC_5H_{11})_4$ isomer (a), α-$H_2Pc(SC_5H_{11})_8$ (b), β-$H_2Pc(SC_5H_{11})_8$, (c) and β-$H_2Pc(\text{tert-BPh})_8$ (d), respectively. α-$H_2Pc(SC_5H_{11})_4$ C_s isomer $q_0(Z_s)$ plot serves as a representative of C_{2h}, D_{2h} and C_{2v} isomers, see appendix section **Figure 6.1** for their $q_0(Z_s)$ plots. All the compounds showed strong nonlinear absorption behaviour, with reverse saturable absorption (RSA) profiles, see **Figure 3.26**. The observed RSA response suggests that the excited state cross-section is greater than that of the ground state. The nonlinear fit of $q_0(Z_s)$ was used to obtain the nonlinear absorption coefficient (β) values using **Equation 19**[69]. The β parameter is used to quantify the strength of nonlinearity. **Table 3.7** below summarises the averaged β values obtained for all the compounds. The β values obtained in this work were found to be in range of reported values of α-$H_2Pc(SC_5H_{11})_4$ [51]. The β values of α-$H_2Pc(SC_5H_{11})_4$ isomers were found to follow the following trend C_S (6.42 ×10^{-10} MW^{-1}) > D_{2h} (5.89 ×10^{-10} MW^{-1}) > C_{2v} (5.51 ×10^{-10} MW^{-1}) > C_{4h} (3.31 × 10^{-10} MW^{-1}). Interestingly enough, these values were all lower than the β value of the mixture of α-$H_2Pc(SC_5H_{11})_4$ isomers. As seen in literature[66], β value of the mixture of α-$H_2Pc(SC_5H_{11})_4$ isomers was 14.7 ×10^{-10} MW^{-1} in THF. The β values of the octa substituted Pcs were found to follow the following trend β-H_2Pc(tert-BPh)$_8$ (5.80 ×10^{-10} MW^{-1}) > β-$H_2Pc(SC_5H_{11})_8$ (4.29 ×10^{-10} MW^{-1}) > α-$H_2Pc(SC_5H_{11})_8$ (1.23 ×10^{-10} MW^{-1}). The Im[γ] values followed the same trend as β values.

Table 3.7: Table containing experimental averaged Im[γ] of Phthalocyanines

	I **W.m^{-2}** **x 10^{12}**	**$Re[x^3]$** **esu** **x 10^{-15}**	**$Re[\gamma]$** **esu** **x 10^{-39}**	**zr** **m** **x 10^{-3}**	**β** **m.W^{-1}** **x 10^{-10}**	**$Im[x^3]$** **esu** **x 10^{-11}**	**$Im[\gamma]$** **esu** **x 10^{-32}**
C_S	1.98	-1.45	-5.79	2.94	6.42	2.29	59.20
C_{4h}	1.76	0.17	-1.43	3.88	3.31	1.18	1.21
D_{2h}	2.56	-0.53	-1.44	2.80	5.89	2.10	2.24
C_{2v}	3.51	-1.02	-4.39	2.26	5.51	1.96	1.04
α-$H_2Pc(SC_5H_{11})_8$	2.46	-1.26	-4.93	2.62	1.23	4.39	0.01
β-$H_2Pc(SC_5H_{11})_8$	1.69	0.62	2.45	3.63	4.29	1.53	4.67
β-H_2Pc(tert-BPh)$_8$	1.49	1.84	7.21	3.57	5.80	2.07	44.50

The β values were further used to calculate the imaginary third order susceptibility (Im[$\chi^{(3)}$]) using **Equation 1.20**[70]. The Im[$\chi^{(3)}$] values (in **Table 3.6**) were used to calculate second order hyperpolarizability (Im[γ]), which is concentration independent and directly related to the molecule, using **Equation 1.21** [70]**.** The following Im[γ] trend was obtained for α-$H_2Pc(SC_5H_{11})_4$ isomers, $5.93\ \times 10^{-31}$ (**C_s**) 2.24×10^{-32}(**D_{2h}**) > 1.21×10^{-32}(**C_{4h}**) > $1.05 \times$

10^{-32} (**C_{2v}**) esu, respectively. The optimal third order nonlinear hyperpolarizability values for phthalocyanines in solution have been reported to lie within 10^{-34}- 10^{-29}esu range[71]. The Im[γ]) values for D_{2h}, C_{2v} and C_{4h} are found to be lower in magnitude compared to 4α-(4-tert-butylphenoxy)phthalocyanine isomers values, which are in the rage of 10^{-31}esu, see **Table 1.3** [51]. However, C_s isomer showed a higher Im[γ] value within the trend and values obtained for 4α-(4-tert-butylphenoxy)phthalocyanine isomers. Except for α-$H_2Pc(SC_5H_{11})_4$ C_s isomer, the lower Im[γ] values for α-$H_2Pc(SC_5H_{11})_4$ isomers suggest that alkyl thio substituents at the α position do not improve the nonlinear optical properties of the Pc as compared to 4α-(4-tert-butylphenoxy) phthalocyanine isomers. The trend is also found to be different to the reported γ values for the monomeric isomers of 4α-(4-tert-butylphenoxy)phthalocyanine isomers, which were found to follow the following trend 2.32×10^{-31}(**C_{4h}**) > 2.11×10^{-31}(**D_{2h}**) > 1.11×10^{-31} (**C_{2v}**) > 0.68×10^{-31}(**Cs**) esu, respectively. The differences between the two trends are the C_s and C_{4h} isomers which swap positions. α-$H_2Pc(SC_5H_{11})_8$, β-$H_2Pc(SC_5H_{11})_8$, and β-H_2Pc(tert-BPh) compounds showed Im[γ] values of 1.00×10^{-32}, 4.6×10^{-32} and 4.45×10^{-31} esu, respectively. The Im[γ] values for α-$H_2Pc(SC_5H_{11})_8$, β-$H_2Pc(SC_5H_{11})_8$ are in the same range as α-$H_2Pc(SC_5H_{11})_4$ isomers. α-$H_2Pc(SC_5H_{11})_8$ showed the lowest Im[γ] value compared to β-$H_2Pc(SC_5H_{11})_8$, and β-H_2Pc(tert-BPh), respectively, once again suggesting that substitution of the α position with alkyl thio substituents does not improve the nonlinear optical properties of Pcs. When the alkyl thio substituent is replaced with tertbutylphenoxy substituent at the β position, 10-fold improvement in Im[γ] value was obtained. Sulphur is known to be more electron donating than oxygen. When substituted at the alpha position it has a greater destabilization effect compared to the beta position due to the presence of high molecular coefficient at the alpha position. Hence, the electron density of the Pc is affected more by the sulphur atom when substituted at the alpha position. Comparison of the Im[γ] values of β-$H_2Pc(SC_5H_{11})_8$ and β-H_2Pc(tert-BPh) compounds suggests that the 10 fold increase in the magnitude of the β-H_2Pc(tert-BPh) is due largely to the presence of the bulky tetrabutyl phenoxy substituent more than the oxygen or sulphur donating ability, since the beta position has a very low molecular coefficient. In summation, the results seemed to suggest that substitution with 4-tert- butyl phenol provided better NLO capabilities than substitution with pentane thiol due to the presence of the large bulky groups. The oxygen in 4-tert butyl phenol is also more electronegative than the sulphur in pentane thiol, resulting in more distortion in the permanent dipole that exists in the molecule.

Substitution at the beta position seems to provide better NLO capabilities based on the evidence in **Table 3.6**. Octa substitution allows for easier purification and replication of production than tetra substituted Pcs.

Table 3.8: Parametric model results of tetra substituted phthalocyanine and octa substituted phthalocyanines.

	I W.m^{-2} x 10^{12}	**n^2 m^2.W^{-1} x 10^{-17}**	**Δn x 10^5**		**I W.m^{-2} x 10^{12}**	**n^2 m^2.W^{-1} x 10^{-17}**	**Δn x 10^5**
C_s	1.39	-3.14	-4.36	**α-$H_2Pc(SC_5H_{11})_8$**	1.9	-3.3	-6.26
	2.29	-2.05	-4.7		2.92	-2.18	-6.36
	2.96	-1.64	-4.84		4.06	1.72	7
	1.28	-3.51	-4.51		0.961	-5.23	-5.03
C_{4h}	1.25	-3.83	-4.78	**β-$H_2Pc(SC_5H_{11})_8$**	1.85	3.01	5.56
	2.18	-2.33	-5.08		3.52	1.78	6.28
	3.06	1.82	5.57		0.641	-5.89	-3.77
	0.575	5.58	3.21		0.762	5.49	4.18
D_{2h}	2.31	2.37	5.47	**β-H_2Pc(tert-BPh)$_8$**	1.23	3.57	4.38
	2.19	-2.42	-5.3		1.66	2.84	4.73
	2.5	-2.11	-5.26		2.22	2.18	4.85
	3.26	-1.63	-5.32		0.845	4.52	3.82
C_{2v}	1.7	-2.9	-4.94				
	3.2	-1.61	-5.17				
	3.84	-1.52	-5.86				
	5.28	-1.25	-6.58				

Upon inspection of both blue curve fits in **Figure 3.25**, a peak- valley signature can be seen at the lower focal intensity, while a valley-peak signature can be seen at the higher focal intensity. For the closed aperture fits for the other Pcs , see appendix **Table 6.4**. This peak-valley signature is indicative of a negative refractive index (n^2), while a valley-peak signature is indicative of a positive refractive index, and this can be seen in **Table 3.7**. As the focal intensity increases, the excited state population increases. When the power of the laser was increased, the excited states of the material (which exhibit an inverse sign of the nonlinear refraction response compared to the ground state nonlinear refraction response) were reflected in their increase in population, hence changing the curve morphology from peak-valley to valley-peak.

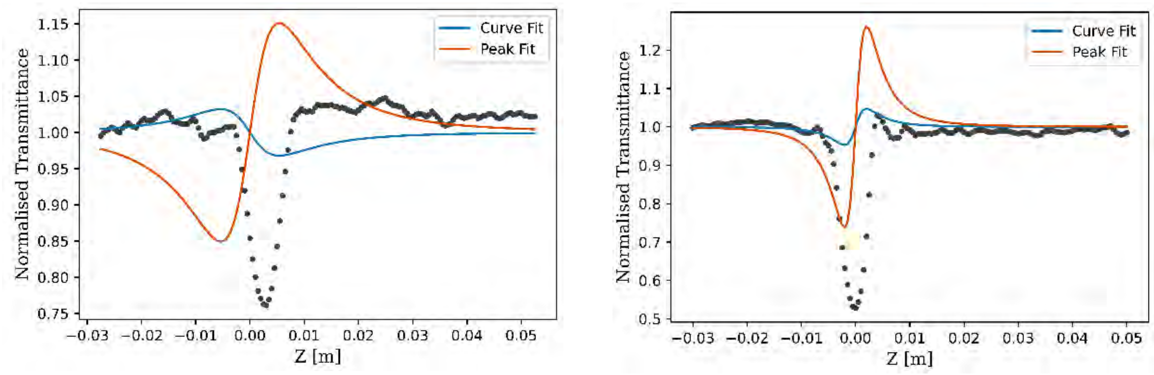
a)

b)

Figure 3.25: Closed aperture fit graph of C_{4h} at a focal intensity of 5.75 x 10^{11} W.m^{-2} (a) and 3.06 x 10^{12} W.m^{-2} (b).

3.5.2. Analysis of the ground state and excited state cross section

Experimental and theoretical z-scan transmittance plots based on the five-energy level model for C_s α-$H_2Pc(SC_5H_{11})_4$ isomers (**a**), α-$H_2Pc(SC_5H_{11})_8$ (**b**), β-$H_2Pc(SC_5H_{11})_8$, (**c**) and β-H_2Pc(tert-BPh)$_8$ (**d**) in chloroform are shown in **Figure 3.26** below. The ground state and excited state cross sections where calculated using the five-level model[72, 73]**.** The fit and the experimental data show a decrease in transmittance at the focal position (z = 0 cm), which shows a reverse saturable absorption (RSA) behaviour, which is also confirmed by a positive difference between the σ_E and the σ_g. RSA transmittance curve is observed when the excited state absorption cross section (σ_S) is greater than the ground state absorption cross section (σ_g). **Figure 3.26** also shows that the dominant contribution to RSA curve is the singlet excited state absorption (ESA). The excited state is populated *via* 2 photon absorption and very small linear absorption at 532 nm.

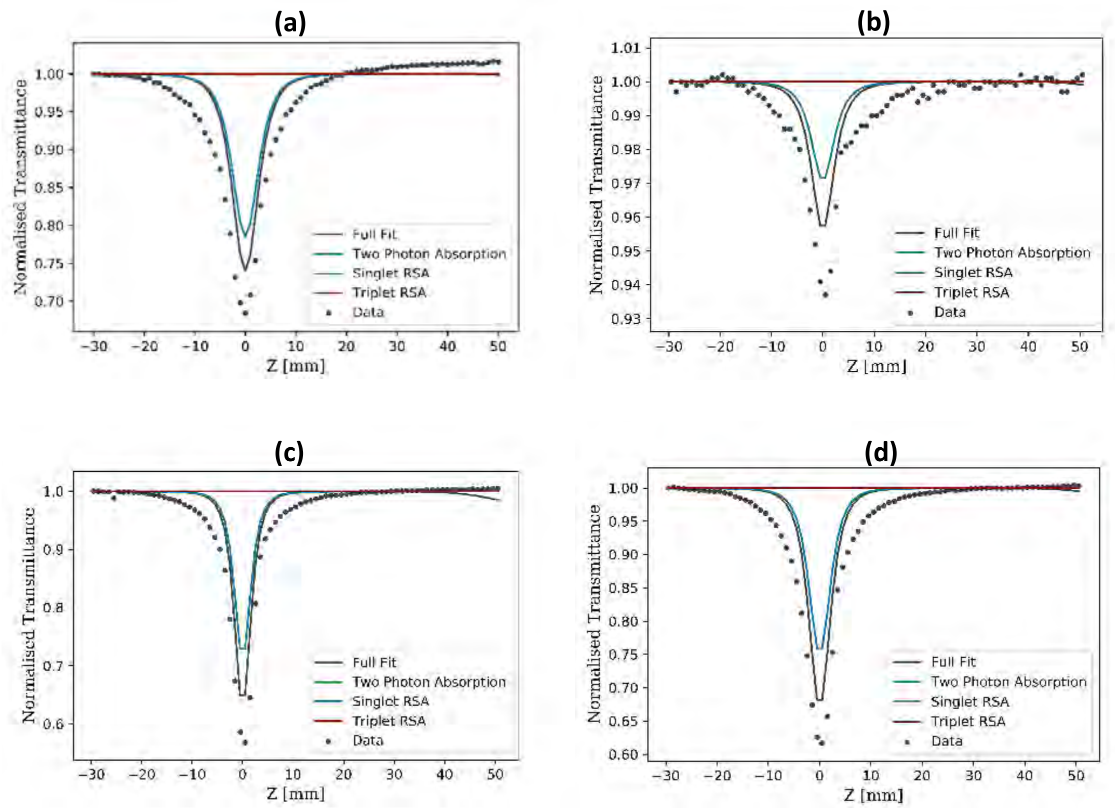

Figure 3.26: Experimental and theoretical z-scan transmittance plots based on the five-energy level model for C$_s$ α-$H_2Pc(SC_5H_{11})_4$ isomers (a), α-$H_2Pc(SC_5H_{11})_8$ (b), β-$H_2Pc(SC_5H_{11})_8$, (c) and β-H_2Pc(tert-BPh)$_8$ (d) in chloroform.

In **Figure 3.13**, while the TDDFT data does not display any absorbances in the region around 532nm for the octa substituted phthalocyanines, these absorbances are seen in the tetra substituted phthalocyanines. In the RT-TDDFT data, **Figure 3.17** gives an example where a small ground state absorption around the 500-532nm region is seen and an excited state absorption is seen in the same region.

Equation 41 below was used to calculate the ground state absorption cross section (σ_g).

$$\sigma_g = \frac{\alpha}{N_0} \tag{41}$$

Where α is the linear absorption and N_0 is the number of molecules per cm^3. The two-photon absorption cross section (σ_{2PA} [GM]) and singlet state absorption cross section (σ_S [**Å^2**]) were calculated by fitting the experimental data with the five-level model using the rate **Equations 23-28** , following literature method[72, 73]. As the phthalocyanines were unmetalated, an acceptable triplet signal could not attained, and as a result a standard value of ISC was used to fit the data using the non-parametric fit.

Table 3.9 below summarises the σ_{TPA} [GM], σ_s [Å^2], and σ_g [Å^2] cross sections values for α-$H_2Pc(SC_5H_{11})_4$ isomers, α-$H_2Pc(SC_5H_{11})_8$, β-$H_2Pc(SC_5H_{11})_8$, and β-H_2Pc(tert-BPh)$_8$. The σ_g cross section for the compounds studied in this work were found to be within a range of 0.009 - 0.080 (Å^2). In **Table 3.9** the ratio of the excited state cross section (σ_E [m^2] = σ_s [m^2] + σ_{TPA} [m^2]) and σ_g cross section for all the compounds are shown to be greater than 1 ($\sigma_E > \sigma_g$), suggesting a RSA behaviour for all the isomers. The σ_{TPA} of the α-$H_2Pc(SC_5H_{11})_4$ isomers (see **Table 3.9**) are found to follow the following trend C_{2v} (152.9) > D_{2h} (137.4) > C_s (68.5) > C_{4h} (2.4) GM. The octa substituted Pcs showed the following trend, β-$H_2Pc(SC_5H_{11})_8$ (959.8) > β-H_2Pc(tert-BPh)$_8$ (703.6) > α-$H_2Pc(SC_5H_{11})_8$ (124.4) GM. The observed trends for α-$H_2Pc(SC_5H_{11})_4$ isomers and octa substituted Pcs does not follow the Im[γ] value trend, suggesting that the σ_{TPA} is not the only parameter that should be used to characterise materials.

Table 3.9: Ground state absorption cross section (σ_g), first excited state absorption cross section (σ_s) and the two-photon absorption cross section (σ_{TPA}) of phthalocyanines, all at 532nm.

	σ_g [Å^2]	σ_s [Å^2]	σ_{TPA} [GM]
C_s	0.033	0.201	68.5
C_{4h}	0.015	0.443	2.4
D_{2h}	0.011	0.593	137.4
C_{2v}	0.014	0.421	152.9
α-$H_2Pc(SC_5H_{11})_8$	0.009	0.077	124.4
β-$H_2Pc(SC_5H_{11})_8$	0.080	0.489	959.8
β-H_2Pc(tert-BPh)$_8$	0.010	0.266	703.6

3.5.3. DFT calculations for first order hyperpolarizability.

DFT calculations were performed, using B3LYP level of theory and 6-311G basis set, in order to determine the theoretical second order nonlinear polarizability (β) values. Theoretical dipolar and octupolar ($\Phi_{J=1}$ and $\Phi_{J=3}$) contributions were also calculated.

Table 3.10 below shows the theoretical data of first order hyperpolarizability (β_{HRS}), Dipolar and Octupolar parameters. α-$H_2Pc(SC_5H_{11})_4$ isomers showed β_{HRS} trend C_s (7.87) > D_{2h} (7.41) > C_{4h} (5.83) > C_{2v} (4.89) esu. The theoretical β_{HRS} is found to be higher for the isomer with the lowest symmetry (C_s isomer). A contradiction to this trend was seen in literature[30] in 4-tertbutyl phenoxy substituted isomers where the following trend of C_{4h} (4.61) > D_{2h} (4.00) > C_{2v} (3.42) > C_s (2.49) was observed, clearly showing a lowest β_{HRS} for the molecule with the lowest symmetry. β_{HRS} values for octupolar Pcs where found to follow the following trend β-$H_2Pc(SC_5H_{11})_8$ > α-$H_2Pc(SC_5H_{11})_8$ > β-H_2Pc(tert-BPh)$_8$. β and β_{HRS} are not directly comparable because they represent different parameters and therefore, the values are different. Dipolar and octupolar contributions for β_{HRS} were determined following **Equations 33-38**, the results are summarized in **Table 3.10**. The dipolar/octupolar contributions are rationalised by using the nonlinear anisotropy parameter (**ρ**) in **Table 3.10**. Molecules with **ρ** values less than 1 have a more pronounced dipolar character and those with **ρ** values greater than 1 have a more pronounced octupolar character. Less than 1 **ρ** values were found for all thio substituted Pcs, suggesting that they have a more pronounced octupolar character. β-H_2Pc(tert-BPh)$_8$ showed a **ρ** value greater than 1, suggesting that it has a greater dipolar contribution to the β_{HRS} value. This trend has been seen in literature[30], where the substitution with 4-tert butyl phenoxy groups resulted in molecules with a more pronounced octupolar characteristic. The polar plots, **Figures 27** and **28**, are consistent with the determined dipolar/octupolar contribution. Depolarization ratio (**DR**) gives information about the geometry of the molecule. The smallest DR value was found for β-H_2Pc(tert-BPh)$_8$, suggesting this compound was more symmetrical compared to β-$H_2Pc(SC_5H_{11})_8$ and α-$H_2Pc(SC_5H_{11})_8$ compounds.

Table 3.10: Table displaying theoretical data of phthalocyanines including first order hyperpolarizability (β_{HRS}), dipolar and octupolar parameters with the Nonlinear anisotropy parameter and the depolarization ratio (where the dynamic is presented in the bracket parenthesis)

Pc	**β_{HRS} (esu) x 10^{-28}**	**$\phi_{(J=1)}$**	**$\phi_{(J=3)}$**	**ρ**	**DR**
α-$H_2Pc(SC_5H_{11})_8$	4.99	0.9064	0.0935	0.1032	7.872
β-$H_2Pc(SC_5H_{11})_8$	5.59	0.8631	0.1368	0.1585	7.397
β-H_2Pc(tert-BPh)$_8$	1.85	0.1047	0.8952	8.548	1.979
C_{2v}	4.89	0.9510	0.0489	0.0515	8.391
C_S	7.87	0.9509	0.0490	0.0515	8.391
D_{2h}	7.41	0.9454	0.0545	0.0577	8.324
C_{4h}	5.83	0.9141	0.0858	0.0939	7.959

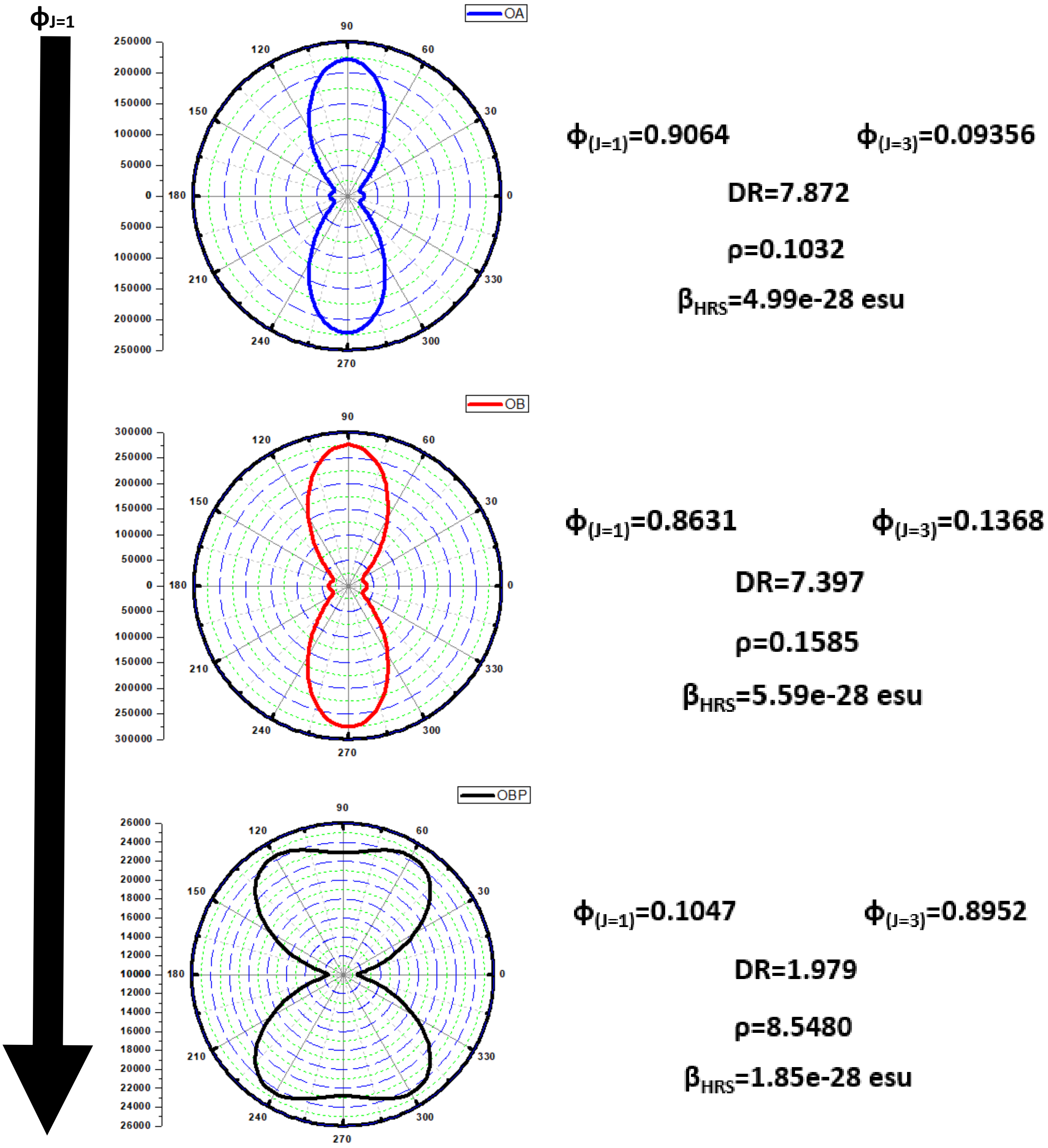

Figure 3.27: Polar plots of α-$H_2Pc(SC_5H_{11})_8$, β-$H_2Pc(SC_5H_{11})_8$ and β-$H_2Pc(tert\text{-}BPh)_8$

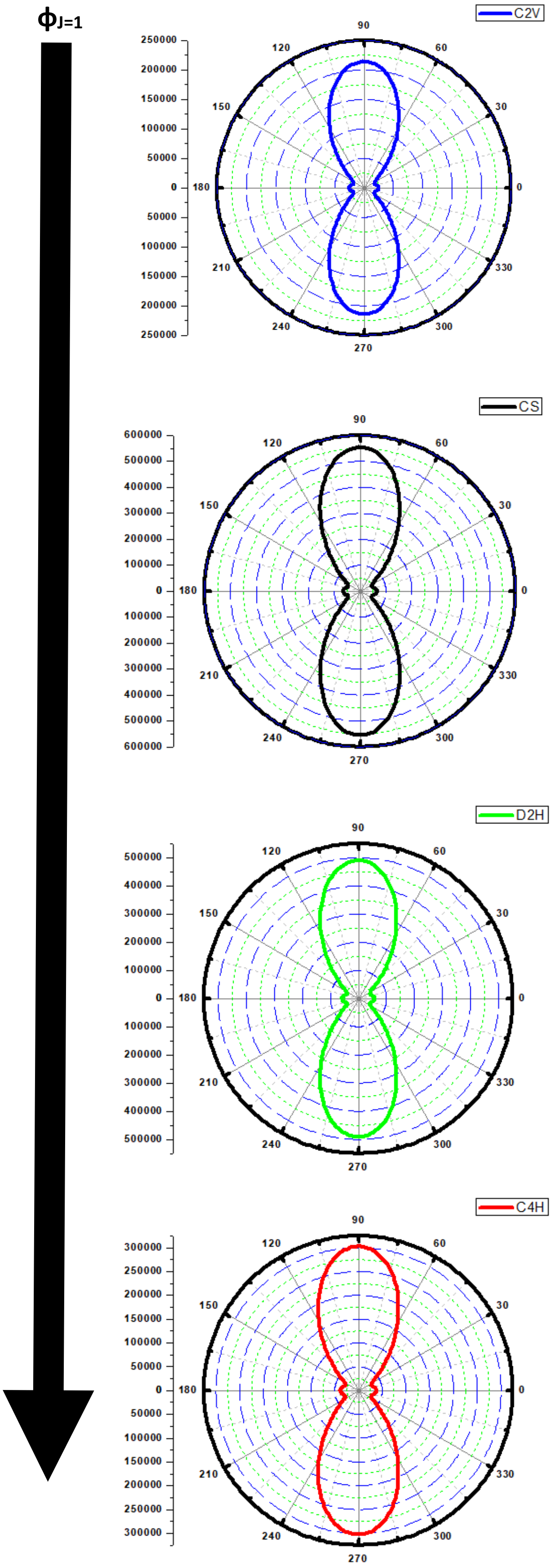

$\phi_{(J=1)}=0.9510$ $\phi_{(J=3)}=0.0489$

DR=8.391

$\rho=0.0515$

$\beta_{HRS}=4.89e\text{-}28$ esu

$\phi_{(J=1)}=0.9509$ $\phi_{(J=3)}=0.0490$

DR=8.391

$\rho=0.0515$

$\beta_{HRS}=7.877e\text{-}28$ esu

$\phi_{(J=1)}=0.9454$ $\phi_{(J=3)}=0.0545$

DR=8.324

$\rho=0.0577$

$\beta_{HRS}=7.41e\text{-}28$ esu

$\phi_{(J=1)}=0.9141$ $\phi_{(J=3)}=0.0858$

DR=7.959

$\rho=0.0939$

$\beta_{HRS}=5.83e\text{-}28$ esu

Figure 3.28: Polar plots of C_{2v}, C_s, D_{2h}, C_{4h} Phthalocyanines.

Chapter 4 Conclusions

4. Conclusions

The intended phthalonitriles and phthalocyanines were synthesized and purified. The isolation of these compounds was confirmed by infrared spectroscopy and mass spectroscopy. The octa-substituted variants of the Pcs were easier to isolate than other Pcs due to the solvent system required to provide resolution between products and side products. The effect of substitution was observed in all the photophysical data. Symmetry and the type of substituent had a large effect on these photophysical parameters.

The DFT, TDDFT and RT-TDDFT computational data gave insight into the trends observed in the experimental results relating to ground state absorption, excited state absorption and geometry of the phthalocyanines. RT-TDDFT was also able to give information to exicted state aborptions that take place in phthalocyanines, in particular absorptions around the 532nm range. The accuracy of the energies attained through the computational data could be improved by adding in solvent effects, use of more accurate basis sets and functionals and finding ways around the steric effects that cause obstructions during the geometrical optimisation process that result in the use of truncations to the molecule size.

The UV/Vis and TCSPC gave absorbance, fluorescence emission and excitation spectra, fluorescence lifetime, anisotropy rotational correlation time values and molecular volumes (V_m) for some of the phthalocyanines. Symmetry and substitution had an effect on these parameters. The TCSPC was able to give very accurate analysis relating to purity and fluoresence. The MCD spectra of the Pcs displayed that the Pcs were non metalated.

There were different magnitudes of aggregation observed through the photophysical data. The aggregation negatively affected the observed molar attenuation coeffient at the Q-band in the Pcs. This issue can be remedied through the metalation of the Pcs with a metal complex with axial ligands such as $SnCl_2$. This metalation will also increase the ISC possible in the molecule through the heavy atom effect and thus will allow for more accurate five energy level populations and cross section values. DFT calculated theorectical Im[γ] values.

The parametric and nonparametric models were able to fit the Z-Scan data and generate useful NLO parameters. The effect of substitution was seen in both the tetra and the octa substituted phthalocyanines. The pentane thiol substituent was seen as an acceptable subtituent to enhance NLO behaviour. When substituted in the same position and to the same extent, the tert-butyl phenoxy groups resulted in a better NLO limiting material as reflected in the β and Im[λ] values.

4.1 Future Work

The synthesis and purification of the 4 constitutional isomers associated with β-$H_2Pc(SC_5H_{11})_4$, and the spectroscopy studies associated with the isomers will provide further clarification as to whether the effects observed due to the change in symmetry hold true when the substituents of the Pc isomer are placed in the beta position compared to the alpha position. To gain a further understanding on the effects of sulphur of the triplet state dynamics of the molecule, it would be imperative to metalate the phthalocyanines with a heavy metal complex with axial ligands to increase the ISC that occurs and to remove the effects of aggregation with the spectroscopy of the materials.

Chapter 5 References

1. Roychoudhuri, C., & Pedrotti, L. (2009). Basic Geometrical Optics. In C. Roychoudhuri (Ed.), *Fundamentals of Photonics* (pp. 73–116). SPIE Society of Photo-Optical Instrumentation. https://doi.org/10.1117/3.784938.ch3
2. Maxwell, J. C. (1865). A Dynamical Theory of the Electromagnetic Field. *Philos. Trans. R. Soc. London*, *155*, 495–512.
3. Yao, C.-B., Zhang, Y.-D., Li, J., Chen, D.-T., Yin, H.-T., Yu, C.-Q., & Yuan, P. (2014). Study of the nonlinear optical properties and behavior in phenoxy-phthalocyanines liquid at nanosecond laser pulses. *Optical Materials*, *37*(March 2016), 80–86. https://doi.org/10.1016/j.optmat.2014.05.003
4. Britton, J., Martynov, A. G., Oluwole, D. O., Gorbunova, Y. G., Tsivadze, A. Y., & Nyokong, T. (2016). Improvement of nonlinear optical properties of phthalocyanine bearing diethyleneglycole chains: Influence of symmetry lowering vs. heavy atom effect. *Journal of Porphyrins and Phthalocyanines*. https://doi.org/10.1142/S1088424616501042
5. Louzada, M. (2020). *Determination of the Nonlinear Optical properties of Phthalocyanine Stereoisomers Using Computational Methods - (PhD Thesis)*. Rhodes University.
6. Ying Xie, Fei Liang, Bo Zhang, Binghui Ge, Haohai Yu, Zheshuai Lin, Z., & Wang, Huaijin Zhang, Baibiao Huang, J. W. (2019). Artificial Second- Order Nonlinear Optics in a Centrosymmetric Optical Material BiVO4 : Breaking the Prerequisite for Nonlinear Optical Materials. *ACS Omega*, *4*, 1045–1052.
7. Hecht, J. (2010). Short history of laser development. *SPIE Reviews*, *1*(1). https://doi.org/10.1364/ao.49.000f99
8. Jiménez, C. C., Enríquez-Cabrera, A., González-Antonio, O., Ordóñez-Hernández, J., Lacroix, P. G., Labra-Vázquez, P., & Santillan, R. (2018). State of the art of boron and tin complexes in second- and third-order nonlinear optics. *Inorganics*, *6*(4). https://doi.org/10.3390/inorganics6040131
9. New, G. H. C. (2011). Nonlinear optics : the first 50 years. *Contemporary Physics*, *7514*. https://doi.org/10.1080/00107514.2011.588485
10. Boyd, R. (2008). *Nonlinear Optics*. (Elsevier, Ed.) (3rd ed.). Elsevier.
11. Paschotta, R. (2020). Nonlinear Polarization. *RP- Photonics*. Retrieved from https://www.rp-photonics.com/nonlinear_polarization.html
12. Physics, I. of. (2020). Basic Nonlinear Optics. *University of Pécs*. Retrieved from http://www.physics.ttk.pte.hu/files/TAMOP/FJ_Nonlinear_Optics/index.html

13. Boyd, R. W. (2003). The Nonlinear Optical Susceptibility. *Nonlinear Optics*, (1941), 1–65. https://doi.org/10.1016/b978-012121682-5/50002-x

14. Mayerhöfer, T. G., Pipa, A. V., & Popp, J. (2019). Beer's Law-Why Integrated Absorbance Depends Linearly on Concentration. *ChemPhysChem*, *20*(21), 2748–2753. https://doi.org/10.1002/cphc.201900787

15. Straub, Q. M. (2010). *A Methodology for the Determination of the Light Distribution Profile of a Micro-Algal Photobiopreactor*. Florida State University.

16. Nanda, K. D., & Krylov, A. I. (2017). Visualizing the Contributions of Virtual States to Two-Photon Absorption Cross Sections by Natural Transition Orbitals of Response Transition Density Matrices. *Journal of Physical Chemistry Letters*, *8*(14), 3256–3265. https://doi.org/10.1021/acs.jpclett.7b01422

17. Band, Y. B. (1986). Optical Properties and Applications of Reverse Saturable Absorbers. In *Methods of Laser Spectroscopy* (pp. 117–118). Boston, MA: Springer. https://doi.org/https://doi.org/10.1007/978-1-4615-9459-8_16

18. Tsigaridas, G., Polyzos, I., Persephonis, P., & Giannetas, V. (2006). A novel approach for analyzing open Z-scan experiments. *Optics Communications*, *266*(1), 284–289. https://doi.org/10.1016/j.optcom.2006.04.015

19. Perry, J. W., Alvarez, D., Choong, I., Mansour, K., Marder, S. R., & Perry, K. J. (1994). Enhanced reverse saturable absorption and optical limiting in heavy-atom-substituted phthalocyanines. *Optics Letters*, *19*(9), 625. https://doi.org/10.1364/ol.19.000625

20. de laTorre, G., Vazquez, P., Agullo-Lopez, F., & Torres, T. (2004). Role of Structural Factors in the Nonlinear Optical Properties of Phthalocyanines and Related Compounds. *Chemical Reviews*, *104*(9), 3723–3750. https://doi.org/10.1021/cr030206t

21. Lind, P. (2007). *Organic and Organometallic Compounds for Nonlinear Absorption of Light - (PhD Thesis)*. Umeå university.

22. Claessens, C. G., Blau, W. J., Cook, M., Hanack, M., Nolte, R. J. M., Torres, T., & Wöhrle, D. (2001). Phthalocyanines and phthalocyanine analogues: The quest for applicable optical properties. *Monatshefte fur Chemie*, *132*(1), 3–11. https://doi.org/10.1007/s007060170140

23. Braun, A., & Tcherniac, J. (1907). Article. *Ber. Dtsch. Chem. Ges*, *40*, 2709.

24. de Diesbach, H., & von der Weid, E. (1927). Quelques sels complexes des o-dinitriles avec le cuivre et la pyridine. *Helv. Chim. Acta*, *10*, 886.

25. Linstead, R. (1933). Article. *Br. Asso. Adv. Sci. Rep*, 465.

26. Dandridge, A. G., Drescher, H. A. E., & Thomas, J. (1929). Patent. Great Britain.

27. Robertson, J. M. (1935). An X-ray study of the structure of the phthalocyanines. Part I. The

metal-free, nickel, copper, and platinum compounds. *J. Chem. Soc*, (0), 615.

28. Ghani, F., Kristen, J., & Riegler, H. (2012). Solubility properties of unsubstituted metal phthalocyanines in different types of solvents. *Journal of Chemical and Engineering Data*, *57*(2), 439–449. https://doi.org/10.1021/je2010215
29. Neduvhuledza, M. Z. R. (2020). *Synthesis , characterisation , and Nonlinear Optical Properties of the positional isomers of Cobalt , Nickel and Copper 4-(tertbutylphenoxy) Phthalocyanine - (MSc Thesis)*. Rhodes University.
30. Ngubeni, G. N. (2016). *Spectroscopic and nonlinear optical characterisation of alpha substituted binuclear phthalocyanines - (MSc Thesis)*. Rhodes University.
31. Xue, J., Uchida, S., Rand, B. P., & Forrest, S. (2015). High efficiency organic photovoltaic cells employing hybridized mixed-planar heterojunctions. United States.
32. Nyokong, T. (2011). Desired properties of new phthalocyanines for photodynamic therapy. *Pure Appl. Chem*, *Vol. 83*(9), 1763–1779.
33. Calvete, M. J. F., Dini, D., Hanack, M., Sancho-García, J. C., Chen, W., & Ji, W. (2006). Synthesis, DFT calculations, linear and nonlinear optical properties of binuclear phthalocyanine gallium chloride. *Journal of Molecular Modeling*, *12*(5), 543–550. https://doi.org/10.1007/s00894-005-0043-5
34. Song, L. C., Luo, F. X., Liu, B. B., Gu, Z. C., & Tan, H. (2016). Novel Ruthenium Phthalocyanine-Containing Model Complex for the Active Site of [FeFe]-Hydrogenases: Synthesis, Structural Characterization, and Catalytic H2 Evolution. *Organometallics*, *35*(10), 1399–1408. https://doi.org/10.1021/acs.organomet.5b01040
35. Boscencu, R., Ilie, M., & Socoteanu, R. (2011). Spectroscopic behavior of some A(3)B type tetrapyrrolic complexes in several organic solvents and micellar media. *International Journal of Molecular Sciences*, *12*(9), 5552–5564. https://doi.org/10.3390/ijms12095552
36. Tau, P., & Nyokong, T. (2007). Electrochemical characterisation of tetra- and octa-substituted oxo(phthalocyaninato)titanium(IV) complexes. *Electrochimica Acta*, *52*(11), 3641–3650. https://doi.org/10.1016/j.electacta.2006.10.023
37. Banerjee, S., & Mazumdar, S. (2012). Electrospray Ionization Mass Spectrometry: A Technique to Access the Information beyond the Molecular Weight of the Analyte. *International Journal of Analytical Chemistry*, *2012*, 1–40. https://doi.org/10.1155/2012/282574
38. Gouterman, M. (1961). Spectra of Porphyrins. *Journal of Molecular Spectroscopy*, *6*.
39. Dodsworth, E. S., Lever, A. B. P., Seymour, P., & Leznoff, C. . (1985). Intramolecular coupling in metal-free binuclear phthalocyanines. *J. Phys. Chem.*, *89*, 5698.
40. Mwanza, D., Louzada, M., Britton, J., Sekhosana, E., Khene, S., Nyokong, T., & Mashazi, P.

(2018). The effect of the cobalt and manganese central metal ions on the nonlinear optical properties of tetra(4-propargyloxyphenoxy)phthalocyanines. *New Journal of Chemistry*, *42*(12), 9857–9864. https://doi.org/10.1039/c8nj00748a

41. Mack, J., Stillman, M. J., & Kobayashi, N. (2007). Application of MCD spectroscopy to porphyrinoids. *Coordination Chemistry Reviews*, *251*(3–4), 429–453. https://doi.org/10.1016/j.ccr.2006.05.011
42. Mack, J., & Stillman, M. J. (2001). Assignment of the optical spectra of metal phthalocyanines through spectral band deconvolution analysis and ZINDO calculations. *Coordination Chemistry Reviews*, *219–221*, 993–1032. https://doi.org/10.1016/S0010-8545(01)00394-0
43. Mack, J., & Kobayashi, N. (2011). Low symmetry phthalocyanines and their analogues. *Chemical Reviews*, *111*(2), 281–321. https://doi.org/10.1021/cr9003049
44. Mack, J., Liang, X., Dubinina, T. V., Tomilova, L. G., Nyokong, T., & Kobayashi, N. (2013). MCD spectroscopy and TD-DFT calculations of a naphthalene-ring-bridged coplanar binuclear phthalocyanine dimer. *Journal of Porphyrins and Phthalocyanines*, *17*(6–7), 489–500. https://doi.org/10.1142/S1088424613500259
45. Snow, A. W. (2003). Phthalocyanine Aggregation. *The Porphyrin Handbook*, *17*, 129–173.
46. Satake, A., & Kobuke, Y. (2007). Artificial photosynthetic systems: assemblies of slipped cofacial porphyrins and phthalocyanines showing strong electronic coupling. *Org. Biomol. Chem.*, *5*, 1679.
47. George, R. D., Snow, A. W., Shirk, J. S., & Barger, W. R. (1998). The alpha substitution effect on phthalocyanine aggregation. *Journal of Porphyrins and Phthalocyanines*, *2*, 1.
48. Wang, Z. S., Hara, K., Dan-Oh, Y., Kasada, C., Shinpo, A., Suga, S., & Sugihara, H. (2005). Photophysical and (Photo)electrochemical Properties of a Coumarin Dye. *J. Phys. Chem. B.*, *109*, 3907.
49. Kobayashi, T., Du, J., & Kida, Y. (1996). Ultrafast Real-Time Vibrational Dynamics in J-Aggregates (1st ed.). World Scientific.
50. Chakraborty, S., Debnath, P., Dey, D., Bhattacharjee, D., & Hussain, S. A. (2014). Formation of fluorescent H-aggregates of a cyanine dye in ultrathin film and its effect on energy transfer. *J. Photochem. Photobiol. A*, *293*, 57.
51. Ngubeni, G. N., New, E., Hancox, I., Walker, M., Nyokong, T., Jones, T. S., & Khene, S. (2015). Spectroscopic and nonlinear optical properties of the four positional isomers of 4α-(4-tert-butylphenoxy)phthalocyanine. *J. Mater. Chem. C*, *3*, 10705–10714. https://doi.org/10.1039/C5TC01601K
52. Stradi, D., Díaz, C., Martín, F., & Alcamí, M. (2011). A density functional theory study of the

manganese-phthalocyanine. *Theoretical Chemistry Accounts*. https://doi.org/10.1007/s00214-010-0852-1

53. Modibane, D. K., & Nyokong, T. (2008). Synthesis and photophysical properties of lead phthalocyanines. *Polyhedron*, *27*(3), 1102–1110. https://doi.org/10.1016/j.poly.2007.12.004

54. So, P. T. C., & Dong, C. Y. (2002). Fluorescence Spectrophotometry. In *Encyclopedia of Life Sciences*.

55. Shimizu, Y., & Azumi, T. (1982). Mechanism of External Heavy Atom Effect on Intersystem Crossing in Fluid Solutions . *J. Phys. Chem.*, *86*, 22–26. https://doi.org/10.1021/j100390a006

56. Van Der Werf, R., Zevenhuijzen, D., & Kommandeur, J. (1974). Reversible intersystem crossing, fluorescence lifetime lengthening and collisionally induced phosphorescence in biacetyl. *Chemical Physics Letters*, *27*(3).

57. Lakowicz, J. R. (2006). *Principles of Fluorescence Spectroscopy* (3rd ed.).

58. Tombe, S., Antunes, E., & Nyokong, T. (2013). The photophysical and photochemical behaviour of coumarin-derivatized zinc phthalocyanine when conjugated with gold nanoparticles and electrospun into polymer fibers. *New J. Chem.*, *37*, 679–689. https://doi.org/10.1039/c2nj40984d

59. Cueto, C., Perez, A., & Racedo, F. (2017). Characterization of the nonlinear optical properties of the new 2-amino-4,6-difenilnicotinonitrilo by UV-Vis spectroscopy absorption and Z-Scan. *Journal of Physics: Conference Series*, *786*. https://doi.org/10.1088/1742-6596/786/1/012005

60. Stryland, E. W. Van, & Sheik-Bahae, M. (1998). Z-Scan Measurements of Optical Nonlinearities. *Characterization Techniques and Tabulations for Organic Nonlinear Materials*, (3), 655–692.

61. Mageza, R. (2020). *Synthesis, Spectroscopic and Nonlinear Optical Properties of Asymmetric A3B Type Phthalocyanine Complexes - (MSc Thesis)*. Rhodes University.

62. Nkaki, T. (2020). *Nonlinear Optical Studies of Copper , Cobalt and Nickel Phthalocyanine Complexes Non-Peripherally Substituted With (4-(Methylthio)Phenylthio) Group - (MSc Thesis)*. Rhodes University.

63. Castet, F., Bogdan, E., Plaquet, A., Ducasse, L., Champagne, B., & Rodriguez, V. (2012). Reference molecules for nonlinear optics: A joint experimental and theoretical investigation. *Journal of Chemical Physics*, *136*(2). https://doi.org/10.1063/1.3675848

64. Pretsch, E., Buhlmann, P., & Badertscher, M. (2009). *Structure Determination of Organic Compounds* (4th ed.). Heidelberg: Springer-Verlag. https://doi.org/10.1007/978-3-540-93810-1

65. Ishida, H., & Beeby, A. (2016). Guidelines for measurement of luminescence spectra and

quantum yields of inorganic and organometallic compounds in solution and solid state (IUPAC Technical Report), *88*(7), 701–711. https://doi.org/10.1515/pac-2014-0706

66. Makinde, Z. O., Louzada, M. S., Britton, J., Nyokong, T., & Khene, S. (2019). Dyes and Pigments Spectroscopic and nonlinear optical properties of alkyl thio substituted binuclear phthalocyanines. *Dyes and Pigments*, *162*(June 2018), 249–256. https://doi.org/10.1016/j.dyepig.2018.10.022

67. Waluk, J., & Michl, J. (1991). The Perimeter Model and Magnetic Circular Dichroism of Porphyrin Analogues. *Journal of Organic Chemistry*, *56*(8), 2729–2735. https://doi.org/10.1021/jo00008a029

68. Quartarolo, A. D., Lanzo, I., Sicilia, E., & Russo, N. (2009). Can phthalocyanines and their substituted a-para-(methoxy)phenyl derivatives act as photosensitizers in photodynamic therapy? A TD-DFT study. *Physical Chemistry Chemical Physics*, *11*(22), 4586–4592. https://doi.org/10.1039/b819064j

69. Kabwe, K. P., Louzada, M., Britton, J., Olomola, T. O., Nyokong, T., & Khene, S. (2019). Nonlinear optical properties of metal free and nickel binuclear phthalocyanines. *Dyes and Pigments*, *168*(April), 347–356. https://doi.org/10.1016/j.dyepig.2019.05.003

70. Chen, Y., Hanack, M., Araki, Y., & Ito, O. (2005). Axially modified gallium phthalocyanines and naphthalocyanines for optical limiting. *Chemical Society Reviews*, *34*(6), 517–529. https://doi.org/10.1039/b416368k

71. Dini, D., & Hanack, M. (2003). *In The Porphyrin Handbook: Physical Properties of Phthalocyanine based Materials*. (K. M. Kadish, K. M. Smith, & R. Guilard, Eds.).

72. Louzada, M., Britton, J., Nyokong, T., & Khene, S. (2017). Solvent Effect on the Third-Order Nonlinear Optical Properties of α- and β-Tertbutyl Phenoxy-Substituted Tin(IV) Chloride Phthalocyanines. *Journal of Physical Chemistry A*, *121*(38), 7165–7175. https://doi.org/10.1021/acs.jpca.7b07349

73. Rao, S. V., Rao, D. N., Akkara, J. A., Decristofano, B. S., & Rao, D. V. G. L. N. (1998). Dispersion studies of non-linear absorption in C60 using Z-scan. *Chemical Physics Letters*, *297*(5–6), 491–498. https://doi.org/10.1016/S0009-2614(98)01166-X

Chapter 6 Appendix

Qo

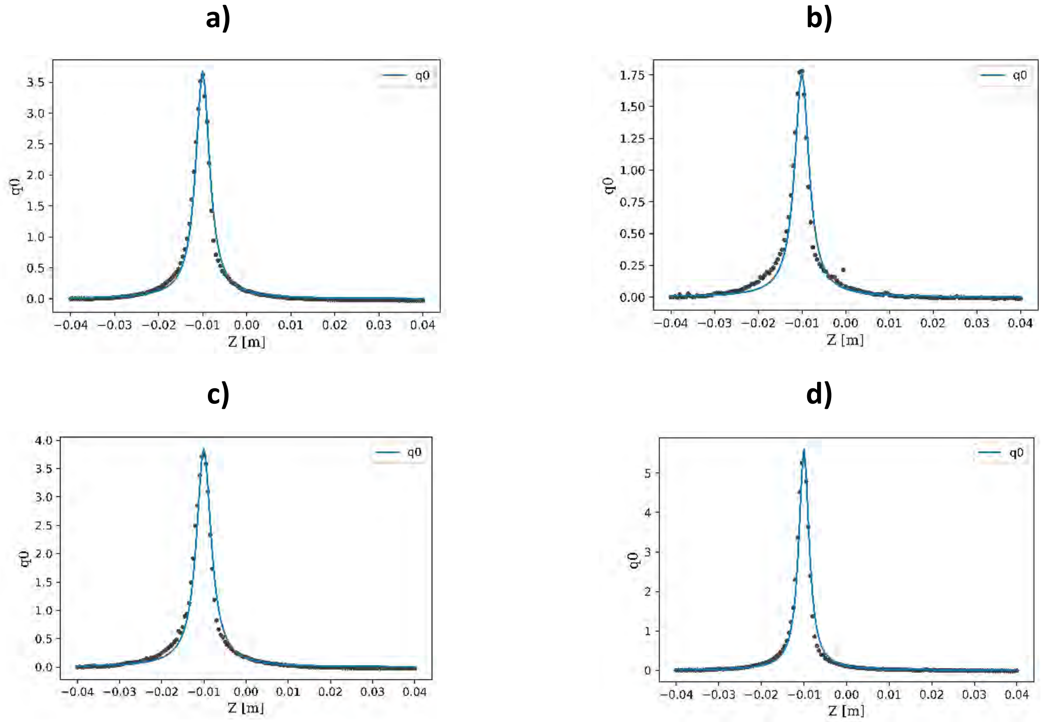
a) b) c) d)

Figure 6.1: Open aperture nonlinear fit z-scan curve for α-$H_2Pc(SC_5H_{11})_4$ C_s isomer (a) at a focal intensity of 2.96 x 10^{12} W.m^{-2}, C_{4h} isomer (b) at a focal intensity of 3.06 x 10^{12} W.m^{-2}, D_{2h} isomer (c) at a focal intensity of 3.26 x 10^{12} W.m^{-2} and C_{2v} isomer (d) at a focal intensity of 5.28 x 10^{12} W.m^{-2} in chloroform.

Table 6.1: RT-TDDFT ground and excited state results

C_s	
Ground	**Excited**
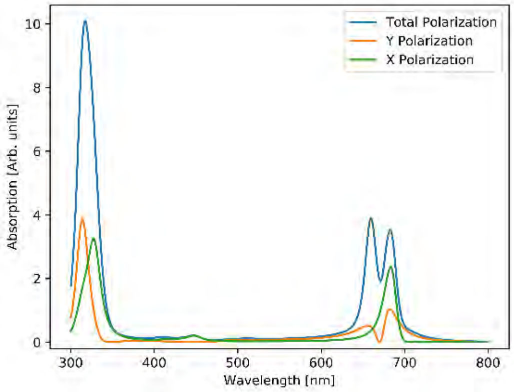	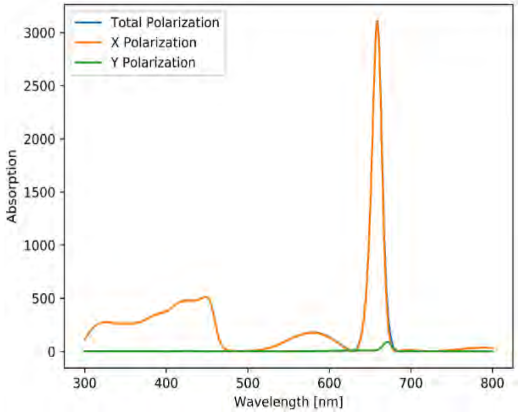

C_{4h}

Ground

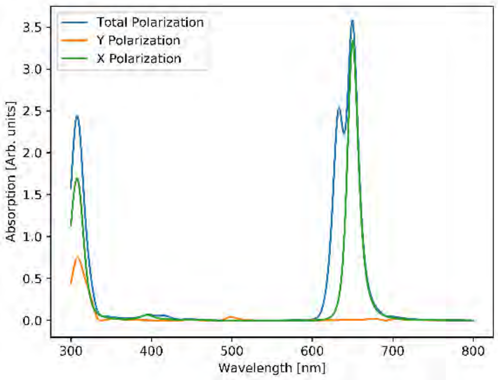

Excited

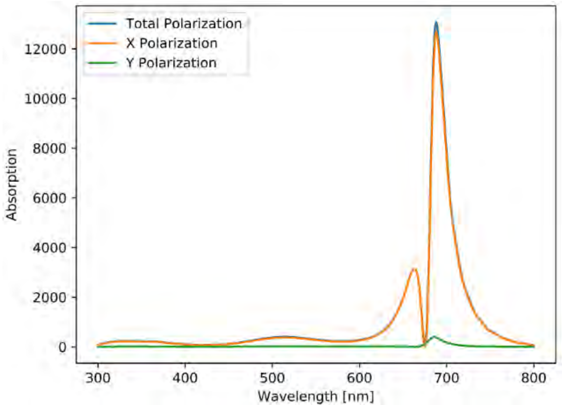

D_{2h}

Ground

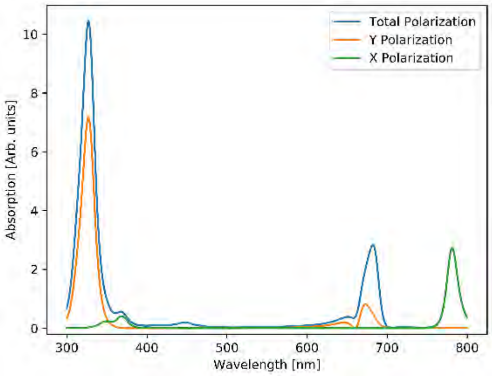

Excited

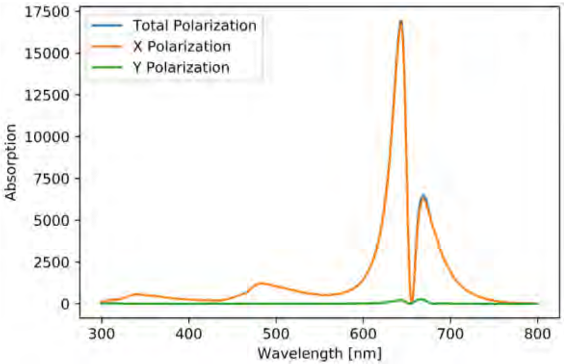

C_{2v}

Ground

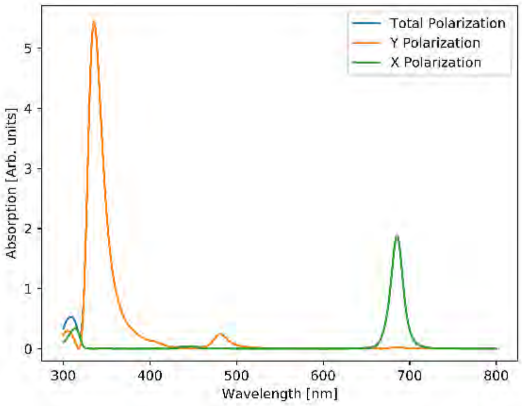

Excited

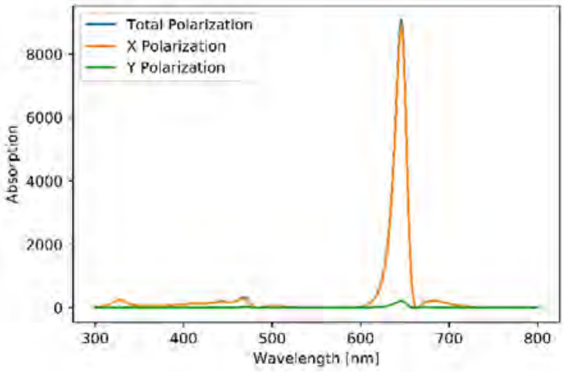

<table>
<tr><th colspan="2">α-$H_2Pc(SC_5H_{11})_8$</th></tr>
<tr><th>Ground</th><th>Excited</th></tr>
<tr><td>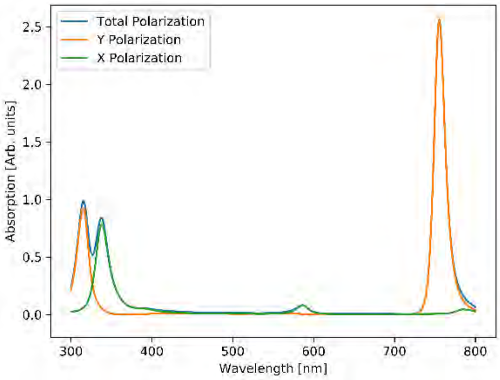
</td><td>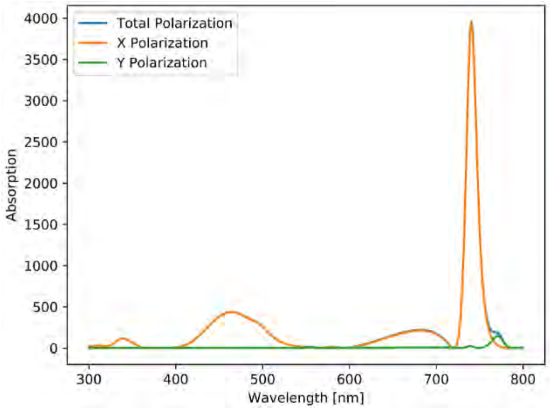
</td></tr>
<tr><th colspan="2">β-$H_2Pc(SC_5H_{11})_8$</th></tr>
<tr><th>Ground</th><th>Excited</th></tr>
<tr><td>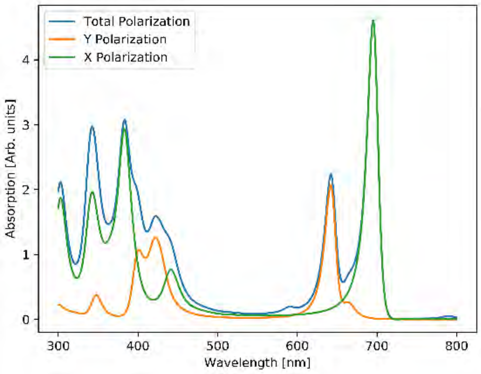
</td><td>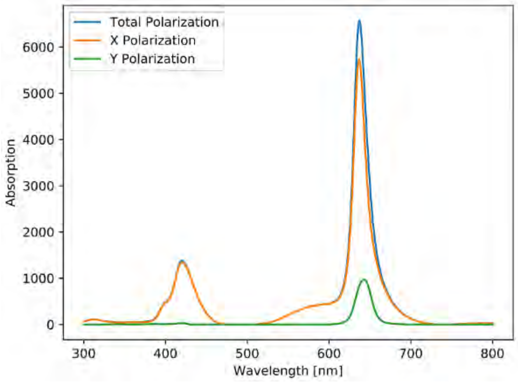
</td></tr>
</table>

Table 6.2: MALDI-TOF results

C_s

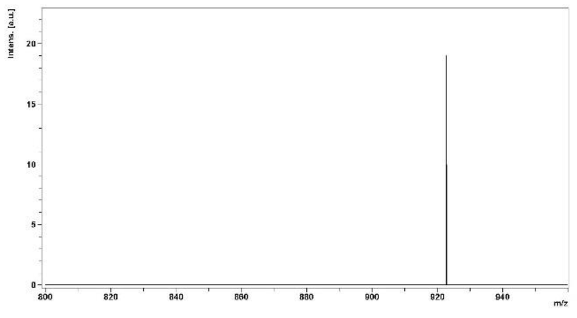

C_{4h}

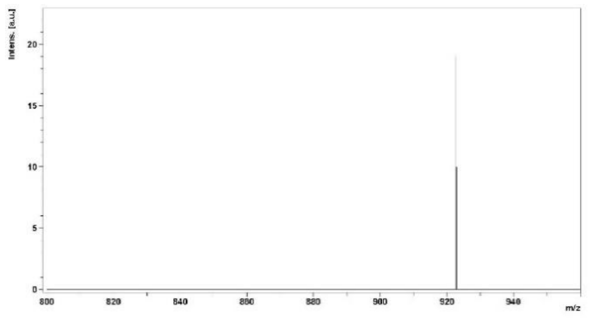

D_{2h}

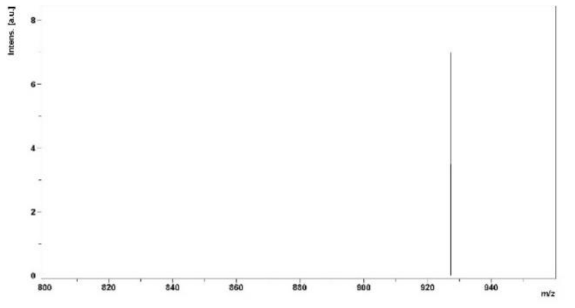

C_{2v}

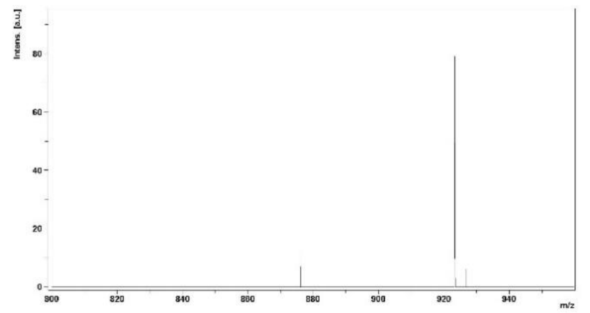

α-$H_2Pc(SC_5H_{11})_8$

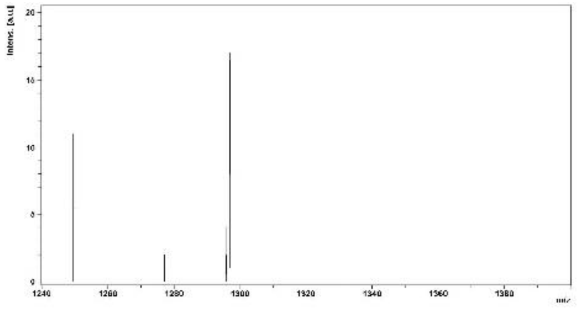

β-$H_2Pc(SC_5H_{11})_8$

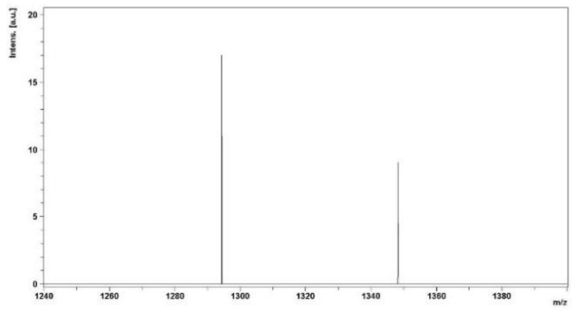

β-H_2Pc(tert-BPh)$_8$

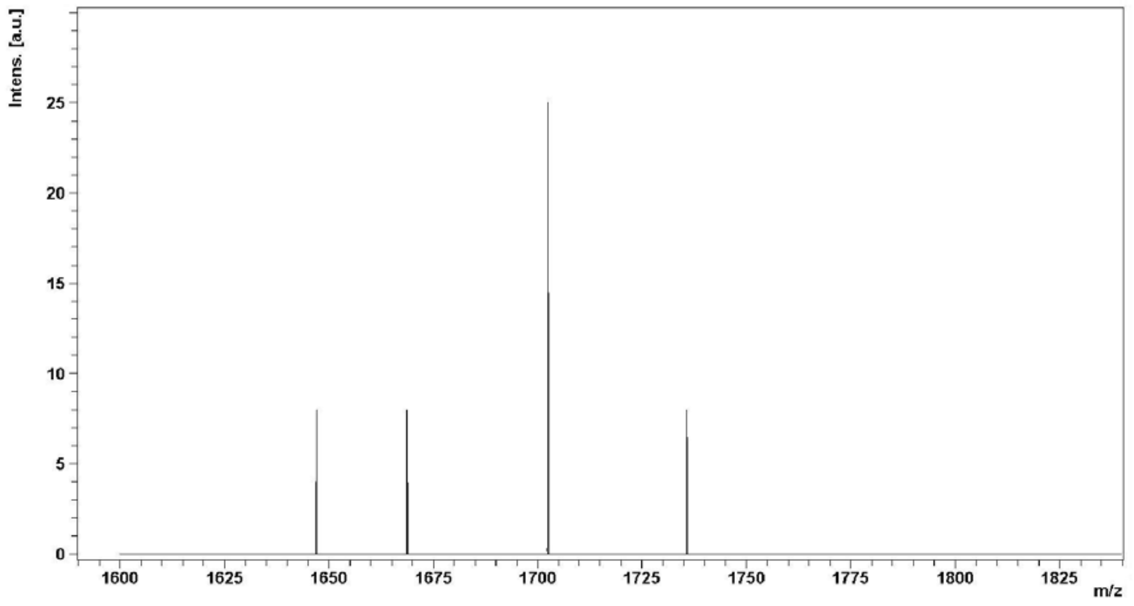

Table 6.3: Inter planar angles cross phthalocyanine carbons

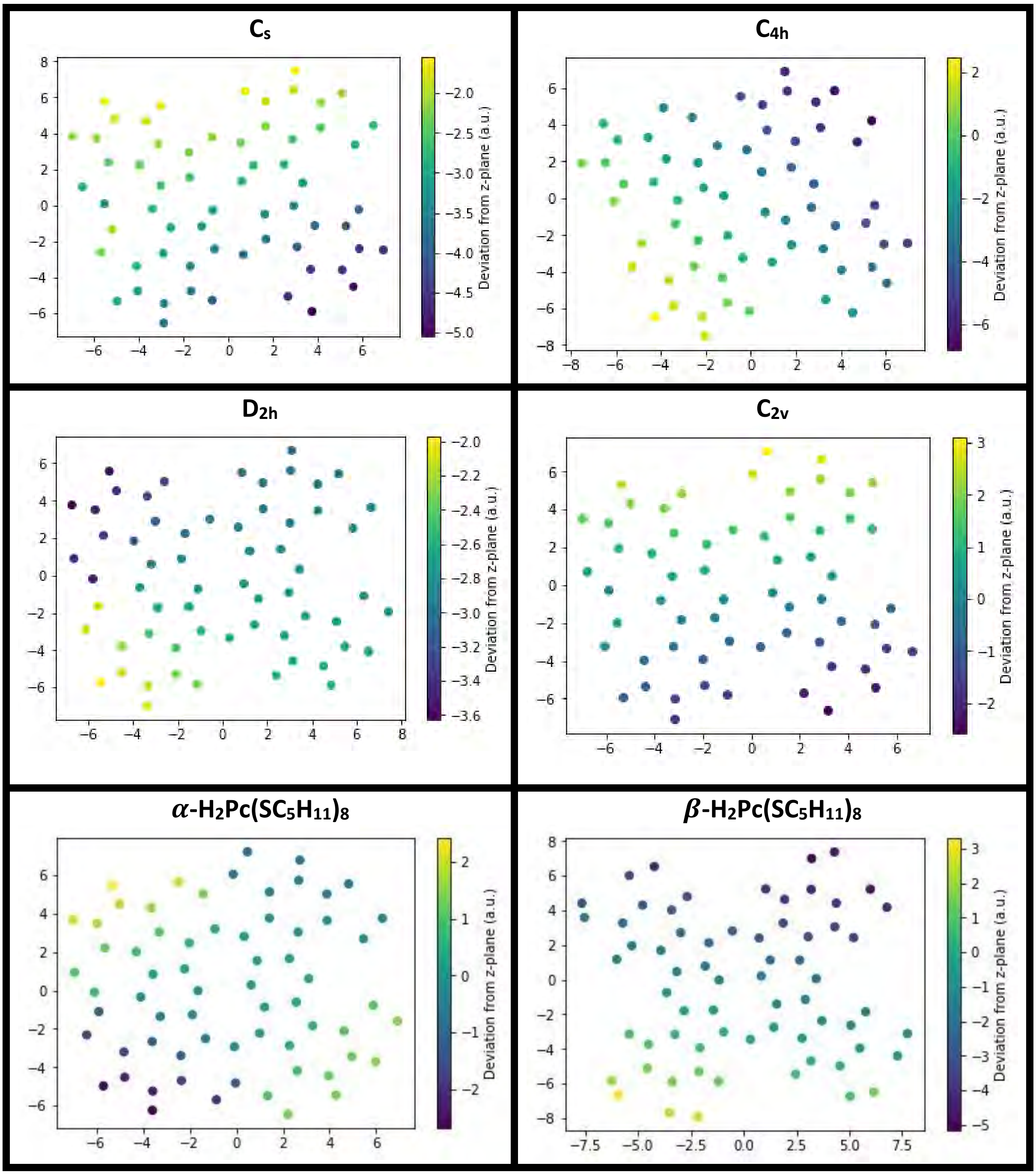

Table 6.3: Inter planar angles cross phthalocyanine carbons. (continued)

β-$H_2Pc(tert\text{-}BPh)_8$
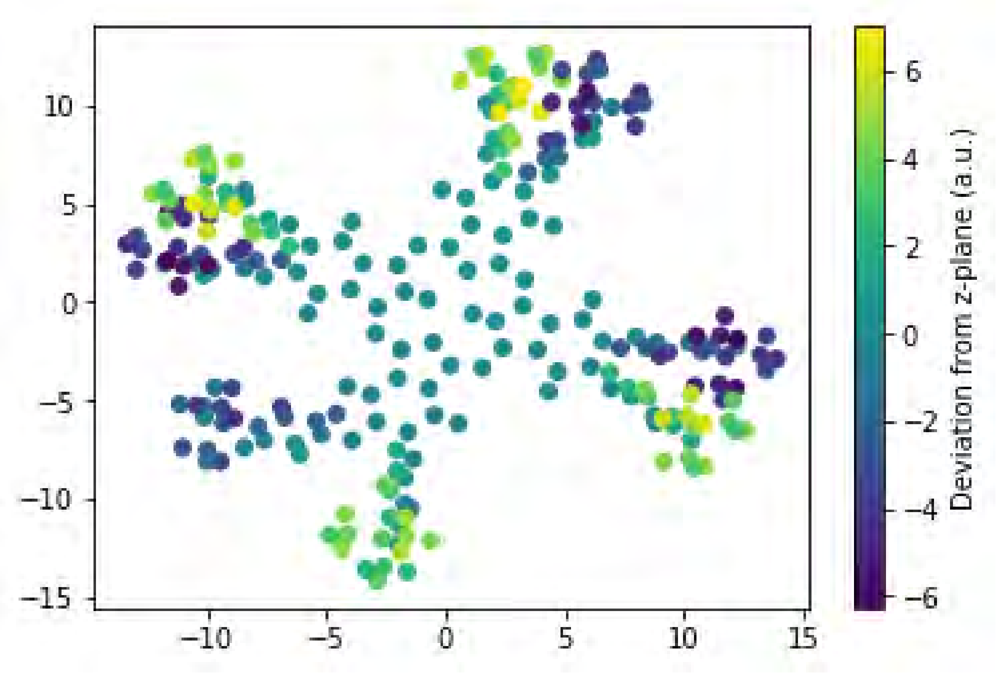

Table 6.4: Closed aperture fit graphs of phthalocyanines where focal intensity of measurement is indicated.

C_s – 2.96 x 10^{12} W.m^{-2}

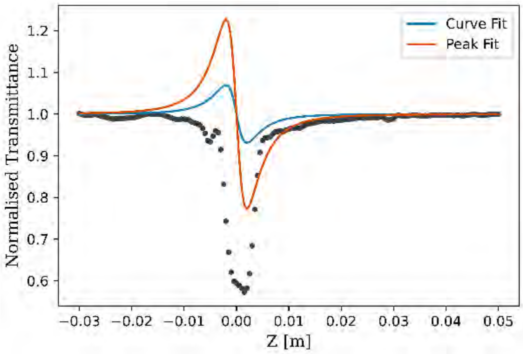

C_{4h} – 3.06 x 10^{12} W.m^{-2}

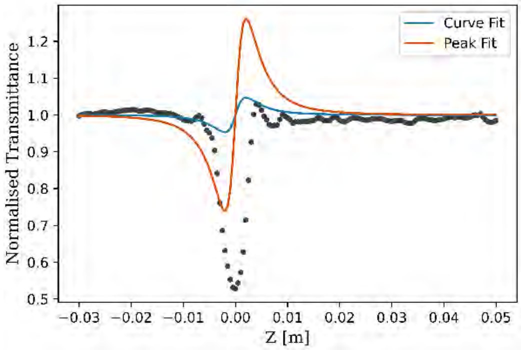

D_{2h} – 3.26 x 10^{12} W.m^{-2}

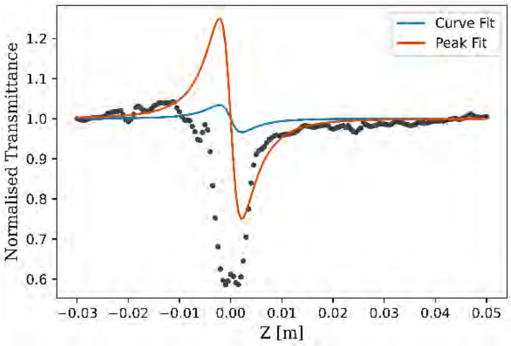

C_{2v} – 5.28 x 10^{12} W.m^{-2}

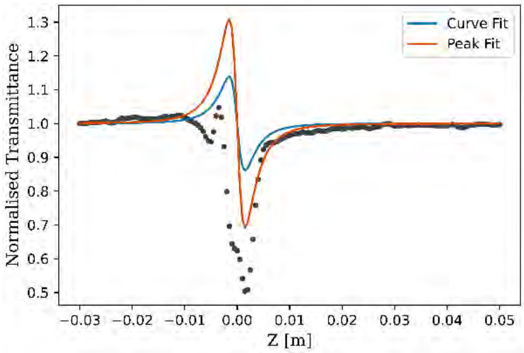

α-$H_2Pc(SC_5H_{11})_8$ – 4.06 x 10^{12} W.m^{-2}

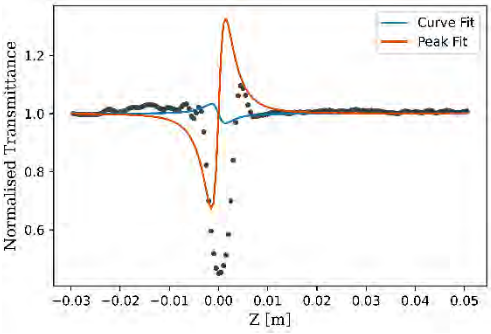

β-$H_2Pc(SC_5H_{11})_8$ – 3.52 x 10^{12} W.m^{-2}

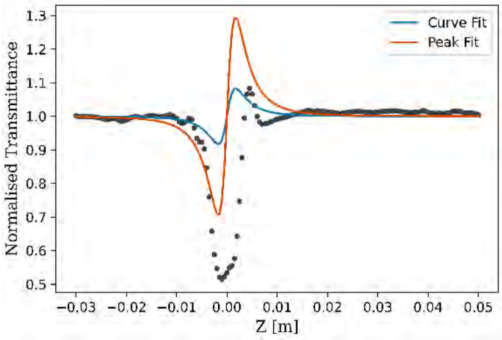

Table 6.4: Closed aperture fit graphs of phthalocyanines where focal intensity of measurement is indicated. (continued)

β-H$_2$Pc(tert-BPh)$_8$ – 2.22 x 10^{12} W.m^{-2}